Design of In Situ Metal Matrix Composites Produced by Powder Metallurgy
A Critical Review

Schramm Deschamps, Isadora ; dos Santos Avila, D.; Vanzuita Piazera, Enzo ; Dudley Cruz, Robinson Carlos ; Aguilar, Claudio; Nelmo Klein, Aloisio

DOI
10.3390/met12122073

Publication date
2022

Document Version
Final published version

Published in
Metals

Citation (APA)
Schramm Deschamps, I., dos Santos Avila, D., Vanzuita Piazera, E., Dudley Cruz, R. C., Aguilar, C., & Nelmo Klein, A. (2022). Design of In Situ Metal Matrix Composites Produced by Powder Metallurgy: A Critical Review . *Metals*, *12*(12), Article 2073. https://doi.org/10.3390/met12122073

metals

Review

Design of In Situ Metal Matrix Composites Produced by Powder Metallurgy—A Critical Review

Isadora Schramm Deschamps [1,*], Daniel dos Santos Avila [1,2], Enzo Vanzuita Piazera [1], Robinson Carlos Dudley Cruz [3,4], Claudio Aguilar [5] and Aloisio Nelmo Klein [1]

[1] Materials Laboratory (LabMat), Mechanical Engineering Department, Federal University of Santa Catarina (UFSC), Campus Universitário Reitor João David Ferreira Lima, s/n°, Trindade, Florianópolis 88040-900, Brazil
[2] Department of Materials Science and Engineering, Delft University of Technology, Mekelweg 2, 2628 CD Delft, The Netherlands
[3] Ceramic Materials Institute, Caxias do Sul University, Bom Princípio 95765-000, Brazil
[4] Hecílio Randon Institute, 95.480-000 Rua Leopoldo Andre Alves, 178—Centro, Cambara do Sul 95181-899, Brazil
[5] Department of Metallurgical Engineering and Materials, Universidad Técnica Federico Santa María, Valparaíso 2340000, Chile
* Correspondence: isadora.deschamps@labmat.ufsc.br

Abstract: In situ composite manufacture is an approach to improve interfacial adhesion between matrix and reinforcements, in which reinforcements are synthesized along composite processing itself. In situ powder metallurgy route, in particular, offers alternatives to some shortcomings found in other techniques. This work aims not only to review the state of the art on metal matrix composites (MMCs)—including cermets—obtained in situ by powder metallurgy, but also to dissect key aspects related to the development of such materials in order to establish theoretical criteria for decision making before and along experiments. Aspects regarding the design, raw material selection, and processing of such composites were observed and divided between concept, intrinsic, and extrinsic parameters. That way, by means of material databases and computational thermodynamics applied to examples of the reviewed literature, we aim at providing tools in both conducting leaner experiments and richer discussion in this field.

Keywords: metal matrix composites; cermets; powder metallurgy; computational thermodynamics; in situ

check for updates

Citation: Schramm Deschamps, I.; dos Santos Avila, D.; Vanzuita Piazera, E.; Dudley Cruz, R.C.; Aguilar, C.; Klein, A.N. Design of In Situ Metal Matrix Composites Produced by Powder Metallurgy—A Critical Review. *Metals* **2022**, *12*, 2073. https://doi.org/10.3390/met12122073

Academic Editors: Haiming Ding, Peng Wang, Xiangguang Kong and Andreas Chrysanthou

Received: 24 October 2022
Accepted: 28 November 2022
Published: 2 December 2022

1. Introduction

As for any composite, the performance of metal matrix composites (MMCs) is not only subject to the size, volume fraction, shape, and composition of reinforcements, but also to the distribution and interface between matrix and reinforcement [1]. Metal matrix composites are conventionally manufactured by a number of techniques, such as additive manufacturing [2,3], casting [4–6], and spray forming [7], but according to research studies regarding the last 10 years, the processing techniques that are the most used—around 30% of large-scale industrial level—are powder metallurgy techniques (PM) [8].

In all these techniques, the composite material is usually produced by mixing the desired reinforcement to the matrix along processing. Such an approach is named ex situ because reinforcements have already been synthesized prior to composite manufacturing. Apart from the seemingly simpler preparation by mixing, particles—especially nanometric ones—are often hard to disperse or tend to segregate from the matrix if both display significant differences in density [9]. Additionally, because it is inevitable for powder surfaces to present some level of roughness, impurities, and moisture, many ex situ composites end up suffering from porosity and contamination at the interface of reinforcements with the metal matrix [10,11], which hampers load bearing capacity, Zener pinning, and Orowan and thermal mismatch strengthening, and ultimately leads to lower overall strengthening [12].

In situ formation of reinforcements has been used as an approach to improve reinforcement adhesion with the interface. In those techniques, the reinforcements are synthesized by exothermic reactions along composite manufacturing itself. Some reinforcements have even been found to be coherent with the matrix, resulting in reduced lattice mismatch and great wettability, not to mention complete absence of contamination [13–15]. When interface bonding is adequate, it is possible to transfer load from matrix to reinforcement, and composites do not fail prematurely by intergranular fracture caused by poor interfacial strength. Such advantage implies that reinforcement particles can effectively generate and resist the movement of dislocations, as well as inhibit matrix grain growth [16]. Additionally, in situ techniques allow for raw materials saving, as they do not require the use of nanopowders to obtain nanosized reinforcements. Moreover, because reactive elements can often be found in inexpensive materials, in situ synthesis has been attained in most of the aforementioned composite processing techniques [17].

In Figure 1a,b, it is possible to see examples of such well bonded, pore-free interfaces. Figure 1b also displays the particle resisting to the passage of dislocations, which become accumulated around the reinforcement.

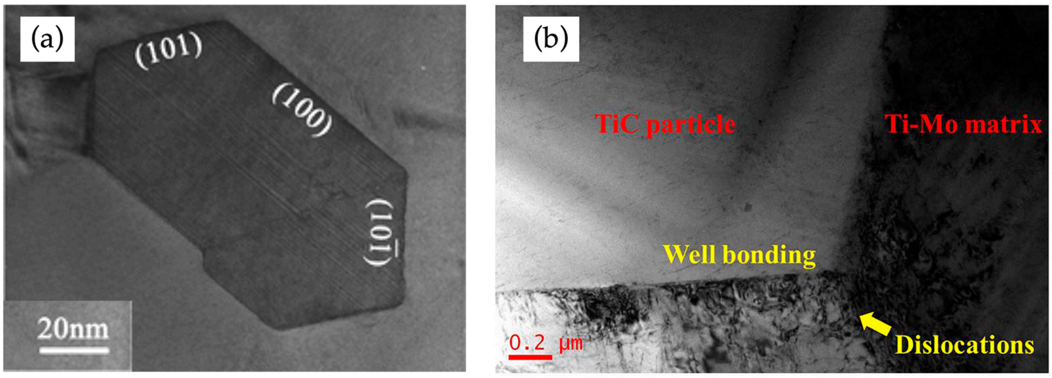

Figure 1. In situ composites produced by powder metallurgy. HDTEM images highlighting the interface between in situ (**a**) TiB and (**b**) TiC reinforcements and titanium matrices.

In situ powder metallurgy, in particular, has gained momentum in many industries because it offers interesting alternatives to shortcomings found in other techniques. Sintering uses lower temperatures and is, therefore, expected to yield more nuclei and slower coalescence of reinforcements [18]. Unlike casting, there is no incompatibility related to density differences between matrix and reinforcements, and thus there is no segregation caused by reinforcements floating inside the liquid matrix. In addition, reinforcement particles often compromise the fluidity of the molten matrix material. Powder metallurgy techniques, therefore, allow for a broader range of reinforcement compositions and volume fractions [19]. Additionally, those techniques offer all advantages inherent to powder metallurgy, such as raw material savings, low processing temperature, and near-net shape of the final product, even for complex components. This is particularly advantageous for composites, which are strong and hard to machine, and implies dramatic cost reductions, especially for large-scale production of small parts.

The tables in Appendix B of this review aim at indexing all the relevant bibliographic production we found on this topic. Details regarding the search queries, databases, and filtering criteria can be also found in Appendix A. Apart from a broad state of the art regarding what has been accomplished so far on the in situ aluminum, titanium, iron, nickel, and copper matrices composites by powder metallurgy, this paper aims at dissecting design and processing parameters—often through a thermodynamic viewpoint—that can lead to a better understanding of the relationship between processing, microstructure, and properties.

The premise of in situ composites relies on raw materials reacting to form the final composite microstructure, and this in turn requires the composite phases to have lower Gibbs free energy than the initial system. Therefore, a thermodynamic analysis of the system is necessary. Moreover, thermodynamic data, and CALPHAD-based software, such as Thermo-Calc® (All CALPHAD simulations presented in this paper were made using Thermo-Calc® with the databases TCFE7, SSOL5, and MOBFE2. Open-source software such as MatCalc could be used as well.), in particular, can be powerful tools for decision making in composite design and processing. It is possible, for instance, to analyze combinations of raw materials and estimate solid state diffusion of elements between them to provide useful insights regarding the final microstructure.

In this article, considerations were ordered starting from composite concept, which deal with the choice and validation of the composite system, intrinsic parameters regarding raw material selection, up to extrinsic parameters related to processing parameters within the scope of powder metallurgy. The aim of the following sections is to increase the chances of obtaining the desired microstructure and of helping to understand the underlying phenomena that influence it. For such purposes, this review reports and analyzes some examples found in the literature.

It should be mentioned that there are many other phenomena related to sintering and in situ reactions that may be described using thermodynamics. However, in this paper, the goal is to use thermodynamic resources to perform calculations that easily yield results that can be used as criteria for decision making regarding an in situ composite system of choice, even before any experiment is carried out.

We believe that, through such systematic analysis, it is possible to decrease experimental effort or to conduct it in a more precise manner to enhance the possibilities and quality of future experimental contributions regarding this topic.

2. Concept

In the design of discontinuously reinforced metal matrix composites, the matrix tends to be chosen first according to the desired combination of properties: aluminum and titanium for high specific strength, iron for cost effectiveness and high strength, nickel for corrosive environments and high temperatures, and copper for high electrical and thermal conductivity. In the meantime, the reinforcement particles analyzed in this review are mostly selected to increase wear resistance and strength. Carbides, nitrides, oxides, and borides of transition metals are traditionally used in the industry as reinforcement phase in such metallic composites for their high hardness and wear resistance [20]. Additionally, intermetallics such as [21], AlxTiy [22], AlxNiy [23], and CuxZry [24] are used as well. Like ceramics, these materials are brittle in their pure form, and display elevated hardness and mechanical strength up to high temperatures. The reinforcement compound can either be based on the metal matrix itself, as in an Al + Al_2O_3 system, hereby called A + AB type, or based on another metallic compound, as is the case for a Fe + TiC composite, hereby called A + BC composite. Moreover, reinforcements such as graphene (reactions of graphene reinforced in situ composites are not described in this section because they belong to a very specific setup, and thermodynamic considerations regarding its intrinsic parameters are out of the scope of this work) have also been reported [25].

Oxide dispersion strengthened (ODS) steels bear many similarities with in situ metal matrix composites in view of the fact that, like many in situ composites, their processing involves high-energy ball milling, powder compaction, and precipitation of thermodynamically favored phases upon thermal treatment. Nevertheless, we consider this class of materials to be out of the scope of this review for two main reasons: firstly, the amount of oxides present in such materials is very low—usually below 1 wt.%—so that we find it to be more closely related to, for instance, a ferrous alloy containing very small fractions of insoluble carbides rather than an in situ composite. Secondly, is it a well-established processing technique which has such vast literature on the subject that it deserves a review of its own.

Additionally, although techniques such as SHS, exothermic dispersion (XD), and combustion synthesis may be related to powder metallurgy, mostly because reactants are often used in powder form, those processes involve large amounts of liquid phase and no isothermal control due to the self-propagating/combustion character of the reaction. Because of that, they do not bear many similarities to powder metallurgy and both processing and thermodynamic considerations in our review do not cover such techniques very well. Some scientific production on additive manufacturing involving SLM has also been excluded from this work for the same reason. Nevertheless, SHS, combustion synthesis, and exothermic dispersion can be used as means to produce in situ composite powders, which can in turn be used in powder metallurgy [26,27]. Some robust scientific reviews on the particularities of such processing methods have been published by Tjong [26] and Subrahmanyam [28].

We have also found reports in the literature of in situ metal matrix composites in which the dispersed phase is not conceived to act as a reinforcement [29,30]. Those studies were deliberately left out of the scope of the review. Although we recognize the relevance and innovation of such works, we believe they do not share most of the design criteria and considerations hereby discussed.

2.1. Validation of the Composite System

A useful first step in designing in situ composites is to analyze whether the desired reaction is thermodynamically possible. The two following criteria help to evaluate whether a matrix/reinforcement system has good chances of being formed in situ, and are detailed in sequence:

- Gibbs free energy criterion: the combination of desired phases should at least have a lower Gibbs free energy than the initial raw materials or, ideally, be stable upon equilibrium;
- Reinforcement dissociation criterion: the elements that are conceived as reinforcements should have sufficiently low solubility in the matrix.

2.1.1. Gibbs Free Energy Criterion

Given that in an in situ composite system raw materials react and form the intended matrix and reinforcement, such composite must have lower free energy than the selected reactants. One straightforward method to be sure of that is to check if the phases of interest correspond to a state of minimum free energy for the composition in question. If a combination of phases is the lowest free energy form of a system, all raw material combinations tend to transform accordingly. Unlike what is sometimes implied in the literature, it should be highlighted that it is not sufficient for a reinforcement to have low free energy by itself: instead, the whole set of phases in the composite, i.e., reinforcement and matrix, must be stable in the presence of one another.

Titanium borides are a good example of why free energy of formation of the reinforcement alone cannot be used as a criterion for a composite feasibility: as in [31], a mixture of 34.14 wt.% TiB_2 and Ti powders—the composition of the system is, therefore, around 10 wt.% B and 90 wt.% Ti—yields a Ti + ~70% TiB composite, even though TiB has a higher free energy of formation per mole of product: −160 kJ/mol for TiB (from Thermo-Calc®) than TiB_2 −306 kJ/mol (from Thermo-Calc®). The reason why the equilibrium state of this system is TiB + Ti is because the Gibbs free energy change of the whole system, considering Ti and ~70 wt.% TiB phases, is lower compared to higher amounts of pure titanium mixed with ~34.14 wt.% titanium diboride. They are, respectively, −160 kJ/mol and −153 kJ/mol.

Depending on the number of elements, binary or ternary phase diagrams can be used to evaluate what are the stable phases for a given composition, for a system of up to three elements, as is the case for Ti-B binary phase diagram in Figure 2.

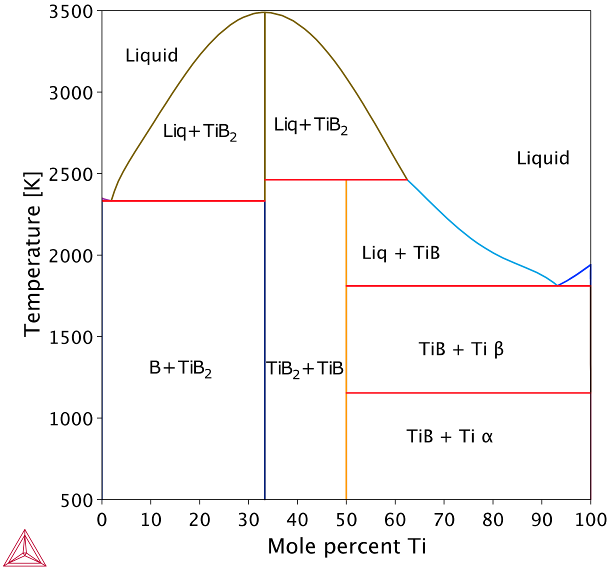

Figure 2. Simulated B—Ti phase diagram showing that Ti and TiB are the stable phases for 10 wt.% B (~77 at.% Ti).

To further illustrate the Gibbs free energy criterion, two articles found in the literature were analyzed: in the first one, Wang [32] produced a vanadium carbide reinforced ferrous alloy, starting from Fe, Fe-50 wt.% V, Fe-70 wt.% Cr, Fe-50 wt.% Mo, and carbon black powders. Samples of Fe-28.3V-6.7C-2Mo-2Cr wt.% were sintered at 1573 K in an argon atmosphere. In Figure 3, a property diagram simulated in Thermo-Calc® shows that the equilibrium state of the system is indeed Fe(Mo, Cr) + VC, not only at the sintering temperature, but actually ranging from room temperature up to the melting point. As expected from the simulations, Wang [32] obtained VC particles homogeneously dispersed in the matrix, ranging from 1 to 5 μm, and a hardness of ~770 HV.

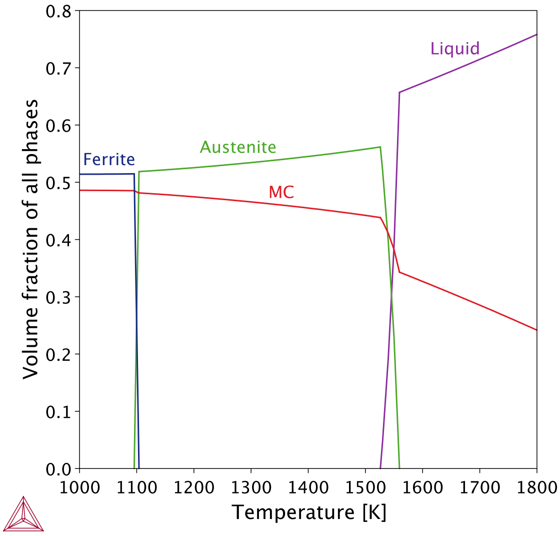

Figure 3. Fe-V-C Property diagram.

As a counterexample, Guan [33] aimed at increasing the wear resistance of a 316 L stainless steel by in situ precipitation of SiC. The precursor for SiC was a polycarbosilane (PCS) in concentrations that range from 1.5 to 7 wt.%. PCS is a silicon-based polymer that is converted into silicon-based ceramic upon heating, a class of material known as polymer derived ceramics (PDC). In Figure 4, we calculated the equilibrium state around the sintering temperature for the composites containing 1.5 and 7 wt.% PCS. The equilibrium phases were not found to be austenite + SiC, but rather austenite + chromium carbides. This happens because in this system, carbon has a higher affinity for chromium than for silicon, and silicon has high solubility in iron. In this case, even though the authors reported an increase in hardness—from 195 HV to 361 HV—and in wear resistance, the resistance to oxidation is compromised by a process known as stainless steel sensitization, i.e., chromium depletion by chromium carbide precipitation.

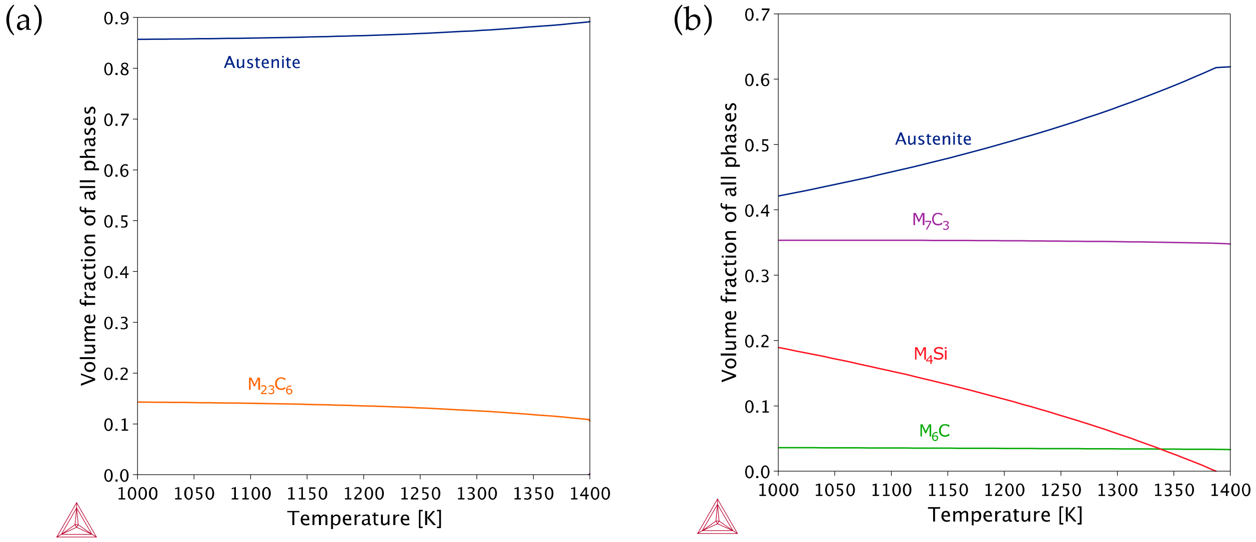

Figure 4. Property diagram of 316L with (**a**) 1.5 wt.% and (**b**) 7 wt.% PCS. M23C6, M7C3, and M6C phases listed represent carbides from the metals of the alloy of several compositions (mostly chromium), but none corresponds to SiC.

It should be noted that the thermodynamic analysis presented here also applies when more than one reinforcement phase is to be used. We chose to analyze single reinforcement systems for the sake of simplicity, and although calculations become more complex when more phases are involved, they can be computed in thermodynamic software just as easily.

2.1.2. Reinforcement Dissociation Criterion

Composite A + AB

In this composite type, elements A and B form a compound beyond a specific solubility, so that the reinforcement is based on the same metal as the matrix. The fraction of AB depends on the system's B content and the solubility of B in the metallic matrix.

For instance, Pan et al. [34], Otte [35,36], and Toptan [37] used Ti + BN for in situ formation of TiB reinforcements. No TiN can be found in any of the manufactured composites, because although titanium nitride is a very stable compound, nitrogen has very high solubility in Ti. This means that the matrix can accommodate large amounts of dissolved nitrogen upon processing temperatures, without the formation of TiN. On the other hand, B has very low solubility and TiB can be precipitated within Ti, even at very low B contents.

Composite A + BC

In this system type, the metal(s) in the reinforcements are not the same as the major element of the matrix. If the equilibrium state corresponds to low contents of B and C dissolved in the matrix, the amount of reinforcement that can be formed upon sintering is almost the same as the fractions of B and C in the system. Otherwise, if there is significant dissociation of BC reinforcement, reinforcement yield after in situ reaction is lower and could also affect the matrix properties. The reinforcement elements' solubility in the matrix can be simulated in Thermo-Calc® or in an open-source CALPHAD software.

For instance, Kwon et al. [38] developed a Ni-TiC composite based on the reaction of Ni–Ti alloy and graphite. Ti–Ni alloy presenting a weight ratio of 7:3 and enough graphite to match the molar ratio of Ti in the alloy were ball milled, compacted, and sintered at 1600 K, with a holding time of 5 min. TiC particles with size below 1 µm were obtained, leading to a hardness of 1384 HV. According to Thermo-Calc® simulations performed by us, at the equilibrium corresponding to this temperature and composition, 5.4 at.% Ti is expected to be in solid solution in the nickel matrix. It should be noted that solubility of both Ti and C decreases with the temperature and reinforcement yield at room temperature may vary according to the cooling rates. The amount of dissolved Ti may not be significant for samples with as high a ratio of Ti:Ni as the one in this paper, and it can result in solid solution hardening of the nickel matrix. For lower amounts of Ti, this could mean, however, a significant reduction in reinforcement volume fraction. Additionally, solute in the matrix can sometimes jeopardize its performance, as is often the case for copper-matrix composites that are aimed for high conductivity applications, in which reinforcement dissociation should be carefully studied, for dissolved atoms have a very negative impact on conductivity [39]. Moreover, the amount of dissolved elements in the matrix can also influence its crystal structure, such as is the case for beta stabilizing elements in titanium matrix composites.

Alternatively, it is possible to make an estimate without thermodynamic software by calculating the reinforcement's solubility product. The solubility limit is reached when the molar free energy of the solid solution is equal to the molar free energy for the formation of the compound, which is given by Equation (1), if it is assumed that *A* does not dissolve in the reinforcement:

$$m\mu_B^A + n\mu_C^A = \Delta G^{BC} \tag{1}$$

in which μ_i^A is the chemical potential of element i in solid solution in the matrix A, and ΔG^{BC} is the change in Gibbs free energy for the reaction $mB + nC \rightarrow B_mC_n$. The chemical potential of the elements in solid solution are given by Equation (2):

$$\mu_i^A = RT\, ln\left(x_i^A \gamma_i^A\right) \tag{2}$$

where x_i^A and γ_i^A are, respectively, the molar fraction and the activity coefficient of element *i* in solid solution in the matrix *A*. The product $x_i^A \gamma_i^A$ is called the activity of element *i*, represented by the symbol a_i. As elements *B* and *C* are added to the matrix, they first form a solid solution because in very low molar fractions the term $ln(x_i\gamma_i)$ is negative with a very high absolute value. By adding more *B* and *C*, the absolute value of this term decreases until it becomes equal to ΔG^{BC}. At this point, *B* and *C* reach their solubility limit and start to form the reinforcement compound. It is for this reason that, the more negative the compound-forming energy, the lower its solubility in the matrix. Combining Equations (1) and (2), the equilibrium point between solid solution and formation of *BC* can be expressed by Equation (3):

$$\left(x_B^A \gamma_B^A\right)^m \left(x_C^A \gamma_C^A\right)^n = exp\left(\Delta G^{BC}/RT\right) \tag{3}$$

Equation (3) can be used to calculate the so-called solubility product, a parameter widely used to evaluate the solubility of carbides in steels. For a given temperature, the solubility of carbide-forming elements depends on the carbon content. The higher the materials' carbon content, the greater the elements' tendency to leave solid solution and form carbides. A solubility product graph shows this dependence: for a given temperature, the solubility of an element is a function of carbon concentration. The same applies to oxides, borides, nitrides, and intermetallics.

To illustrate that, Figure 5 compares the solubility product of chromium, titanium, and vanadium in iron at 1473 K, a hypothetical sintering temperature. Chromium presents a very high solubility product in iron. Even at 3 at.% of carbon, there can be up to 17 at.% of Cr in solid solution, which means that only chromium in an excess of 17 at.% would be in the form of carbide at that temperature. On the other hand, titanium has the lowest solubility product, so in the Fe-M-C system, M being titanium, chromium, or vanadium, Ti has the highest reinforcement turnout. Therefore, among the three reinforcement candidates, titanium carbide would be the best suited for an iron matrix composite according to this criterion.

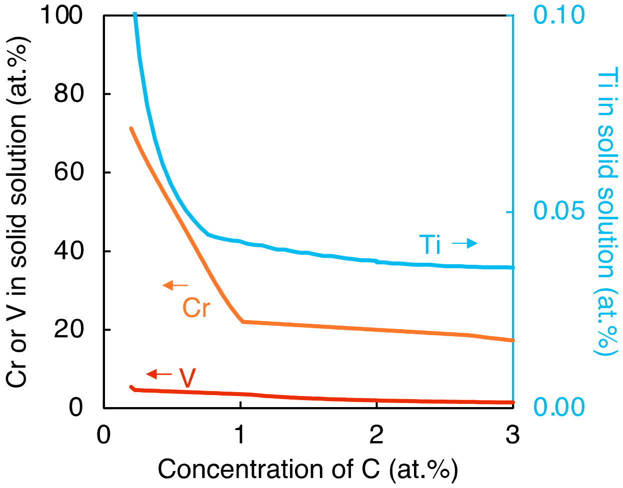

Figure 5. Simulated solubility product of V, Ti, and Cr carbides in Fe at 1473 K.

3. Intrinsic Parameters

3.1. Raw Material Selection

After evaluating whether a matrix and reinforcement set is a viable in situ composite, one must select raw materials that recombine to form the selected phases. Depending on the starting powders, different diffusion paths can take place upon reaction, and the resulting microstructure varies accordingly. This impacts reaction rate, reinforcement size, and whether there might be defects at the interface. Moreover, the driving force for in situ composite formation depends on the reactants. An intelligent selection of raw materials implies not only cost-effective powders and processing but also a potential boost of interface bonding and particle size distribution refinement. This section aims at providing a clear comparison between the choices of reactants and factors that we believe should be considered in the selection of processing parameters afterwards. Processing variables, hereby called extrinsic parameters, are further discussed in the following section. Suggestions on simulation or at least basic thermodynamic assessments of the system prior to composite manufacture are provided whenever possible.

Moreover, we believe that a condensed, critical comparison between each system's tradeoffs can shed light on some promising new raw material systems. We hope that such examples can cover by analogy most of the approaches found in the reviewed literature listed in Appendix B.

Based on what has been found in the reviewed literature, we separated the interactions between raw materials into groups, according to the type of composite—A + AB or A + BC—and the form of reactants. This approach makes highlighting critical diffusion paths for similar systems easier, which, together with processing parameters, ultimately influence the final composite's microstructure.

3.1.1. Composite A + AB

The simplest way to form in situ composites is based on two fundamental elements A and B, which form a composite of A + AB type. Upon reaction, B converts into an AB compound, which acts as composite reinforcement. Many of such composites are those whose matrix is a strong compound forming metal, such as Ti and Al. The reinforcement particles ultimately form where B is available. If B is a solid particle, AB reinforcement presents a size like the original B powder particle. Additionally, large A powders may cause a heterogeneous distribution of the reinforcement phase around the prior A particle boundaries. Either interface mobility or diffusion controls the reaction speed, depending on which is the slower phenomenon. Table 1 summarizes raw material systems for A + AB composites produced by in situ powder metallurgy found in the reviewed literature and common features that have been identified among each reaction type. It is worth mentioning that none of the considerations regards liquid phase sintering. Figure 6 illustrates microstructural evolution for such raw material systems.

Table 1. Raw material possibilities for composites of type A + AB. ΔG is the Gibbs free energy change of the reaction, G is the Gibbs free energy of element i, and p_B is the partial pressure of B in atm. R and P subscripts in the fourth column stand for reactant and product amounts of A, respectively. For the sake of simplicity, there is no mass balance in the reaction equations. Figures in the "examples" column are meant to illustrate microstructural features listed in the summary.

Reaction	Description	Microstructural Features	Examples
$A + B \rightarrow A + AB$, B = Metal Driving Force : $\Delta G' = G_{Ap} + G_{AB} - (G_{Ar} + G_B)$	Metal matrix powder reacting with another metallic powder. The reaction generates intermetallic reinforcements.	Difference in solubility of metals causes Kirkendall porosity. Reinforcements are about the size of B particles. If B powder is too large, reaction may be incomplete.	Al + Ti → Al + Al$_3$Ti [40] 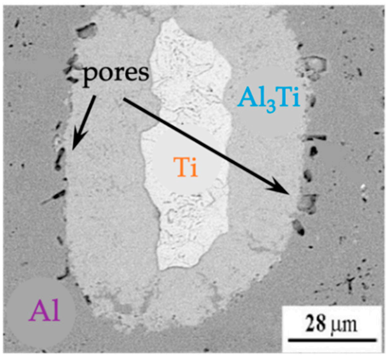
$A + B \rightarrow A + AB$, B = Nonmetal (solid) Driving Force : $\Delta G' = G_{Ap} + G_{AB} - (G_{Ar} + G_B)$	Metallic matrix powder reacts with a nonmetal to form the reinforcement. If the nonmetal presents some solubility in the matrix, it is usually interstitial.	Reinforcements have similar size to B powder particles. Reinforcement yield may vary according to the stoichiometry range of the AB compound.	Ti + C (Graphene) → Al + TiC [41] 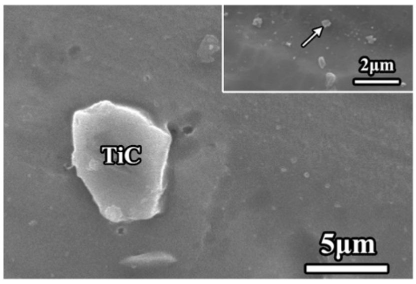
$A + B \rightarrow A + AB$, B = Nonmetal (gas) Driving Force : $\Delta G' = G_{Ap} + G_{AB} - (G_{Ar} + RTln\ (p_B))$	The atmosphere reacts with the matrix powder to generate reinforcements. It is usually performed in powder form or in porous compacts.	Reinforcements are located at prior particle boundaries.	Al + O$_2$ →Al + Al$_2$O$_3$ [42] 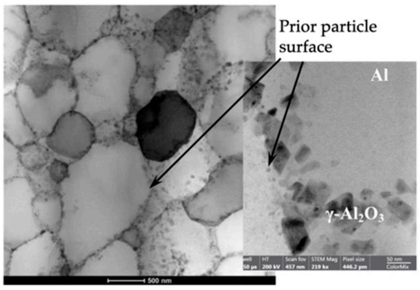

Table 1. *Cont.*

Reaction	Description	Microstructural Features	Examples
A + BC → A + AC + AB Driving Force : $\Delta G' = G_{Ap} + G_{AB} + G_{AC} - (G_{Ar} + G_{BC})$	Metal matrix powder reacts with a compound powder. BC compound becomes two types of reinforcements by reacting with the matrix.	AB and AC form near BC reinforcements, so a cluster of nuclei forms at former BC particles. Microstructural evolution relies on the stability of BC [16]. Coherent and semi-coherent interfaces are possible.	Ti + B_4C → Ti + TiC + TiB [43] 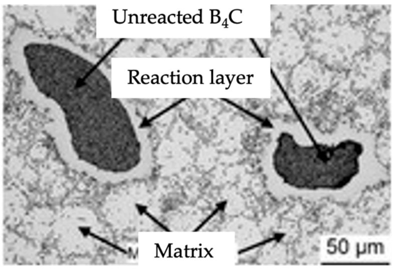
A + BC → A(C) + AB Driving Force : $\Delta G' = G_{A(C)} + G_{AB} - (G_A + G_B)$ where $\Delta G_{A(C)} = RT(x_A ln a_A + x_C ln a_C)$	Metal matrix powder reacts with a compound powder. BC dissociates and C dissolves in A, while B reacts with the matrix to become a reinforcement.	AB forms near BC reinforcements, usually as clusters. Microstructural evolution relies on the stability of BC [16]. Coherent and semi-coherent interfaces are possible. C may act as an alloying element.	Ti + Mo_2C → Ti(Mo) + TiC [44] 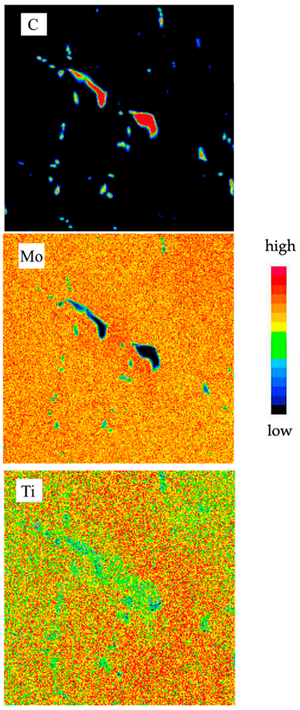
A + ABx → A + AB Driving Force : $\Delta G' = G_{Ap} + G_{ABx} - (G_{Ar} + G_{AB})$	Metal matrix powder reacts with a compound powder. Decomposition of the compound gives rise to another compound possessing a different stoichiometry.	Reinforcements grow outward from Abx. There is usually a clean and semi-coherent reinforcement interface.	Ti + TiB_2 → Ti + 2TiB [45] 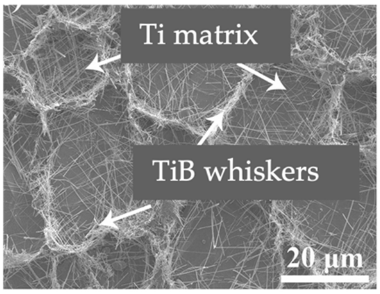

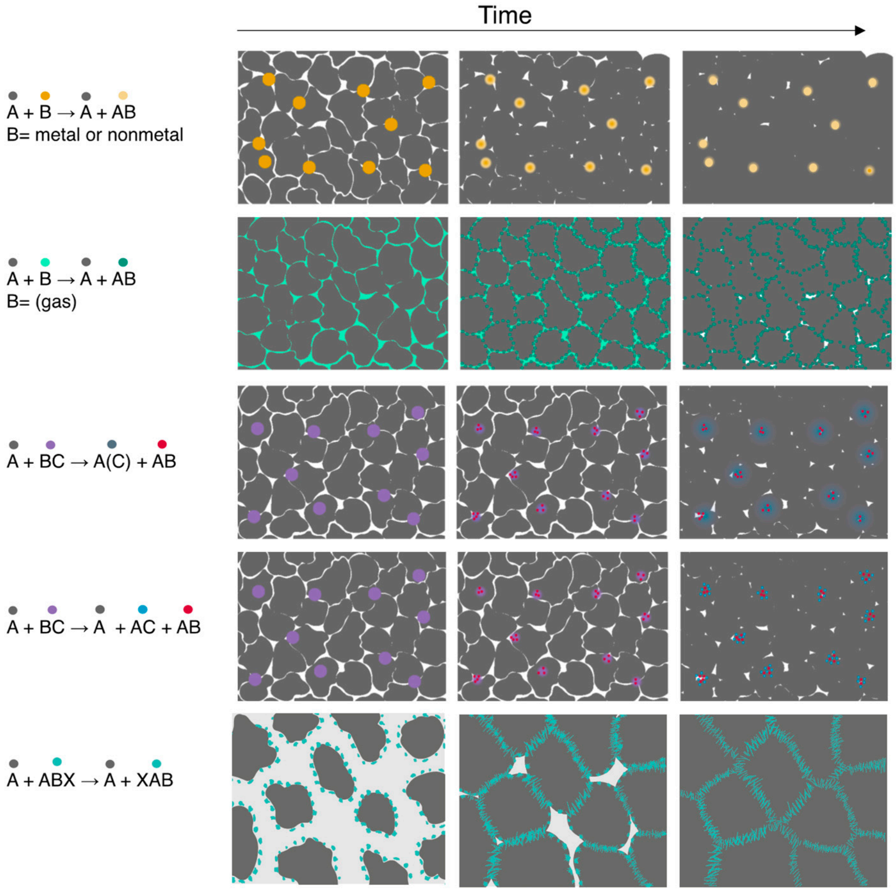

Figure 6. Microstructural evolution of raw material possibilities for type A + AB composites The pictures in the first column correspond to the beginning of the reaction (t = 0), the second column to an intermediate state of the process, and the third column to the system's final state.

3.1.2. A + BC

In this composite system, element A is the matrix, and elements B and C form the reinforcement compound. Despite the metal of the matrix not being part of the reinforcement's formula, during in situ processing, the matrix-reinforcement interactions play a role in determining potential intermediate phases and available diffusion paths, as is later discussed in the section regarding solubility and diffusion of raw materials. Table 2 summarizes raw material types used for A + BC composites into reaction systems. As before, none of the scenarios consider liquid phase assisted sintering. Figure 7 illustrates microstructural evolution for some raw material systems.

Table 2. Raw material possibilities for composites of type A + BC. ΔG is the Gibbs free energy change of the reaction, G is the Gibbs free energy of element i. R and P subscripts in the fourth column stand for reactant and product amounts of A, respectively. For the sake of simplicity, there is no mass balance in the reaction equations. Figures in the “examples” column are meant to illustrate microstructural features listed in the summary.

Reaction	Description	Microstructural Features	Example
$A + B + C \rightarrow A + BC$ Driving Force : $\Delta G' = G_{Ap} + G_{BC} - (G_{Ar} + G_B + G_C)$	Elemental powder mixture of A, B, and C. B and C reaction yields reinforcements and A becomes the matrix surrounding them.	Adhesion between matrix and reinforcement depends on A densifying around BC. The differences in diffusion fluxes between raw materials determines the final microstructure.	Al + Ti + B → Al + TiB_2 [46] 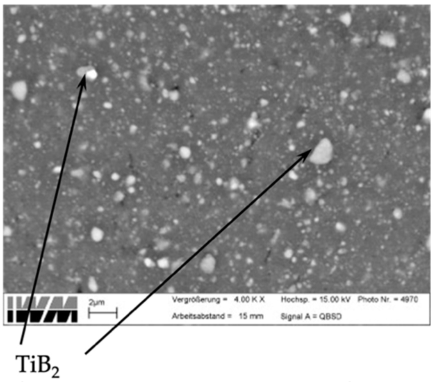 TiB_2 (similar size to initial B powder)
$AB + C \rightarrow A + BC$ Driving Force : $\Delta G' = G_{Ap} + G_{BC} - (G_{AB} + G_C)$	Less stable compounds are selected as raw materials for obtaining A + BC composites. Usually an intermetallic compound reacting with a nonmetal.	Reinforcement fraction is defined by the stoichiometry of the AB compound. Microstructure is mostly defined by the diffusion flux of B and C in A.	FeV + C → Fe + VC [47] 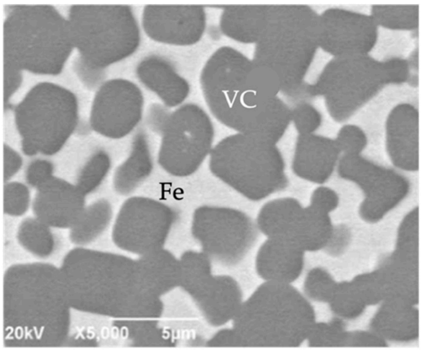
$A(B) + C \rightarrow A + BC$ Driving Force : $\Delta G' = G_{Ap} + G_{BC} - \left(G_{A(B)} + G_C\right)$	Composite is formed through a reaction between an elemental powder and a solid solution.	If the flux of C towards B is significantly larger, precipitation of BC compounds occurs within A. If the flux of B towards C is more intense, it is likely that reinforcements would have shapes and sizes similar to C particles.	Cu(Gd) + Hu2 → Cu + Gd2O3 [48] 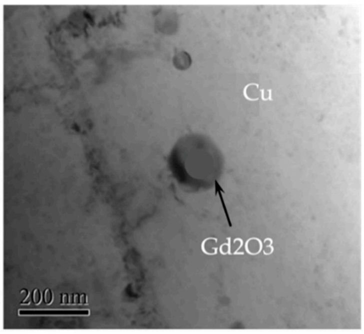

Table 2. *Cont.*

Reaction	Description	Microstructural Features	Example
$A(BC) \rightarrow A + BC$ Driving Force : $\Delta G' = G_{Ap} + G_{BC} - G_{A(BC)}$	A, B, and C form a single solution, which, upon heating, precipitates BC reinforcements within A.	Both B and C are dissolved in the matrix, so they nucleate and grow within it, like a classical solid state nucleation process.	Cu(Nb,C) → Cu + NbC [49] 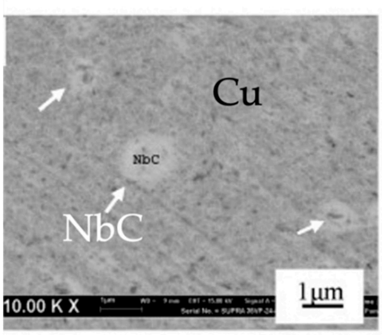
$A + BCD \rightarrow A(D) + BC$ and $A + BCD \rightarrow A + AD + BC$ Driving Force : $\Delta G' = G_{A(D)} + G_{BC} - (G_{Ar} + G_{BCD})$ and $\Delta G' = G_{Ap} + G_{AD} + G_{BC} - (G_{Ar} + G_{BCD})$	Ternary compounds, mostly MAX phases, react with the matrix releasing D. Element D either remains dissolved in the matrix or precipitates upon cooling or aging.	Reinforcement clusters are sometimes located where the former MAX phase used to be. It is possible for reinforcement distribution to become more homogeneous, if the matrix melts and wets BC clusters.	Ni + Ti2AlC → Ni + TiC + γ' [50] 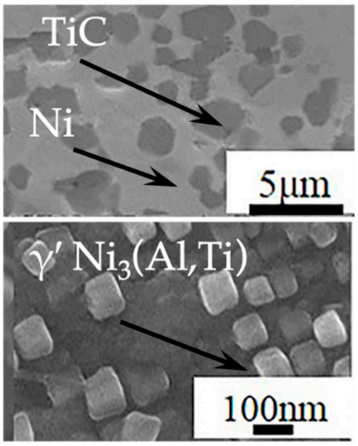

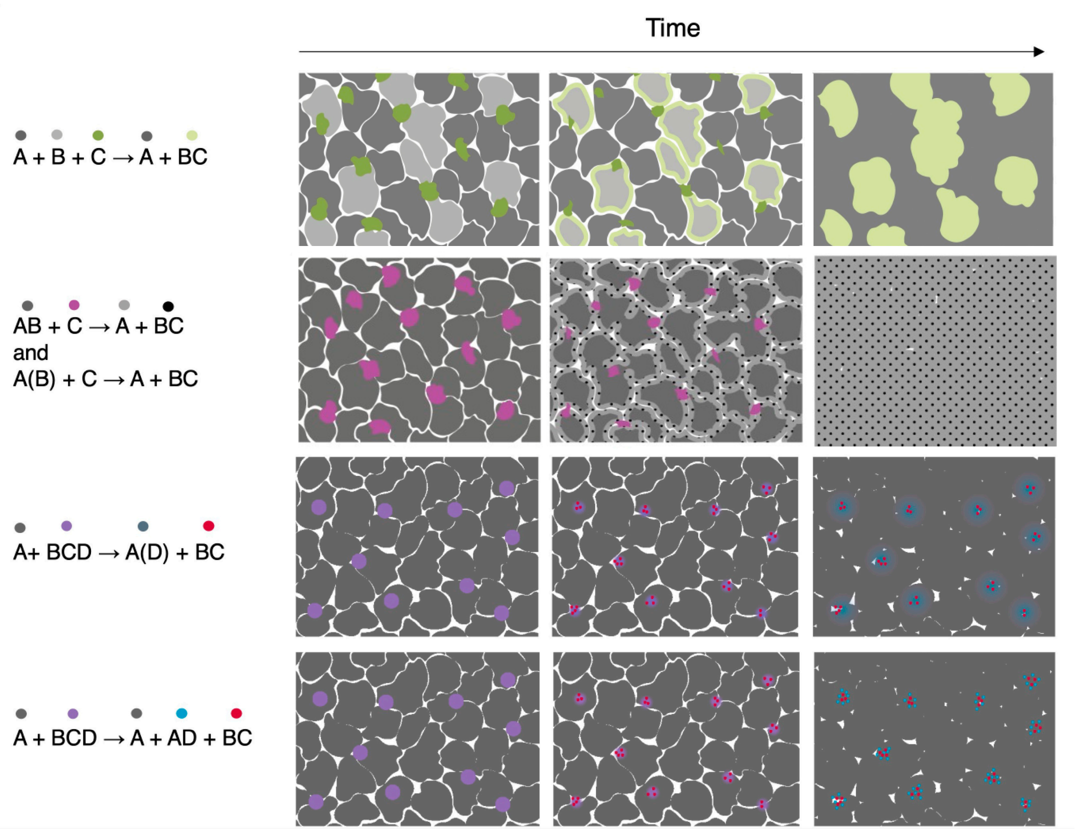

Figure 7. Microstructural evolution of raw material possibilities for composites of type A + BC. The pictures in the first column correspond to the beginning of the reaction (t = 0), the second column to an intermediate state of the process, and the third column to the system's final state.

3.1.3. Multi-System Composites

Many complex raw material reactions involving a larger number of reactants exist in the literature. As the number of elements grows, there is an increasing number of possible raw material combinations. Nonetheless, we believe that by covering the systems above, it is possible to provide general microstructural investigation tools for evaluating mechanisms and highlighting key parameters involved even in larger systems.

3.1.4. Decomposition Prior to In Situ Reactions

The raw material system may be engendered so that reduction and decomposition of raw materials take place before in situ reactions. This can be an interesting strategy for using cheaper and finer powder particles, as is the case for most metallic oxides [51]. Ghiasabadi [52], for instance, has used the process of carbothermal reduction of Fe_2O_3, TiO_2, and graphite powders to produce a TiC reinforced iron matrix composite.

Moreover, hydrides may be an alternative to protect some metals from undesired oxidation, as is often the grounds for using TiH_2. Organic materials, which sometimes even play a role in previous processing steps, as process control agents in milling or binder, can be used as a carbon source, reacting after they decompose at lower temperatures.

Nonetheless, early reduction and decomposition of raw materials should be studied carefully so that they do not negatively superimpose on reinforcement generation. Differential scanning calorimetry (DSC) and thermodynamic simulations of a compound system as a function of temperatures may provide good insights on that topic.

Figure 8 shows a simulation of the TiH_2 decomposition. When heated above 924 K, the compound dissociates into Ti and H_2. Before its decomposition, titanium is protected from residual oxygen in the atmosphere, as the latter preferentially reacts with hydrogen. Moreover, upon decomposition, the H_2 that is released can combine with residual oxygen and reduce O_2 partial pressure in the furnace. However, if TiH_2 decomposes before titanium particles can react, such particles become prone to oxidation and hydrogen's protective effect is lost.

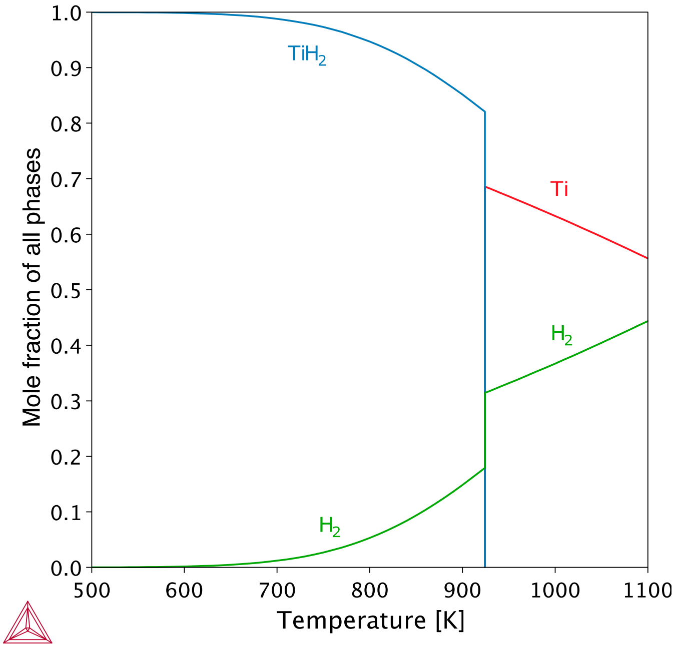

Figure 8. Simulation of phases in equilibrium in the system 1/3 mol of Ti and 2/3 mol of H as a function of temperature. Above 924 K, TiH2 becomes unstable and dissociates into H2 and Ti with some hydrogen in solid solution.

3.2. Parameters Regarding In Situ Reactions

3.2.1. Driving Force of Raw Materials' Reaction

It should be mentioned that, for the sake of clarity, mass balance has been intentionally removed from reaction equations in the first column of Tables 1 and 2. Nevertheless, in reactions such as A + B → A + AB, the amount of A on the right-hand side of the equations is less than on the left-hand side, for a percentage—corresponding in stoichiometric ratio to the amount reacted with B—has reacted to form the AB compound.

The equations for driving force described above can be used as comparison criteria between different raw material possibilities within the same composite (in the intended comparison, the final composite is the same for all raw materials, so it is not necessary to portray the Gibbs free energy change related to elements dissolved in the matrix in the reaction equations) Selecting among reactants that cause the largest energy release in the system could be an approach to attaining high nucleation and reaction rates.

Otte [36], for instance, calculated the Gibbs free energy and enthalpy change for different reactant candidates for a Ti + TiB composite. According to the authors, there are often problems with unreacted raw materials used to manufacture TiB/Ti composites through powder metallurgy.

The equations for driving force in the fourth row of Tables 1 and 2 have been written in the most general form and absolute values. Therefore, the free energy of formation G_A is the number of moles of species A multiplied by the molar free energy of A, respectively, n_A and $\overline{G_A}$.

$$G_A = n_A\overline{G_A} \tag{4}$$

It should be pointed out that, although $\overline{G_A}$ is constant in reactants and products, the amount of this species in the reactants and products, namely n_{Ar} and n_{Ap}, are different. For that reason, in the equations for driving force, the Gibbs free energy of the matrix in the reactants and products is identified, respectively, as G_{Ar} and G_{Ap}.

For reactions taking place in the standard state, driving force equations may become much simpler, as the standard state free energy of formation of pure substances is zero, so, for instance, the reaction

$$\Delta G' = G_{Ap} + G_{AB} - (G_{Ar} + G_{A}) \tag{5}$$

becomes

$$\Delta G' = \Delta G_{AB} \tag{6}$$

3.2.2. Solubility between Elements in the Composite

The solubility between elements of the composite has a large impact not only on the validation of the composite system but is also a powerful tool for evaluating interactions between raw materials as well. As mentioned in Table 1 above, Kirkendall porosity may result from the interdiffusion between elemental metallic powders and alloys. This effect can be anticipated by comparing solubilities of one into another.

Secondly, by knowing if one of the elements is not soluble in the matrix—such as in the case of carbon in copper—it is possible to have significant insights about the reactions involved in reinforcement formation. This is because if the C element in an A + BC composite—particularly in raw materials systems such as A + B + C, A(B) + C or AB+ C—is insoluble in A, it cannot move within it, so B must diffuse across the matrix to be able to react with C. This implies that reinforcements would display similar size and distribution to C particles. This reaction path and corresponding microstructure is depicted in Figure 7 for A + B + C $\rightarrow$ A + BC reaction type.

Additionally, limited solubility and eventual formation of intermediate compounds in the interface of raw materials can be an obstacle for the intended in situ reaction. For instance, in the reaction between Al, Ti, B, and C to create an aluminum matrix composite reinforced by TiC and TiB, which is the thermodynamically favored form of this system at room temperature, there may be formation of Al_2B and Al_3Ti at the interfaces of elemental powders, namely Al and B, and Al and Ti powders, due to limited solubility between them. Those compounds are fairly stable and were often found as residue in the final microstructure as reported in [53].

It is helpful to initially study the solubility of elements and compounds using phase diagrams. Binary phase diagrams can provide information regarding the solubility of elements according to the temperature, and insights into the reaction path between two elemental powders of the system—even if the system has more than two elemental powders, each interface can be analyzed separately—as it displays the phases present from 100% A to 100% B, which will form along the interface as interdiffusion undergoes. The same applies to ternary phase diagrams when the simultaneous interaction of more than two elements are concerned. A good example of using ternary phase diagrams for predicting reaction paths on an interface can be found in [54]. Pseudo-binaries can provide precious information regarding reactions between compound raw materials, such as transient phases and, unlike ternary phase diagrams, phase stability in a temperature range. However, if on the one hand binary and ternary diagrams can be easily found in the literature, and we recommend experimental data to be preferred, whenever available, specific pseudo-binary diagrams are hard to come by. Fortunately, diagrams can be rapidly simulated with the help of CALPHAD software such as Thermo-Calc®. Such simulations even provide phase composition at all points of the diagram.

For instance, Li [55] used Fe_2Ti e B_4C to create TiB and TiC reinforced iron matrix composites. A mixture of boron carbide powders and ferrotitanium alloy was spark plasma sintered under temperatures ranging from 1073 to 1373 K for 5 min. It is particularly interesting to map intermediate phases that would take place during diffusion in the spark plasma sintering (SPS) processes, as they are characterized by a short soaking time, and thermodynamic equilibrium may not be reached in time.

In this case, Figure 9 shows the property diagram used to simulate intermediate phases that form as the reaction progresses at the interface between Fe_2Ti and B_4C powders. It should be mentioned that from this diagram, it is impossible to know at which compositional stage the microstructure is at a given time frame, as there is no kinetic data being used. Diffusion data for such compounds is often unavailable at DICTRA and hard to find in the literature. It is, therefore, useful to visualize the compositional gradient that may develop in the interface between Fe_2Ti and B_4C powders, as it is expected to transit between all phases in the diagram. The phase diagram in Figure 9 has been simulated in Thermo-Calc®.

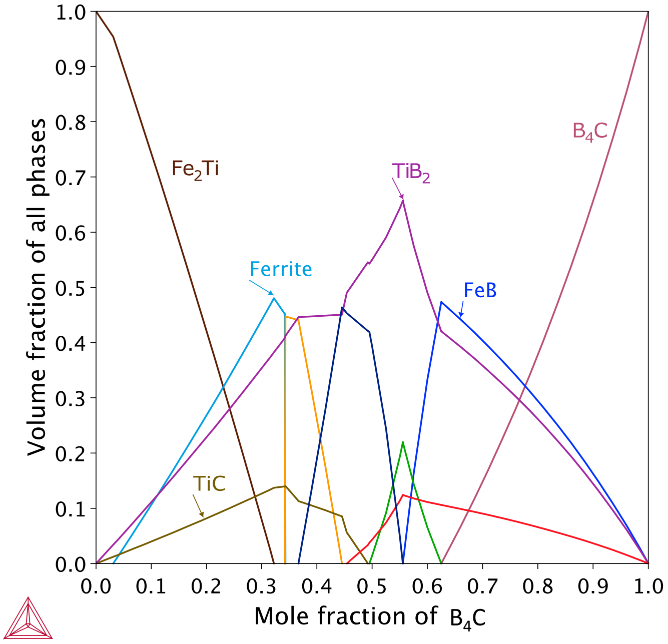

Figure 9. Fe_2Ti—B_4C property diagram simulated in Thermo-Calc® for 1223 K.

From the XRD results in Figure 10, it is possible to see that phase evolution is similar to the phase diagram: for lower temperatures (a) and (b), which are at room temperature and at 1073 K, respectively, as very little diffusion is taking place, only the phases corresponding to raw materials were detected. As the temperature increases to 1173 K and powders diffuse into one another, FeB and TiB_2 are detected as well, which corresponds to low amounts of B_4C diffusing into Fe_2Ti. At 1223 K, FeB is no longer detected, and TiC is formed. All the phases present in the sample sintered at 1223 K were predicted by the property diagram in Figure 9. In all instances, α-iron was detected because measurements were performed after the samples were cooled. Fe_2Ti is detected up to 1273 K, when it fully decomposes into Fe + TiB + TiC, which are the equilibrium phases of this system.

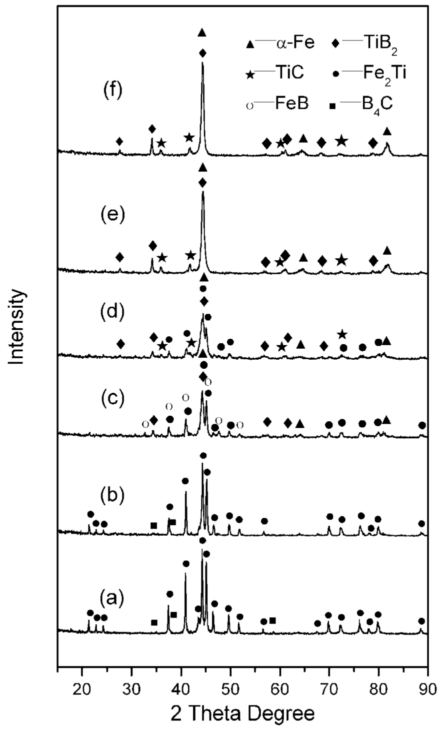

Figure 10. XRD patterns for (**a**) room temperature and sintering at (**b**) 1073, (**c**) 1173, (**d**) 1223, (**e**) 1273, and (**f**) 1323 K (reprinted from Fabrication of in situ TiB2–TiC reinforced steel matrix composites by spark plasma sintering, B H Li, Y Liu, J Li, H Cao & L He, Powder Metallurgy, copyright © Institute of Materials, Minerals and Mining, reprinted by permission of Taylor & Francis Ltd., http://www.tandfonline.com (accessed on 27 October 2022) on behalf of Institute of Materials, Minerals and Mining).

3.2.3. Diffusion during In Situ Reactions

After a thermodynamic assessment of the composite system, it is an excellent resource to, whenever possible, evaluate diffusion fluxes of raw materials upon sintering. By knowing which element diffuses faster, a reasonable microstructural forecast can be performed. This analysis can be performed experimentally by analyzing the sintered interface of macroscopic plates in contact, each having the composition of the chosen raw materials. The interdiffusion of such plates at the sintering temperature can provide plenty of insights into the microstructural evolution of the composites. A good example of that is the work by Shahid [56]. Moreover, informative theoretical assessments can be made by using the diffusion coefficient and solubility of elements in the matrix, if not for making predictions, but for interpreting an in situ composite final microstructure.

For instance, in A + BC composite systems, particularly in raw materials systems such as A + B + C, A(B) + C, or AB+ C, if there is a large difference in diffusion coefficients between B and C, it is possible to make an estimate of where in situ reinforcements are likely to be created.

The distance d traveled by a species from the starting point in time t can be approximated using the diffusion coefficient D of said species—in one dimension—by the mean square displacement $\langle d^2 \rangle$ relationship below [57]:

$$\frac{\langle d \rangle}{t} = 2D \tag{7}$$

As an example, Lee et al. [19] produced in situ TiC reinforced iron matrix composite, from the reaction of carbon black, titanium hydride, and Fe powders. In that system, the obtained microstructure results from carbon diffusion towards elemental Ti to form TiC. This happens because in that system the diffusion flux of carbon through Fe is much higher than that of Ti. The diffusion flux is dependent on both diffusion coefficient and concentration gradient. However, because the diffusion coefficient of carbon in iron (5.7×10^{-10} m^2/s) (from Thermo-Calc®) is three orders of magnitude larger than titanium (2.2×10^{-13} m^2/s) (from Thermo-Calc®) at the sintering temperature (1673 K), the difference in solubility between the two species, i.e., C and Ti, is negligible. The result is that before the interdiffusion between iron and titanium can take place, carbon would already have diffused to titanium and formed the carbide. This results in TiC formation where Ti powder particles used to be.

The same assessment could be performed by comparing the differences in microstructure when reacting Fe(C) + Ti and Fe(Ti) + C in the solid state. The former would yield a similar microstructure to the previous example, as C can reach titanium particles' surface faster than Ti would diffuse significantly into the matrix. Alternatively, in the latter case, the raw material selection would lead to nucleation and growth of TiC precipitates, as titanium is already homogeneously distributed in the matrix. Liquid phase reactions may be more complicated as all elements may be dissolved prior to reaction and diffusion becomes orders of magnitude greater.

3.2.4. In Situ Composites through Atomization

Apart from the aforementioned reaction systems, it is also possible to obtain composite powders through atomization. Unlike the reactions between powder and gas that are summarized in the third row of Table 1, reinforcements can also be precipitated from elements that are either previously dissolved in the melt and form upon fast cooling of droplets [26,58] or that precipitate in the molten matrix upon the mixture of master alloys melts [26].

Shi et al. [56] used the latter approach to produce Cu-TiB_2 composite powders through gas atomization. Cu, Ti, and B were used to produce Cu–B and Cu–Ti master alloys by induction melting. Then, at 1673 K, both melts were mixed to form the TiB_2 within the molten copper. The composite was solidified in powder form by atomization.

Though many considerations regarding the thermodynamic validation of the composite system and extrinsic parameters apply for reinforcements obtained upon atomization, reaction kinetics bear more similarities with other in situ techniques that take place in liquid state, such as rapid solidification processing (RSP) and Mixalloy Process [26].

4. Extrinsic Parameters of In Situ Composites

Bearing in mind the intrinsic characteristics that are most critical to a composite and raw material system, it is possible to calibrate extrinsic process parameters, such as temperature, time, atmosphere, etc., to meet the demands of each, as well as refine operations so that the results come out according to the intended microstructural design.

Some thermodynamic aspects of in situ composites sintering are very akin to those of general powder metallurgy, and do not belong to the scope of this review because they have already been extensively analyzed elsewhere [59]. Therefore, we focused on aspects that deal with specificities of in situ composites and relate to processing parameters.

4.1. Milling

Milling of reactants plays a more significant role in the in situ composites than those MMCs obtained by traditional ex situ methods because milling is not only necessary for homogenization and reinforcement size reduction, but in this case, it can affect the resulting in situ reactions, for there may be a change in reaction paths and kinetics of reactants.

In the first instance, high-energy milling can reduce powder particle size, affecting the final microstructure according to the type of raw material system. As previously mentioned, finer particles may display a lower mean free path of diffusion and sometimes reduce final reinforcement size. What is more, particle size reduction and defect density increase also promote enhanced diffusion and lower the activation energy for in situ reaction, which can allow for lower temperatures for reactions and sintering [60].

Because of those two factors—size reduction and increased defect density—the amount of energy stored within the material is so high that it might overcome the free energy of in situ reaction and reinforcements are able to form upon milling.

In [23], the authors produced Al_2O_3 + AlxNix reinforced aluminum composites. The authors produced the composites by reaction between Al and NiO using two approaches: milling accompanied by reaction—thereby called reactive milling—followed by hot pressing, and in situ reaction upon sintering—thereby called reactive sintering—of milled powder.

Powders presenting different Al:NiO ratios, namely 5:3, 7:3, 15:3, and 20:3, were milled in a shaker mill. A thermocouple was attached to the milling vial to detect if an in situ reaction—which is exothermic—took place upon milling. Only powders presenting a ratio of 20:3 did not react upon milling.

Among the reaction milled powders, it has been observed that the reaction takes place faster for the 5:3 and 7:3 composites, and only Al, Al_2O_3, and AlN phases were detected. Powders displaying a 15:3 ratio took longer to react and display Al, Al_2O_3, Al_3Ni, and Al_3Ni_2 phases. Moreover, more dilute NiO mixtures also have a more refined microstructure. Both characteristics are likely due to the reactions occurring at different temperatures, according to the amount of reinforcements being formed due to increased NiO amount.

The authors hot pressed both 15:3 and 20:3 powders under the same conditions. It has been found that samples produced with reaction milled powder display higher porosity, because of the hardness of in situ reinforcements that were produced upon milling, which in turn hampers compressibility of the powders. Nevertheless, composites obtained by reactive sintering display lower hardness, because a 20:3 proportion yields lower amounts of reinforcements.

Moreover, elemental powders can be turned into a solid solution outside the equilibrium composition or the equilibrium temperature. Mechanical alloying is a processing technique that uses high-energy ball milling to produce equilibrium and non-equilibrium solid solutions through deformation energy promoted by the impact of balls and powder. That is especially interesting when dealing with $A(B) + C \rightarrow A + BC$ reactions, for reinforcement yield could be increased by dissolving a higher amount of B in the matrix before reaction with C. The energy of milling required to form a solid solution can also be evaluated in open-source software [61], which uses Miedma's model to calculate an alloy's entropy of mixing [62–64].

Miedema's method is a simple method to determine the enthalpy of mixing of solid solutions and amorphous phases [65,66]. Aguilar et al. [67] determined Gibbs' free energy of mixing for the Ti-Nb-Ta system, as illustrated in Figure 11. From the ΔG of mixing, milling operations can be designed to provide the required deformation energy to stabilize such phases.

It should be highlighted that such powders, particularly those in which reinforcement has already precipitated, usually present high hardness, which hinders compressibility and, therefore, may present challenges related to powder metallurgy, i.e., to attain high green density [68]. Additionally, because often long, high-energy milling times are required, powder processing tends to be expensive. Therefore, unless one can identify niche markets for mechanical alloying, cost may become prohibitive. Additionally, aspects involving consolidation and the contamination of particles have also been reported to rank among the main obstacles for mechanical alloying industrialization. Very large amounts of scientific production in the field of in situ synthesized metal matrix composites use mechanical alloying to obtain their final products and it is important to have in mind that technological relevance of such developments is often conditioned to affordably produce large quantities of material, especially when one of the main claims of a study is that it is economically more advantageous over ex situ techniques. Nevertheless, authors such as [69] report successfully implementing MA for tailored, high-added value composites.

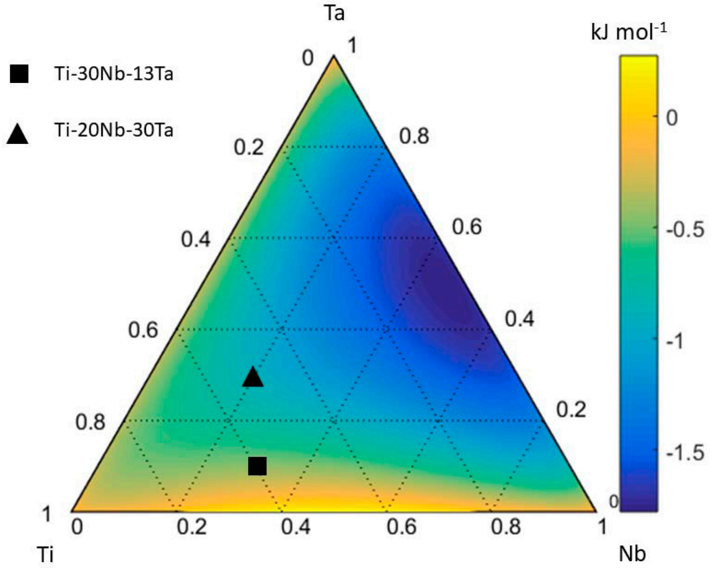

Figure 11. Ternary diagram of Gibbs' free energy for the Ti−Nb−Ta system at 298 K (reproduced with permission [67]).

4.2. Time and Temperature

4.2.1. Nucleation and Coarsening

Oftentimes, in situ and sintering are performed in a single thermal cycle, even though there are reports of powders that underwent special processes in which reinforcement formation took place before the sintering stage [70–75]. High temperatures and long reaction periods on the one hand may help in situ reactions and densification, when sintering is simultaneous to those reactions, but on the other hand, they also favor nucleation of larger reinforcements and accelerated coarsening of them.

Viljus [76] developed an in situ (Ti, Mo)C-Ni composite using a sintering cycle composed of two dwellings periods. Ti (62.2 wt.%), Ni (16.7 wt.%), C (12.8 wt.%), and Mo (8.3 wt.%) powders were vacuum sintered first at 1273 K for 1 hour, a dwelling time and temperature designed for the in situ synthesis of carbides to be completed. After precipitation took place, a second heating segment was performed for sintering the matrix to its final density. It was considered that going directly to the sintering temperature would cause critical radius for precipitation to be larger and, therefore, a smaller number of larger precipitates would tend to be formed directly. It was found that optimum sintering temperature for such a composition to be 1773 K, for it gave rise to a hardness of 1451 ± 22 HV10, transverse rupture strength of 956 ± 64 MPa, and fracture toughness of 10.59 ± 0.30 MPa $\sqrt{m}$. Although those properties are comparable to commercial ex situ composites (etalon cermet), the authors [76] did not make a comparison with the same in situ composites without dwelling time at 1273 K for validation of the proposed sintering cycle strategy. Depending on the kinetics of coarsening, sintering itself may cause reinforcement growth upon sintering, even though reinforcements have been formed at a lower temperature.

As for coarsening itself, besides high temperature and long sintering time, high interfacial energy also increases the driving force of coarsening. Moreover, reinforcement dissociation—which was already estimated in the sections before—as well as the mean free path between reinforcements can increase coarsening kinetics. Considering the mean radius of the precipitates to be r_0 when sintering starts, after a time t has passed, the mean radius increases to r_t according to the relation [77]:

$$(r_t)^3 - (r_0)^3 \propto XD\sigma t \tag{8}$$

where X and D are, respectively, the solubility and the diffusion coefficient of the precipitate in the matrix, and σ is the interphase interfacial energy [77]. A more detailed description of coarsening that considers the size distribution can be found in the work of Lifshitz, Slyozov, and Wagner [78,79].

Although Thermo-Calc® software proposes equations for estimating coalescence using mobility data and interfacial energy of a precipitate in a given matrix, it is not always possible to use it to effectively estimate coarsening because it is still very challenging to find accurate values for interfacial energy in the literature.

4.2.2. Densification

In addition to attaining in situ formation of the composite, sintering can be challenging because reinforcement particles, particularly the smallest ones, tend to block mass transport required for densification [80,81]. What is more, the reaction between raw materials can be accompanied by shrinking. In other words, as the reaction takes place, additional porosity appears as denser phases are formed [82].

To reach effective sintering, and low coalescence, methods that use fast heating and high pressure are adopted to enable higher density in those composites, while avoiding coarsening that would take place in classical, pressureless sintering. In the majority of reviewed articles (see Appendix B), authors used special techniques such as hot pressing, hot isostatic pressing, and, particularly, spark plasma sintering.

In [75], the authors adopted spark plasma sintering as a sintering technique for attaining densification of nanoreinforced Fe + TiB_2 in situ composite powders, which would otherwise coarsen at the temperatures required for densification under pressureless sintering. Firstly, a mixture of Fe and TiH_2 aiming at a final composite Fe-40 wt.% TiB_2 was high-energy ball milled and heat treated at 1173 K to obtain nanoreinforced powder particles, which would be subsequently consolidated. To attain a similar densification at pressureless sintering and SPS, powders were sintered, respectively, at 1673 K and 1353 K. It has been found that reinforcements that underwent traditional sintering display several micrometers while SPSed ones are as small as 5 nm. Their hardness is 840 ± 70 HV20 and 1560 ± 130 HV20, respectively. The wear rate of composites obtained by SPS decreased by one order of magnitude.

Though SPS-related research at laboratory scale has shown promising results, industrialization of components using such techniques is yet limited. SPS scalability is a major problem from both technical and practical points of view, mainly because larger samples are challenging to produce, and the cost of manufacture is elevated. High-added value applications may benefit from the performance granted by such techniques, but in most applications, SPS use can offset the cost-effectiveness of other attributes of in situ composites [83,84]. Moreover, as the principle of SPS is based on electrical conductivity and in situ synthesis relies on a mixture of powders presenting variable electrical properties, it can also be challenging to determine the temperature throughout the sample precisely as well as to control it, leading to uneven heating, which in turn also restricts its use in components presenting complex geometries. Moreover, although pressure assisted sintering techniques, particularly SPS, can enhance sintering speed, in situ reinforcement reaction kinetics may not be accelerated to the same extent. Many reviewed works added a post treatment of further soaking time to ensure reaction completion [36].

In both pressure assisted and conventional sintering techniques, many authors use temperatures that at least partially melt raw materials, so that rearrangement of particles and dissolution-precipitation in the liquid can favor densification. Viljus [76], for example, used 40 wt.% Ni, 30–35 wt.% Ti, 20–15 wt.% C, and 10 wt.% Mo powders as starting materials to form (Ti,Mo)C–Ni alloy composite. Milling was performed in an attritor mill with BTP ratio of 5:1 at 560 rpm for 6 h. During high-energy milling, graphite is smeared onto powder particles and reacts with Ti and Mo during heat treatment to form (Ti, Mo)C at 1273 K. The as-milled powders were pressed to compacts and then heated in a vacuum furnace at 1673 K for 30, 150, and 300 min. At 1273 K, (Ti, Mo)C has already precipitated. Above 1573 K, there is liquid phase assisted sintering. The longer the stage of liquid phase sintering, the more pronounced the carbide particle growth, as shown in Figure 12.

The solidus temperature, even for complex systems, can be estimated via one axis equilibrium calculations via software, such as Thermo-Calc®. It should be mentioned, however, that permanent liquid phase sintering is very sensitive to temperature variations, as a slight oscillation in temperature can dramatically change liquid phase fraction, and can lead to undesirable amounts of liquid, particularly because sometimes the equipment is not suitable for large amounts of molten material to be formed upon sintering [85]. One example of that is by Lee et al. [19] which used carbon black powder, titanium hydride, and an atomized steel (equivalent to AISI D2, as listed in Table 3). Powders were mixed aiming at 30 vol% TiC, with C:Ti ratios of 0.8, 0.9, 1, and 1.1. Powders were pressed and sintered at 1673 K for 1 h. Simulations of volume fraction of phases as a function of temperature were performed in Thermo-Calc®, assuming that all carbon black reacts with TiC, are displayed in Figure 13. This analysis shows how sensitive matrix phases can be to temperature variations at this sintering condition: in an interval of only 40 K, the liquid volume fraction goes from 0 to 0.7.

Table 3. Fe alloy powder composition data from [19].

C	Si	Mn	P	S	Ni	Cr	Mo	Cu	V	Fe
1.57	0.35	0.44	0.013	0.006	0.08	11.98	1.00	0.02	0.35	Bal.

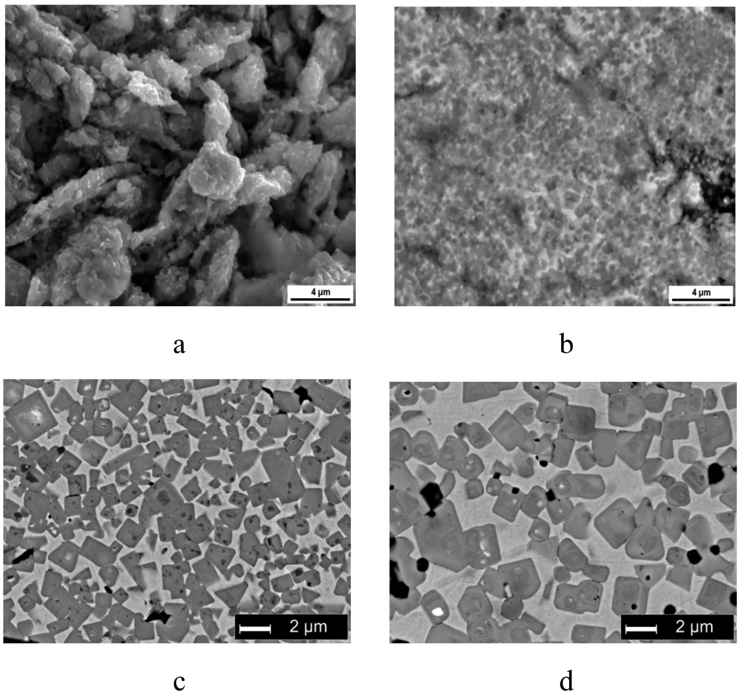

Figure 12. Volume fraction of stable phases for matrix alloy composition of Table 3 as a function of temperature. M represents the metallic atoms, with Ti being the major element.

Transient liquid phase is likely the safest way to improve density through liquid phase assisted sintering, because it depends on local composition gradients which eventually cease to exist. To evaluate the possibility of transient liquid phase, local equilibrium should be analyzed between each of the raw material interfaces upon sintering temperature.

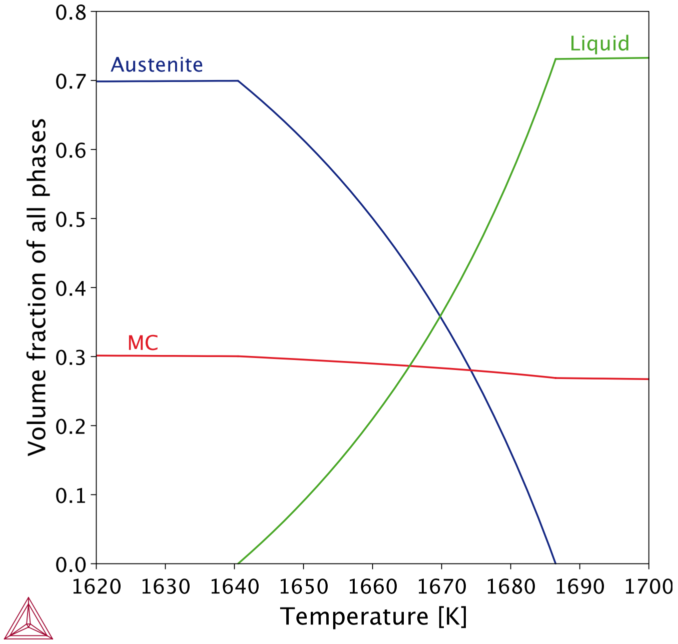

Figure 13. Micrographs showing reinforcement growth according to sintering temperature. Sintering at (**a**) 1273 K for 30 min, (**b**) 1573 K for 30 min, (**c**) 1673 K for 30 min, and (**d**) 1673 K for 300 min (reproduced with permission [86]).

Saito [86] produced in situ Ti-6.8Mo-4.2Fe-1.4Al-1.4V from hydride-dehydride pure titanium, Fe–62Mo and Al–50V master alloy, and TiB_2 powders. Samples were sintered at 1573 K for 4 h and the amount of resulting TiB ranged from 0 to 40 vol%, depending on the amount of added titanium diboride. The final microstructures display uniformly distributed needles of TiB and no residual TiB_2 was found. After hot working, samples display porosity below 1%, regardless of the reinforcement amount. The authors [86] used Thermo-Calc® to evaluate diffusion paths among powders and the results are displayed in Figure 14. According to the interaction parameters in its database, ferro-molybdenum particle is unstable in ß titanium. Because the diffusivity of iron in titanium is at least 100 times higher than that of molybdenum, iron atoms in Fe–Mo master alloy penetrate rapidly into the titanium matrix prior to molybdenum atoms. Boron, on the other hand, has very little solubility in ß titanium (<3 ppm). What results is that boron and molybdenum co-segregate and form a transient liquid phase. This phenomenon has been explained by analyzing the effect of boron on the solidus line of a Ti4Fe-Mo pseudo-binary diagram calculated by the authors, as depicted in Figure 14.

The composites containing 20% TiB [86] and 20% TIB composites display UTS: ~1700 MPa, E: ~155 GPa, fatigue strength ~1000 MPa, and the lowest wear rate among all volume percentages of TiB in the study (including TiB-free titanium). Authors claim that all properties, including hot workability, are superior to the celebrated Ti–6V–4Al alloy.

We believe that, besides liquid phase assisted sintering, several strategies that go back to traditional powder metallurgy could be used to improve densification, namely improving the green compact density and density gradients. It is well known from basic powder metallurgy theory that many defects and poor densification that become assessable after the sintering process are inherited from the green compact [71].

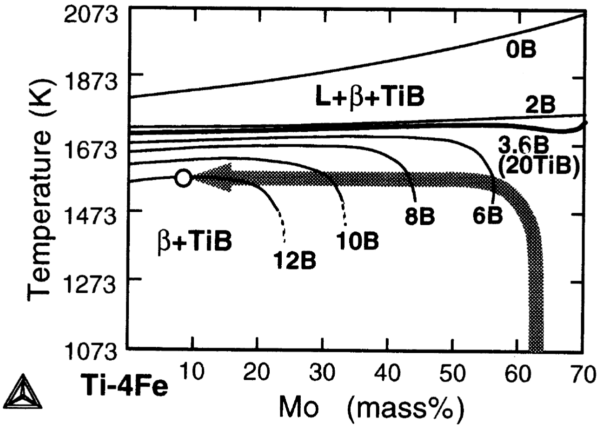

Figure 14. Effect of boron content on solidus line of Ti4Fe-Mo pseudo-binary system showing diffusion path of molybdenum during sintering (reprinted from Materials Science and Engineering: A, 243, T Saito, H Takamiya, T Furuta, Thermomechanical properties of P/M β titanium metal matrix composite, 6, Copyright (2022), with permission from Elsevier).

Panda [87] used trimodal powder distribution respecting a proportion that would allow for maximal packing density. The authors [87] selected Ti, Nb-Mo, and TiB_2 powders that correspond to a particle ratio of 45:10:2 (large:medium:small), which is very close to 49:7:1, which corresponds to the highest theoretical density for a trimodal particle distribution. When compared to β-stabilized Ti(Mo, Nb) + TiB_2 displaying a bimodal distribution, the attainable density for a trimodal distribution is 8% higher. Furthermore, the enhanced contact between particles can favor the reaction of starting powders, possibly leading to accelerated reaction, and sintering as well. This strategy is particularly interesting considering that several in situ composites use more than one kind of raw material, and that very often one already seeks to use at least one fine component to maximize reaction rate and reduce reinforcement size.

Additionally, as important as a high green density is a uniform distribution of powders and pores in the green compact. The reason for that is because pores also suffer from the Ostwald ripening effect: the large consume the smaller ones. If the interspacing between powders is similar, samples can sinter to a higher density. Strategies to control the green body microstructure and its effects include powder flowing additives, granulation of powder blend, or metal injection molding.

Operations after the sintering step, such as forging, extrusion, and post-HIP, have been very often used in the reviewed literature, as can be inferred from the bibliographic data summarized in Tables A2–A6. Their aim is to increase densification and to refine the microstructure and do not differ much from what is also done with ex situ composites.

Hot isostatic pressing is often adopted as a complement after conventional component sintering to increase density. This approach is mainly used when previous steps have already produced a highly complex part. The hot isostatic pressing process preserves the dimensions of the part, as the stresses at all points of the material are homogeneous.

Processes such as forging and extrusion imply the need for further machining operations, as it is not possible to produce a high complexity, near net shape part. In these cases, powder metallurgy is chosen thanks to the microstructural control it allows for, rather than for obtaining a finished component from the powder.

4.3. Atmosphere

During the sintering process, chemical reactions involving condensed and gaseous phases take place. When planning in situ composites, it is often important to take into account that undesirable reacting elements in the system can come from the sintering atmosphere. When composites are reinforced with intermetallics, as well as carbides, borides, and nitrides, avoiding oxidation is necessary when selecting sintering atmosphere conditions, because sometimes not only the matrix can be oxidized, but the metal reinforcement precursor may convert (at least partially) into oxide instead of the desired phase. In the case of PM in particular, powders—even compacted green bodies—have a surface-to-volume ratio a few orders of magnitude higher than ingots, so that even if a reaction with the atmosphere is restricted to the surface of the particles, both the sintering kinetics and the mechanical, magnetic, electrical, and chemical properties can be severely impaired.

It is common practice to use hydrogen in the atmosphere to prevent oxidation. The pH_2/pH_2O ratios from which the reduction of oxides is favorable can be obtained in Ellingham diagrams from the literature, such as the one in Figure 15.

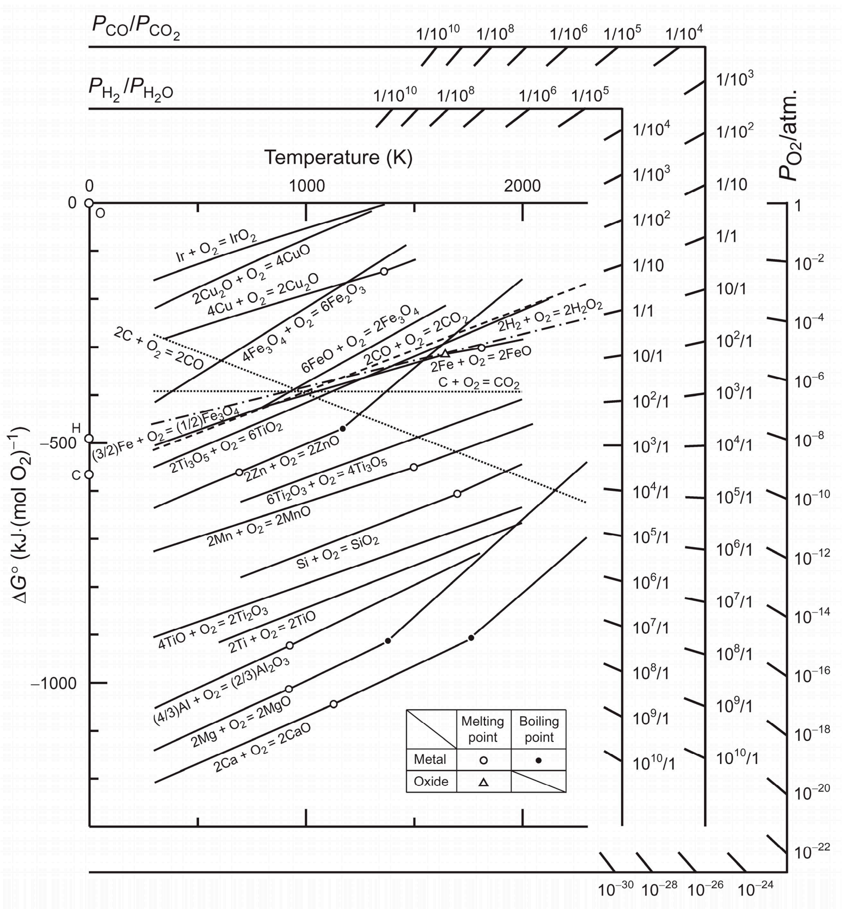

Figure 15. Elligham diagram of some oxides (reprinted from Treatise on Process Metallurgy, Volume 1, Masakatsu Hasegawa, Ellingham Diagram, 10, Copyright 2022, with permission from Elsevier).

If data regarding a particular oxide cannot be found in Ellingham diagrams in the literature, one may also calculate oxygen partial pressure for oxidation from which the reduction of oxides is favorable [88]. For a pure oxide *MO*, formed from pure solid metal *M* at a temperature *T* and a pressure *p* according to the reaction in Equation (9), the Gibbs free energy can be determined for a given temperature and pressure using Equation (10).

$$M_{(s)} + \frac{1}{2}\,O_{2(g)} = MO_{(s)} \tag{9}$$

$$\Delta G^0 = -RT\,ln\left(\frac{a_{MO}}{a_M {p_{O_2}}^{1/2}}\right) \tag{10}$$

where ΔG^0 is the change in Gibbs free energy of reaction from Equation (9), α_i is the activity of element I, and p_{O2} is the partial pressure of O_2. If both M and MO are in the standard state used to calculate ΔG^0, their activities are equal to 1. Otherwise, their activities in relation to the standard state should be used in Equation (10). For more complex systems, the expression can be generalized as Equation (11).

$$\Delta G^0 = -RTln\left(\frac{\Sigma a_{products}}{\Sigma a_{reactants}}\right) \tag{11}$$

This relationship can also be estimated via software. As an example, this calculation was performed for aluminum, iron, and chromium using Thermo-Calc® and is displayed in the graph in Figure 16. By including hydrogen in the atmosphere, it is possible to increase the acceptable amounts of oxygen impurities. To estimate how much hydrogen is required to avoid oxidation of those metals, one uses H_2/H_2O proportions instead of oxygen concentration.

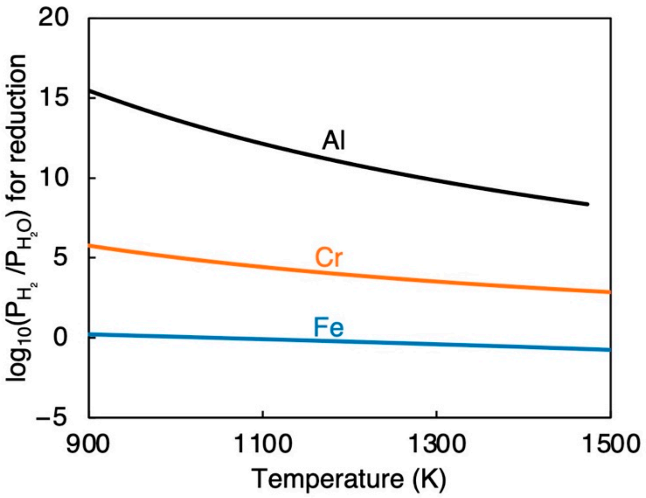

Figure 16. Simulated pH_2/H_2O ratios for reducing Cr, Fe, and Al oxides as a function of temperature.

As would be expected for materials that were selected for their ability to form very stable compounds, it can be gathered from the pH_2/pH_2O ratio in Figure 16 that a strongly reducing atmosphere is required to prevent oxidation of chromium and particularly aluminum at sintering temperatures. Oxygen traps—also known as getter agents—can also be added as sacrifice material to oxidize preferentially and reduce the amount of available oxygen in the atmosphere [88]. Those oxygen traps can be made of metals presenting higher affinity to oxygen [89], such as using magnesium as a getter agent for aluminum. A getter material can be any metal that displays lower free energy of oxidation at the given temperature, as can be easily visualized in Ellingham diagrams [89,90]. Oxygen traps can be also made of the same metal one intends to protect, using a sacrifice sample placed at a slightly cooler region of the furnace, where the driving force for oxide formation is higher. The positive slope of the free energy curves for oxides in the Ellingham diagram corresponds to a decrease in their stability as temperature increases.

Rodeghiero [91] used thermodynamic data, as shown in Figure 17, to evaluate phase combination possibilities and reduction protocol. The raw materials were Ni/Al hydroxides, prepared using an aqueous precipitation technique. Powders were heat treated before sintering, and according to the atmosphere, different composites were obtained, namely Ni + $NiAl_2O_4$ and Ni+ Al_2O_3. For Ni/Al_2O_3, a partial pressure of O_2 in the range of 10–23 and 10–24 atm, and sintering temperature of 1273 K was used, so as to lay in the γ-Ni + Al_2O_3 region of the Ni/Al/O phase diagram. To obtain Ni/$NiAl_2O_4$ composite powders, a temperature of 1373 K for 1 h and an oxygen partial pressure of 10–9.9 atm were selected. It should be mentioned that a CO/CO_2 mixture was adopted to reduce oxygen partial pressure in Ni/$NiAl_2O_4$ composites, and that it was possible because neither Ni nor Al have great affinity for carbon. This thermal treatment cycle at lower temperatures prior to sintering can be a strategy for both obtaining finer precipitates as well as for allowing proper contact with the atmosphere. Sintering atmosphere during hot pressing was also designed to preserve the desired phases. As sintering was performed at 1673 K, higher oxygen partial pressures could be used, as oxide stability decreases with temperature.

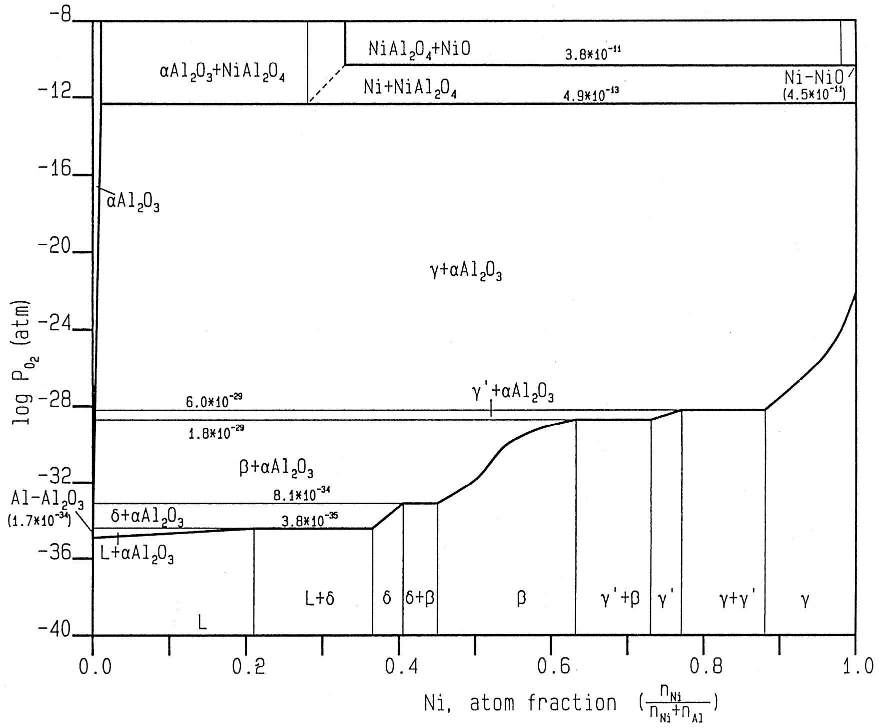

Figure 17. Ni/Al/O phase diagram for 1273K and 1 atm total pressure.

Moreover, vacuum atmosphere is often used in powder metallurgy to promote densification, because it helps promote mass transport mechanisms upon sintering, as the partial vapor pressure of metals increases under vacuum. This should, however, be carefully implemented for nitride reinforcement, which may decompose due to the low nitrogen partial pressure in the atmosphere, as indicated by the simulation shown in Figure 18.

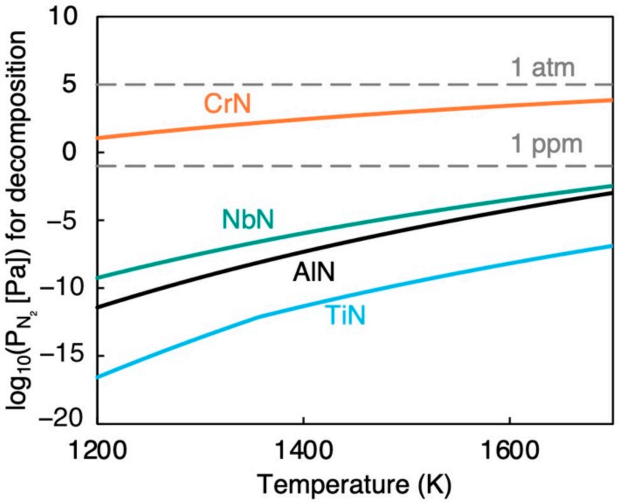

Figure 18. Simulated N_2 partial pressure for nitride decomposition as a function of temperature.

5. Concluding Remarks

In this review, over 400 papers, which correspond to all the literature we found on the subject of metal matrix composites produced in situ via powder metallurgy, have been compiled. From the analysis of the state of the art of this subject, some important common aspects regarding the design, raw material selection, and processing of such composites were observed and divided between concept, intrinsic parameters, and extrinsic parameters, as depicted in the flowchart in Figure 19.

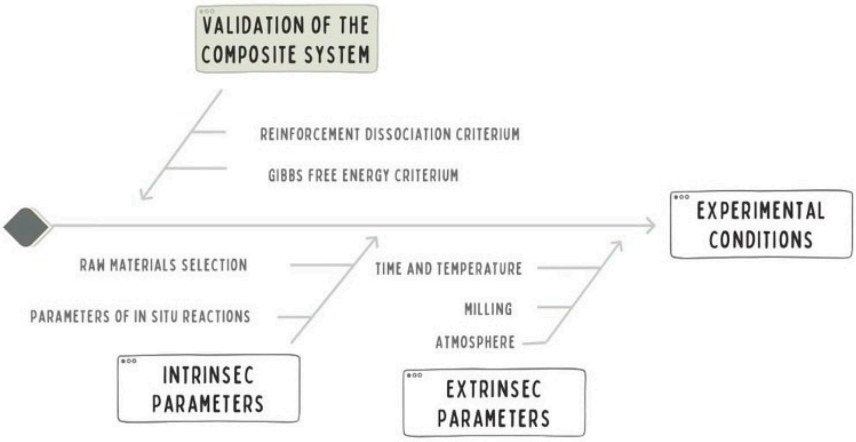

Figure 19. Flowchart summarizing parameters discussed in this review as a means of designing experimental conditions for in situ composite manufacture by powder metallurgy.

In the concept section, an analysis aiming at validating a composite as a possible candidate for in situ powder metallurgy has been carried out and Gibbs free energy minimization and low reinforcement dissociation were used as criteria.

In the intrinsic parameters section of this work, raw materials possibilities have been discussed based on the reactions that are likely to take place and the microstructure they might yield. Such reaction possibilities have been accessed through thermodynamic and kinetic features of such systems. We also outlined the equations used for calculating the driving force of such reactions, so they can be used as criteria for selecting among different reactant options.

In this work, all processing related operations have been regarded as extrinsic parameters. Temperature parameters have been viewed from the standpoint of in situ reactions and densification upon sintering.

The authors hope that this review illustrated important aspects of design in the field of in situ composites via powder metallurgy. During the development of our own composites, some drawbacks could have been avoided from knowledge and observation of previous works. However, the literature on the subject mostly deals with manufacturing of specific composites and, therefore, those design insights were scattered and oftentimes only possible by comparison of multiple systems. We expect to have summarized relevant aspects that can help conduct research in the field in a more concise manner, for we consider in situ composites a promising area for sustainable technological development. Although most simulations were made assuming thermodynamic equilibrium, and equilibrium is not always attained in experimental conditions, either due to sluggish kinetics or high activation energies, we strongly believe thermodynamic analysis in general, and simulations in particular, to be tools of inestimable value in both conducting leaner experiments and richer discussion in this field.

Author Contributions: I.S.D.: conceptualization, software, investigation, writing—original draft, and project administration; D.d.S.A.: conceptualization, methodology, software, investigation, formal analysis, and writing—review and editing; E.V.P.: investigation and data curation; R.C.D.C.: writing—review and editing; C.A.: methodology, writing—original draft, and writing—review and editing; A.N.K.: conceptualization, supervision, and writing—review and editing. All authors have read and agreed to the published version of the manuscript.

Funding: Please This research was funded by the National Council for Scientific and Technological Development (CNPq), grant numbers 308293/2019-3 and 140611/2019-3, and also by Hercílio Randon Institute (IHR).

Data Availability Statement: No new data were created or analyzed in this study, as simulations were performed on data available at the references found in the literature. Data sharing is not applicable to this article.

Acknowledgments: The authors want to acknowledge Fundação de Ensino e Engenharia de Santa Catarina (FEESC), Instituto Hercílio Randon (IHR), and CNPq (National Council for Scientific and Technological Development) for the financial support.

Conflicts of Interest: The authors declare that they have no known competing financial interests or personal relationships that could have appeared to influence the work reported in this paper.

Appendix A. Database Search Queries

In this work, the database was SciVerse Scopus. "Advanced mode" search queries were developed to find articles that fit the literature relevant for this review. The five metal matrices with the largest amount of published literature were selected. The keywords for search queries and their written forms using Booleans for Advanced Search in Scopus are disclosed in Table A1. All the articles which did not fit the scope outlined in the introduction of this review were excluded, and the remaining papers were individually read, analyzed by our team, and now compose the data found in Tables A2–A6. Although we do not aim to provide a systematic review report, all papers that are disclosed in the tables have been double checked and independently read by at least two of the authors. The last database update was performed on 13 May 2022. All papers that were not available in English were also left out.

Table A1. Scopus database search queries.

Matrix.	Specific Keywords	General Keywords	Format for Scopus Advanced Search
Aluminum	"Aluminum"; "Aluminium"; "Al"	"Matrix" "Dispers*"; "Strength*"; "Composite"; "Nanocomposite"; "Sinter*"; "Powder metallurgy"; "PM"; "MIM"; "Injection mold*"; "SPS"; "SPH"; "HIP"; "In situ"; "In-situ"; "Insitu"; "Reactive sintering"; "Diffusion alloying"	TITLE-ABS-KEY ((aluminum OR aluminium OR al) W/3 (matrix OR (dispers* AND strength*) OR composite OR nanocomposite OR cermet) AND (sinter* OR "powder metallurgy" OR pm OR mim OR "injection mold*" OR sps OR sph OR hip) AND ("in situ" OR "in-situ" OR insitu OR "reactive sintering" OR "diffusion alloying")) AND (EXCLUDE (DOCTYPE, "cp") OR EXCLUDE (DOCTYPE, "cr"))
Titanium	"Titanium"; "Ti"		TITLE-ABS-KEY ((titanium OR ti) W/3 (matrix OR (dispers* AND strength*) OR composite OR nanocomposite OR cermet) AND (sinter* OR "powder metallurgy" OR pm OR mim OR "injection mold*" OR sps OR sph OR hip) AND ("in situ" OR "in-situ" OR insitu OR "reactive sintering" OR "diffusion alloying")) AND (EXCLUDE (DOCTYPE, "cp") OR EXCLUDE (DOCTYPE, "cr"))

Table A1. *Cont.*

Matrix.	Specific Keywords	General Keywords	Format for Scopus Advanced Search
Nickel	"Nickel"; "Ni"		TITLE-ABS-KEY ((nickel OR ni) W/3 (matrix OR (dispers* AND strength*) OR composite OR nanocomposite OR cermet) AND (sinter* OR "powder metallurgy" OR pm OR mim OR "injection mold*" OR sps OR sph OR hip) AND ("in situ" OR "in-situ" OR insitu OR "reactive sintering" OR "diffusion alloying")) AND (EXCLUDE (DOCTYPE, "cp") OR EXCLUDE (DOCTYPE, "cr"))
Copper	"Cu"; "Copper"; "Brass"; "Bronze"		TITLE-ABS-KEY ((cu OR copper OR brass OR bronze) W/3 (matrix OR (dispers* AND strength*) OR composite OR nanocomposite OR cermet) AND (sinter* OR "powder metallurgy" OR pm OR mim OR "injection moud" OR sps OR sph OR hip) AND ("in situ" OR "in-situ" OR insitu OR "reactive sintering" OR "diffusion alloying")) AND (EXCLUDE (DOCTYPE, "cp") OR EXCLUDE (DOCTYPE, "cr"))
Iron	"Iron"; "Fe"; "Ferr*"		TITLE-ABS-KEY ((iron OR Fe or steel or ferr*) W/3 (matrix OR (dispers* AND strength*) OR composite OR nanocomposite OR cermet) AND (sinter* OR "powder metallurgy" OR pm OR mim OR "injection mold*" OR sps OR sph OR hip) AND ("in situ" OR "in-situ" OR insitu OR "reactive sintering" OR "diffusion alloying")) AND (EXCLUDE (DOCTYPE, "cp") OR EXCLUDE (DOCTYPE, "cr"))

Appendix B. Summary of Reviewed Literature

Table A2. Aluminum Matrix Composites.

Matrix	Reinforcement	Processing Method	Raw Materials	References
Al	Al0.5FeSi0.5	Pressureless Sintering (PS)	Al; Fe; Si	[92]
Al	Al12W	Pressureless Sintering (PS); Hot Extrusion (HE)	Al; W	[93]
AA2024	Al13Co4; Al3Y	Hot Pressing (HP); Hot Extrusion (HE)	AA2024; Al84Ni8.4Y4.8La1.8Co1	[94]
Al	Al13Fe4	Spark Plasma Sintering (SPS)	Al; Fe	[62]
Al	Al2O3	Pressureless Sintering (PS)	Al	[95]
Al(Zn)	Al2O3	Hot Pressing (HP)	Al; ZnO	[96]
Al	Al2O3	Hot Forging (HF)	Al; O2	[97]
Al	Al2O3	Hot Pressing (HP)	Al; Fe2O3; Al2O3	[98]
Al(Si,Mg,Cu)	Al2O3	Pressureless Sintering (PS)	Al; Mg; Cu; Si; SiO2	[60]
Al	Al2O3	Hot Pressing (HP); Hot Extrusion (HE); Quasi-Isostatic Forging (QIF)	Al; O2	[41]
Al	Al2O3	Hot Pressing (HP); Hot Extrusion (HE)	Al; O2	[99]
Al	Al2O3	Hot Pressing (HP); Hot Extrusion (HE)	Al; O2	[100]
Al	Al2O3	Hot Isostatic pressing (HIP)	Al; O2	[101]
Al(Zn)	Al2O3	Pressureless Sintering (PS)	Al; ZnO	[102]
Al(Zn)	Al2O3	Pressureless Sintering (PS)	Al; ZnO	[103]

Table A2. *Cont.*

Matrix	Reinforcement	Processing Method	Raw Materials	References
Al	Al2O3-(Al3Ti; Al3Zr; TiB2)	Pressureless Sintering (PS)	Al; TiO2; ZrO2; B2O3	[104]
Al	Al2O3; Al11Ce3	Pressureless Sintering (PS); Friction Stir Processing (FSP)	Al; CeO2	[105]
Al	Al2O3; Al2Cu	Pressureless Sintering (PS)	Al; CuO	[106]
Al	Al2O3; Al3Ti	Hot Pressing (HP)	Al; TiO2	[107]
Al	Al2O3; Al3Ti	Hot Pressing (HP)	Al; TiO2	[108]
Al	Al2O3; Al3Ti	Pressureless Sintering (PS)	Al; TiO2	[109]
Al-V	Al2O3; Al3V; Al10V	Pressureless Sintering (PS)	Al; V2O5	[110]
Al	Al2O3; Al3Zr	Pressureless Sintering (PS)	Al; ZrO2	[111]
Al	Al2O3; AlNi; Al3Ni; Al3Ni2	Hot Pressing (HP)	Al; NiO	[23]
Al	Al2O3; Carbon Nanotube (CNT)	Spark Plasma Sintering (SPS); Hot Extrusion (HE)	Al; Multiwalled Carbon Nanotubes (MWCNTs); O2	[112]
Al	Al2O3; CuAl2	Pressureless Sintering (PS); Hot Pressing (HP)	Al; CuO	[113]
Al	Al2O3; CuAl2	Pressureless Sintering (PS)	Al; CuO	[114]
Al	Al2O3; CuAl2	Pressureless Sintering (PS)	Al; CuO	[115]
Al	Al2O3; FeAl2; FeAl3	Spark Plasma Sintering (SPS)	Al; Fe2O3	[116]
Al	Al2O3; Si	Pressureless Sintering (PS)	Al; SiO2	[117]
Al	Al2O3; Si	Pressureless Sintering (PS)	Al; SiO2	[118]
Al	Al2O3; Si	Hot Isostatic Pressing (HIP); High Pressure Torsion (HPT)	Al; SiO2	[119]
Al	Al2O3; Si	Pressureless Sintering (PS)	Al; SiO2	[120]
Al	Al2O3; SiC; Al4C3; Si	Pressureless Sintering (PS); Hot Pressing (HP)	Al; SiO2; C	[121]
Al	Al2O3; TiB2	Pressureless Sintering (PS)	Al; TiO2; B2O3	[122]
Al	Al2O3; TiB2; Al3Ti	Pressureless Sintering (PS); Hot Pressing (HP); Hot Extrusion (HE)	Al; TiO2; B	[123]
Al	Al2O3; TiB2; TiC	Pressureless Sintering (PS); Hot Extrusion (HE)	Al; TiO2; B4C	[124]
Al	Al2O3; TiC	Hot Isostatic Pressing (HIP)	Al; TiO2; C	[125]
Al	Al2O3; TiC; Al3Ti; AlN	Pressureless Sintering (PS)	Al; C; TiO2; N2	[126]
Al	Al2O3; WAl12	Hot Pressing (HP); Hot Extrusion (HE)	Al; WO3	[127]
Al	Al2O3; ZrB2	Pressureless Sintering (PS); Hot Pressing (HP)	Al; ZrO2; B	[128]
Al	Al2OC-AlN; Al5O6N; Al7O3N5	Pressureless Sintering (PS)	Al; Al2O3; N2	[129]
Al	Al3(Zr, Ti)	Pressureless Sintering (PS); Hot Pressing (HP)	Al; Zr; Ti	[130]
Al	Al3CON; Al5O6N	Pressureless Sintering (PS)	Al; NH3; Ethylene-bis Stearamide	[131]
Al	Al3Ni; Al3Ni2; CeO2	Pressureless Sintering (PS)	Al; Ni; CeO2	[132]
Al	Al3Ti	Hot Extrusion (HE); Pressureless Sintering (PS)	Al; Ti	[22]
Al	Al3Ti	Pressureless Sintering (PS); Hot Pressing (HP)	Al; Ti	[133]
AA6061	Al3Ti	Spark Plasma Sintering (SPS)	AA6061; Ti	[134]
Al	Al3Ti	Pressureless Sintering (PS); Hot Extrusion (HE)	Al; Ti	[40]

Table A2. *Cont.*

Matrix	Reinforcement	Processing Method	Raw Materials	References
A356	Al3Ti	Pressureless Sintering (PS)	A356; Ti	[135]
Al	Al3Ti	Pressureless Sintering (PS)	Al; Ti	[136]
Al	Al3Ti	Spark Plasma Sintering (SPS)	Al; Ti	[137]
Al	Al3Ti	Spark Plasma Sintering (SPS); Hot Rolling (HR)	Al; Ti	[138]
Al	Al3Ti	Spark Plasma Sintering (SPS)	Al; Ti	[139]
Al	Al3Ti	Hot Extrusion (HE); Hot Isostatic Pressing (HIP)	Al; Ti	[140]
Al	Al3Ti	Hot Pressing (HP); Friction Stir Processing (FSP)	Al; Ti	[141]
AA2024	Al3Ti; Al2O3	Hot Pressing (HP)	Al; TiO2	[1]
Al	Al3Ti; Al2O3	Pressureless Sintering (PS); Hot Extrusion (HE)	Al; Al2TiO5	[142]
Al	Al3Ti; Al3O2	Pressureless Sintering (PS); Hot Extrusion (HE)	Al; Al2TiO5	[143]
AA7075	Al3Ti; B4C	Pressureless Sintering (PS)	AA7075; Ti; B4C	[144]
Al	Al3Zr	Spark Plasma Sintering (SPS); Hot Forging (HF)	Al; ZrH2	[145]
Al	Al3Zr; Al2O3	Hot Pressing (HP); Hot Extrusion (HE); Hot Rolling (HR)	Al; ZrO2	[146]
Al	Al3Zr; Al2O3	Hot Pressing (HP); Hot Extrusion (HE); Hot Rolling (HR)	Al; ZrO2	[147]
Al	Al4C3	Hot Pressing (HP)	Al; Polyvinyl Butyral (PVB)	[72]
Al	Al4C3	Pressureless Sintering (PS); Hot Extrusion (HE)	Al; C	[148]
Al	Al4C3	Pressureless Sintering (PS)	Al; C	[149]
Al	Al4C3	Pressureless Sintering (PS)	Al; C	[150]
Al	Al4C3	Pressureless Sintering (PS)	Al; C	[151]
Al-O	Al4C3	Hot Pressing (HP)	Al; Polyvinyl Buyral (PVB)	[152]
Al	Al4C3	Spark Plasma Sintering (SPS); Hot Extrusion (HE)	Al; CNTs	[153]
Al	Al4C3	Spark Plasma Sintering (SPS); Hot Extrusion (HE)	Al; Multiwalled Carbon Nanotubes (MWCNTs)	[154]
Al	Al5Fe2; Al13Fe4-Fe	Gas-Pressure Sintering (GPS)	Al; Fe	[63]
Al	Al5Fe2; AlN	Gas-Pressure Sintering (GPS)	Al; Fe; N2	[64]
Al	Al9Co2	Pressureless Sintering (PS)	Al; Co	[155]
Al	AlB2	Spark Plasma Sintering (SPS); Hot Rolling (HR)	Al; B	[156]
AA6061	AlN	Pressureless Sintering (PS); Equal Channel Angular Pressing (ECAP)	AA6061; Mg; Sn; Nylon; N2	[157]
Al	AlN	Pressureless Sintering (PS); Hot Extrusion (HE)	AA6061; Mg; Sn; Nylon; N2	[158]
Al	AlN	Pressureless Sintering (PS); Hot Forging (HF)	Al(Si,Ni,Mg); N2	[159]
Al	AlN	Pressureless Sintering (PS); Hot Forging (HF)	Al(Si, Ni, Mg, Fe); N2	[160]
Al	AlN	Pressureless Sintering (PS); Hot Extrusion (HE)	Al; Mg; Sn; N2	[89]
Al	AlN	Hot Pressing (HP)	Al; N2	[161]
Al	AlN	Pressureless Sintering (PS)	Al; NH3	[162]
AA2024	AlN	Pressureless Sintering (PS); Hot Extrusion (HE)	Al; Al-Mg; Cu; N2	[163]

Table A2. *Cont.*

Matrix	Reinforcement	Processing Method	Raw Materials	References
Al	AlN	Pressureless Sintering (PS); Hot Extrusion (HE)	Al; Sn; N2	[164]
Al	AlN; AlB2	Pressureless Sintering (PS)	Al; hBN	[165]
Al	AlN; Si	Pressureless Sintering (PS); Hot Extrusion (HE)	Al(Si, Ni, Mg, Fe); N2	[166]
AA6061	La2Si2O7	Pressureless Sintering (PS)	AA6061; La	[167]
AA6061	Mg(Al)B2	Hot Pressing (HP); Hot Forging (HF); Hot Rolling (HR)	AA6061; B4C	[168]
AA6061	MgAl2O4	Pressureless Sintering (PS); Hot Extrusion (HE)	AA6061; Mg; H3BO3	[169]
AA6061	MgAl2O4	Hot Pressing (HP)	AA6061; Mg; H3BO3	[170]
AA6061	MgAl2O4	Pressureless Sintering (PS); Hot Extrusion (HE)	AA6061; Mg; H3BO3	[171]
Al	MgAl2O4	Pressureless Sintering (PS); Hot Extrusion (HE)	Al; Mg; H3BO3	[172]
Al	MgAl2O4	Pressureless Sintering (PS); Hot Extrusion (HE)	Al; Mg; H3BO3	[173]
Al	MgAl2O4; (Mg,Al)B2	Pressureless Sintering (PS); Hot Extrusion (HE)	Al; Mg; H3BO3	[13]
Al	MgAl2O4; MgZn2	Pressureless Sintering (PS); Hot Extrusion (HE)	Al; Mg; ZnO	[174]
Al	MgAlB4	Pressureless Sintering (PS); Hot Extrusion (HE)	Al; Mg; B	[175]
Al	MoAl12; MoAl5; MoAl4; Al2O3	Pressureless Sintering (PS)	Al; MoO3	[176]
Al	Nano-C; Al2O3; Si	Hot Isostatic Pressing (HIP); Equal Channel Angular Pressing (ECAP)	Al; SiO2; CNTs; GNPs	[177]
Al	Ni-(Al3Ni2; Al3Ni; AlN)	Gas-Pressure Sintering (GPS)	Al; Ni; N2	[178]
AA2014	Ni3Al; NiAl	Hot Extrusion (HE)	AA2014; Ni	[21]
Al	Ni3Al; NiAl; Al3Ni	Hot Pressing (HP)	Al; Ni3Al	[179]
Al	Si; Al2O3; Multiwalled Carbon Nanotubes (MWCNTs)	Hot Pressing (HP)	Al; SiO2; Multiwalled Carbon Nanotubes (MWCNTs)	[180]
Al	SiC; AlN	Spark Plasma Sintering (SPS)	SiCN; Al	[181]
Al	Ti-Al3Ti	Spark Plasma Sintering (SPS)	Al; Ti	[182]
Al	Ti-Al3Ti	Gas-Pressure Sintering (GPS)	Al; Ti	[183]
AA7050	TiB2	Hot Isostatic Pressing (HIP)	AA7050; TiB2	[184]
Al	TiB2	Spark Plasma Sintering (SPS); Hot Extrusion (HE)	Al; Ti; B	[46]
Al	TiB2	Pressureless Sintering (PS)	Al; Ti; B	[53]
Al	TiB2; Al2O3	Pressureless Sintering (PS)	Al; B; TiO2	[51]
Al	TiB2; Al2O3; Al2Cu	Pressureless Sintering (PS); Hot Extrusion (HE)	Al; Cu; TiO2; B2O3	[185]
Al(Cu)	TiB2; TiAl3	Microwave Heating (MH)	Al; Ti; B; Cu	[186]
Al	TiC	Pressureless Sintering (PS); Hot Pressing (HP)	Al; Ti; C	[14]
Al	TiC	Pressureless Sintering (PS)	Al; K2TiF6; C	[187]
Al	TiO; Al2O3	Pressureless Sintering (PS)	Ti2CO; Al	[188]
Al	WAl12	Spark Plasma Sintering (SPS)	Cu; Zr; Al; Ti; Ni; W	[189]
Al	WAl12	Hot Pressing (HP)	Al; W	[190]
Al	WAl12	Hot Pressing (HP)	Al; W	[191]
Al	y-LiAlO2	Pressureless Sintering (PS); Arc Melting (AM)	Al; Li2O	[192]

Table A2. *Cont.*

Matrix	Reinforcement	Processing Method	Raw Materials	References
Al	Y_2O_3; $Al_5Y_3O_{12}$; CaO; $CaAl_4O_7$; $CuAl_2$; $FeAl_3$	Hot Pressing (HP); Hot Extrusion (HE)	Al-Ca; Al-Y; CuO; Fe_2O_3	[193]
Al	α-Al_2O_3; Al_2Cu	Pressureless Sintering (PS)	Al; CuO	[194]
Al	α-Al_2O_3; Si	Pressureless Sintering (PS)	Al; SiO_2	[195]
Al	α-Al_2O_3; ZrB_2	Hot Pressing (HP)	Al; ZrO_2; B	[16]
Al	β-Al_3Mg_2	Hot Extrusion (HE)	Al; Mg	[196]
Al	β-Al_3Mg_2; γ-$Al_{12}Mg_{17}$	Hot Pressing (HP)	Al; Mg	[56]
Al	γ-Al_2O_3	Pressureless Sintering (PS); Hot Extrusion (HE)	Al; H_3BO_3; $C_{18}H_{36}O_2$	[15]

Table A3. Titanium Matrix Composites.

Matrix	Reinforcement	Processing Method	Raw Materials	References
Ti	GNPs; TiB; TiC	Spark Plasma Sintering (SPS)	Ti; Graphene Nanoplatelets (GNPs); TiB_2	[197]
Ti	Ti(C,N); TiC	Spark Plasma Sintering (SPS)	Ti; Graphene Nanoplatelets (GnP); g-C_3N_4	[198]
Ti	Ti_2Co	Spark Plasma Sintering (SPS)	GO; Co; Ti	[199]
Ti(Al,Zr,Mo,V)	Ti_3AlC; TiC	Spark Plasma Sintering (SPS)	Ti(Al,Zr,Mo,V); Ti_3AlC_2	[200]
Ti	Ti_5Si_3	Spark Plasma Sintering (SPS)	Ti; Si	[201]
Ti	Ti_5Si_3	Spark Plasma Sintering (SPS)	Ti; SiO_2	[202]
Ti(Mo)	Ti_5Si_3	Spark Plasma Sintering (SPS); Hot Rolling (HR)	Ti; Mo; Si	[203]
Ti	Ti_5Si_3; Ti_2C	Hot Pressing (HP)	Ti; SiC	[204]
Ti (Fe, Mo, Al); β-Ti	TiB	Electric Field Assisted Sintering (EFAS)	Ti; TiB_2; Mo; Fe; Al	[85]
Ti	TiB	Coupled Multi-Physical Fields Activation Sintering Technology (CMPFAST)	Ti_6Al_4V; TiB_2	[205]
Ti	TiB	Spark Plasma Sintering (SPS)	Ti; TiB_2	[206]
Ti_6Al_4V	TiB	Spark Plasma Sintering (SPS)	Ti_6Al_4V; TiB_2	[207]
Ti	TiB	Spark Plasma Sintering (SPS)	Ti; TiB_2	[208]
Ti	TiB	Pressureless Sintering (PS)	Ti; TiB_2	[209]
Ti	TiB	Pressureless Sintering (PS)	Ti; TiB_2	[210]
Ti_6Al_4V	TiB	Hot Isostatic Pressing (HIP)	Ti_6Al_4V; TiB_2	[211]
Ti	TiB	Pulse Plasma Sintering (PPS)	Ti; B	[212]
Ti	TiB	Spark Plasma Sintering (SPS)	Ti; TiB_2	[213]
Ti	TiB	Spark Plasma Sintering (SPS)	Ti; TiB_2	[214]
Ti	TiB	Spark Plasma Sintering (SPS)	Ti; TiB_2	[215]
Ti; β-Ti	TiB	Spark Plasma Sintering (SPS)	Ti; KBF_4; Al; Fe	[216]
Ti_6Al_4V	TiB	Spark Plasma Sintering (SPS)	Ti_6Al_4V; Ti; TiB_2	[217]

Table A3. *Cont.*

Matrix	Reinforcement	Processing Method	Raw Materials	References
Ti(Al,Mo,V,Cr)	TiB	Pressureless Sintering (PS); Extrusion (E)	Ti-Al-Mo-V-Zr; TiB2	[218]
Ti6Al4V	TiB	Pressureless Sintering (PS); Hot Extrusion (HE)	Ti6Al4V; TiB2	[219]
Ti	TiB	Spark Plasma Sintering (SPS)	Ti; TiB2	[220]
Ti	TiB	Pulse Plasma Sintering (PPS)	Ti; B	[221]
Ti	TiB	Spark Plasma Sintering (SPS)	Ti; TiB2	[222]
Ti6Al4V	TiB	Pressureless Sintering (PS); Hot Extrusion (HE)	Ti6Al4V; TiB2	[223]
Ti6Al4V	TiB	Hot Isostatic Pressing (HIP)	Ti6Al4V; TiB2	[224]
Ti	TiB	Spark Plasma Sintering (SPS)	Ti; TiB2	[225]
Ti	TiB	Pressureless Sintering (PS)	Ti; B	[226]
Ti6Al4V	TiB	Pressureless Sintering (PS); Hot Extrusion (HE)	Ti6Al4V; TiB2	[227]
Ti6Al4V	TiB	Hot Isostatic Pressing (HIP)	Ti6Al4V; TiB2	[228]
Ti6Al4V	TiB	Spark Plasma Sintering (SPS)	Ti6Al4V; Ti; TiB2	[229]
Ti-Al-Mo-Fe	TiB	Pressureless Sintering (PS)	Ti; Al; Mo; Fe; TiB2; LaB6	[230]
Ti	TiB	Pressureless Sintering (PS); Selective Laser Melting (SLM)	Ti; TiB2	[231]
Ti	TiB	Spark Plasma Sintering (SPS)	Ti; KBF4	[232]
Ti6Al4V	TiB	Hot Pressing (HP)	Ti6Al4V; TiB2	[233]
Ti6Al4V	TiB	Hot Pressing (HP)	Ti6Al4V; TiB2	[234]
Ti	TiB	Spark Plasma Sintering (SPS)	Ti; TiB2	[235]
Ti(Fe,Mo)	TiB	Spark Plasma Sintering (SPS)	Ti; Fe-Mo; TiB2	[236]
Ti60	TiB	Hot Pressing (HP)	T60; TiB2	[237]
Ti6Al4V	TiB	Hot Pressing (HP)	Ti6Al4V; TiB2	[238]
Ti	TiB	Hot Pressing (HP)	Ti; TiB2	[239]
Ti6Al4V	TiB	Spark Plasma Sintering (SPS)	Ti6Al4V; TiB2	[240]
Ti6Al4V	TiB	Hot Pressing (HP)	Ti6Al4V; TiB2	[241]
Ti	TiB	Spark Plasma Sintering (SPS)	Ti; TiB2	[242]
Ti	TiB	Spark Plasma Sintering (SPS)	Ti; TiB2	[243]
Ti	TiB	Current-Activated Pressure-Assisted Sintering (CAPAS); Pressureless Sintering (PS)	Ti; TiB2	[31]
Ti	TiB	Current-Activated Pressure-Assisted Sintering (CAPAS); Pressureless Sintering (PS)	Ti; B; TiB2	[244]
Ti(Mo, Fe)	TiB	Hot Pressing (HP)	Ti; Fe65Mo; B; TiB2	[245]
Ti(Fe,Mo)	TiB	Spark Plasma Sintering (SPS)	Ti; Fe65Mo; B; TiB2	[246]
Ti(Fe,Mo)	TiB	Spark Plasma Sintering (SPS)	Ti; TiB2; Fe65Mo	[247]
Ti(Fe,Mo)	TiB	Spark Plasma Sintering (SPS)	Ti; Fe65Mo; B	[248]
Ti	TiB	Hot Pressing (HP)	Ti; TiB2	[249]
β-Ti	TiB	Hot Pressing (HP)	β-Ti(Mo, Nb, Al, Si); TiB2; α-Ti; Fe-Mo; Mo; Nb	[87]

Table A3. *Cont.*

Matrix	Reinforcement	Processing Method	Raw Materials	References
β-Ti	TiB	Hot Pressing (HP)	Ti; Fe-Mo, TiB2	[250]
Ti6Al4V	TiB	Hot Isostatic Pressing (HIP)	Ti6Al4V; B	[251]
Ti	TiB	Hot Pressing (HP)	Ti; TiB2	[252]
Ti(Al,Sn,Zr,Mo)	TiB	Pressureless Sintering (PS); Hot Isostatic Pressing (HIP)	Ti(Al,Sn,Zr,Mo); TiB2	[253]
Ti(N)	TiB	Spark Plasma Sintering (SPS); Hot Extrusion (HE)	Ti; h-BN	[34]
Ti	TiB	Spark Plasma Sintering (SPS)	Ti; TiB2	[254]
Ti6Al4V	TiB	Plasma Activated Sintering (PAS)	Ti6Al4V; TiB2	[255]
Ti	TiB	Pressureless Sintering (PS); Binder Jetting Printing (BJP)	TiH2; TiB2	[256]
Ti(Ta,Ni)	TiB	Pressureless Sintering (PS)	Ti(Ta,N)i; TiB2	[257]
Ti	TiB	Pressureless Sintering (PS)	Ti; BN	[35]
Ti	TiB	Hydrogen-Assisted Blended Elemental Powder Metallurgy (HABEPM)	TiH; TiB2	[258]
Ti(Al,Zr,Mo,V)	TiB	Hot Pressing (HP); Canned Extrusion (CE)	Ti(Al,Zr,Mo,V); TiB2	[259]
Ti	TiB	Pressureless Sintering (PS)	Ti; BN	[36]
Ti6Al4V	TiB	Spark Plasma Sintering (SPS); Pressureless Sintering (PS)	Ti6Al4V; B4C	[260]
β-Ti	TiB	Pressureless Sintering (PS); Hot Forging (HF)	Ti; Fe-62Mo; Al-50V; TiB2	[86]
Ti(Zr)	TiB	Pressureless Sintering (PS); Hot Rolling (HR)	Ti; ZrB2	[261]
T(Al,Mo,V,Cr,Fe)	TiB	Hot Pressing (HP)	T(Al,Mo,V,Cr,Fe); TiB2	[262]
Ti6Al4V	TiB	Pressureless Sintering (PS)	TiH2, TiB2, and master alloy (Al–V)	[263]
Ti	TiB	Pressureless Sintering (PS)	TiH2; Ti; TiB2	[264]
Ti6Al4V	TiB	Spark Plasma Sintering (SPS); Hot Extrusion (HE)	Ti6Al4V; TiB2	[265]
Ti	TiB	Pressureless Sintering (PS)	TiH; TiB2	[266]
Ti	TiB	Electric Field Assisted Sintering (EFAS)	Ti; TiB2; Fe; Mo	[267]
Ti	TiB; FeTi	Spark Plasma Sintering (SPS)	Ti; TiB2; Fe	[268]
Ti	TiB; Si3N4	Pressureless Sintering (PS)	Ti; TiB2; Si3N4	[269]
Ti6Al4V	TiB; Ti5Si3	Spark Plasma Sintering (SPS)	Ti6Al4V; TiB2; Si	[270]
Ti6Al4V	TiB; Ti5Si3	Hot Pressing (HP)	Ti6Al4V; TiB2; Si	[271]
Ti	TiB; TiB2	Plasma Activated Sintering (PAS)	Ti-Al-V-Fe-C; B	[272]
Ti	TiB; TiC	Spark Plasma Sintering (SPS)	Ti; Mo; B4C	[273]
Ti(Al,Mo,V,Cr)	TiB; TiC	Spark Plasma Sintering (SPS)	Ti-Al-Mo-V-Cr; B4C	[71]
Ti4Al2Fe	TiB; TiC	Spark Plasma Sintering (SPS)	Ti; Al; Fe; KBF4; Graphite foils	[274]
Ti	TiB; TiC	Spark Plasma Sintering (SPS)	Ti; TiB2; B4C	[275]
Ti	TiB; TiC	Spark Plasma Sintering (SPS)	Ti; B4C	[45]

Table A3. *Cont.*

Matrix	Reinforcement	Processing Method	Raw Materials	References
Ti6Al4V	TiB; TiC	Spark Plasma Sintering (SPS)	Ti6Al4V; B4C; B	[276]
Ti	TiB; TiC	Spark Plasma Sintering (SPS); Hot Extrusion (HE)	Ti; B4C	[277]
Ti	TiB; TiC	Spark Plasma Sintering (SPS)	Ti; B4C	[278]
Ti6Al4V	TiB; TiC	Spark Plasma Sintering (SPS); Hot Rolling (HR)	Ti6Al4V; B4C	[279]
Ti	TiB; TiC	Spark Plasma Sintering (SPS); Hot Extrusion (HE)	Ti; B4C	[280]
Ti	TiB; TiC	Spark Plasma Sintering (SPS); Hot Extrusion (HE)	Ti; B4C	[281]
Ti	TiB; TiC	Spark Plasma Sintering (SPS); Hot Extrusion (HE)	Ti; B4C	[282]
Ti	TiB; TiC	Spark Plasma Sintering (SPS)	Ti; B4C	[283]
Ti6Al4V	TiB; TiC	Hot Pressing (HP)	Ti; Ti6Al4V; B4C; C	[284]
Ti	TiB; TiC	Pressureless Sintering (PS)	Ti; B4C	[285]
Ti	TiB; TiC	Hot Pressing (HP)	Ti; TiB2; B4C	[286]
Ti	TiB; TiC	Pre-Sintered (PreS); Hot Isostatic Pressing (HIP)	Ti; TiB2; B4C	[287]
Ti(Al,Fe); Ti(Al,Cr)	TiB; TiC	Pressureless Sintering (PS); Hot Isostatic Pressing (HIP)	Ti; Al3Ti; FeB; Cr3C2	[288]
Ti6Al4V	TiB; TiC	Spark Plasma Sintering (SPS)	Ti6Al4V; TiC; B	[289]
Ti	TiB; TiC	Pressureless Sintering (PS); Binder Jetting Printing (BJP)	TiH2; TiB2; TiC	[290]
Ti(Mo)	TiB; TiC	Spark Plasma Sintering (SPS)	TiB2; Ti; TiC; Mo	[291]
Ti6Al4V	TiB; TiC	Spark Plasma Sintering (SPS)	Ti6Al4V; B4C	[292]
Ti	TiB; TiC; Nd2O3	Pressureless Sintering (PS)	NdB6; Ti(O); B4C	[90]
Ti	TiB; TiC; TiAl	Hot Pressing (HP)	Ti; B4C; Al	[293]
Ti	TiB; TiC; TiAl	Hot Pressing (HP)	Ti; B4C; Al	[294]
Ti	TiB; TiFe	Arc Melting (AM); Pressureless Sintering (PS); Hot Isostatic Pressing (HIP)	Ti; FeB	[295]
Ti	TiB; TiN	Pressureless Sintering (PS)	Ti; BN; Urea	[37]
Ti	TiC	Hot Pressing (HP)	Ti; Diamond	[296]
Ti6Al4V	TiC	Spark Plasma Sintering (SPS)	Ti6Al4V; Graphite	[297]
β-Ti(Nb)	TiC	High Pressure Sintering (HPS)	Ti; Nb; Stearic Acid	[298]
Ti	TiC	Pressureless Sintering (PS)	TiH2; CH4	[299]
Ti(Mo)	TiC	Pressureless Sintering (PS); Hot Swaging (HS)	Ti; Mo; MoC	[43]
Ti6Al4V	TiC	Spark Plasma Sintering (SPS)	Ti6Al4V; Carbon Nanotubes (MWCNT)	[300]
Ti	TiC	Hot Pressing (HP); Hot Rolling (HR)	Ti; Carbon Nanotubes (MWCNT)	[301]
Ti	TiC	Spark Plasma Sintering (SPS)	Ti; Graphene	[41]
Ti	TiC	Pressureless Sintering (PS); Hot Extrusion (HE)	TiH2; Carbon Nanotubes (MWCNT)	[302]

Table A3. *Cont.*

Matrix	Reinforcement	Processing Method	Raw Materials	References
β-Ti70Nb30	TiC	Spark Plasma Sintering (SPS)	β-Ti70Nb30; C	[303]
Ti5Sn3C; Ti13Cr5Sn3C	TiC	Spark Plasma Sintering (SPS)	Ti; Cr; Sn; Carbon Black	[304]
Ti(Mo); Ti(V)	TiC	Pressureless Sintering (PS); Hot Rolling (HR)	Ti; Mo2C; VC	[305]
Ti	TiC	Spark Plasma Sintering (SPS); Hot Extrusion (HE)	Ti; Carbon Nanotubes (VGCFs)	[306]
Ti-Fe	TiC	Pressureless Sintering (PS)	Ti; Fe[C, O, SiO2]; Graphite	[307]
Ti(V); Ti(Mo)	TiC	Pressureless Sintering (PS); Hot Rolling (HR)	Ti; Mo2C; VC	[308]
Ti(Fe, Mo, V)	TiC	Pressureless Sintering (PS)	Ti; Fe; Mo; Mo2C; VC	[309]
Ti	TiC	Spark Plasma Sintering (SPS); Hot Extrusion (HE)	Ti; Carbon Black	[310]
Ti6Al4V	TiC	Pressureless Sintering (PS); Extrusion (E)	Ti6Al4V; Ti; C3H8	[311]
Ti	TiC	Pressureless Sintering (PS); Hot Isostatic Pressing (HIP)	Ti; CH4	[312]
Ti(Ta)	TiC	Spark Plasma Sintering (SPS); Hot Rolling (HR)	Ti; Ta; Stearic Acid	[313]
Ti	TiC	Hot Pressing (HP)	Ti; TiC	[314]
Ti6Al4V	TiC	Hot Pressing (HP)	Ti6Al4V; VC	[315]
Ti	TiC; Ti3Si	Pressureless Sintering (PS)	Ti; (SiH(CH3)–CH2-)n (PCS)	[316]
Ti–Al–Sn–Zr	TiC; Ti5Si3	Pressureless Sintering (PS)	Ti(Al,Sn,Zr); Ti; SiC	[317]
Ti(Nb,Al,Mo)	TiC; Ti5Si3	Spark Plasma Sintering (SPS)	Ti; Nb; Al; Mo; Si; SiC	[318]
Ti(Al,Sn,Zr,Nb,Mo,Si)	TiC; Ti5Si3	Pressureless Sintering (PS)	Ti; Ti(Al,Sn,Zr,Nb,Mo,Si); SiC	[319]
Ti; β-Ti	TiC; TiB	Spark Plasma Sintering (SPS)	Ti; B4C	[320]
Ti	TiC; TiB	Spark Plasma Sintering (SPS)	Ti; B4C	[321]
Ti	TiC; TiB	Spark Plasma Sintering (SPS)	Ti; B4C	[322]
Ti6Al4V	TiC; TiB	Hot Pressing (HP)	Ti; B4C; Graphite; TiB2; TiC; Ti6Al4V	[323]
Ti6Al4V	TiC; TiB	Hot Pressing (HP)	Ti6Al4V; TiB2; Graphite	[324]
Ti(Al,Mo,V,Cr)	TiC; TiB	Spark Plasma Sintering (SPS)	Ti-Al-Mo-V-Cr; B4C; Graphite	[44]
Ti	TiC; TiB	Spark Plasma Sintering (SPS)	Ti; B4C	[325]
Ti	TiC; TiB	Pressureless Sintering (PS); Hot Extrusion (HE)	Ti; B4C	[326]
Ti(Al)	TiC; TiB; Ti3Al; TiAl	Hot Pressing (HP)	Ti; Al; B4C; Ti-Al	[327]
Ti	TiC; TiO2	Spark Plasma Sintering (SPS)	Ti; Toluene	[328]
Ti5V	TiN	Spark Plasma Sintering (SPS)	Ti; V; N2	[329]
Ti	TiN	Mechanosynthesis (M); Hot Pressing (HP)	Ti; NH3	[330]
Ti	TiN	Mechanosynthesis (M); Hot Pressing (HP)	Ti; NH3	[331]
Ti	TiN; Ti2Ni; TiCN	Spark Plasma Sintering (SPS)	Ti; Ni; TiCN	[332]

Table A4. Nickel Matrix Composites.

Matrix	Reinforcement	Processing Method	Raw Materials	References
Ni(Cr)	(Cr, Ni)3C2; (Cr, Mo)3C2; (Cr, Mo, Ni)7C3	Pressureless Sintering (PS)	Cr; C; Ni; Mo	[333]
Ni	(Ti, Mo)C	Pressureless Sintering (PS)	Ti; C; Ni; Mo	[12]
Ni	(Ti, Mo)C	Pressureless Sintering (PS)	Ti; Ni; Mo; C	[76]
Ni	(Ti, Mo)C	Gas-Pressure Sintering (GPS)	Ni; Ti; Mo; C	[334]
Ni	(Ti, Mo)C	Pressureless Sintering (PS)	Ni; Ti; Mo; C	[335]
Ni	(Ti,W)C	Hot Isostatic Pressing (HIP)	Ni; Ti; W; C	[336]
Ni	(Ti,W)C	Pressureless Sintering (PS)	Ti; W; Ni; C	[337]
Ni	(Ti,W)C; WC	Pressureless Sintering (PS)	Ti; W; Graphite	[338]
Ni	Al2O3; NiAl2O4	Hot Pressing (HP)	NiO; Al	[339]
Ni	Al2O3; TiC	Hot Pressing (HP)	Ni; Mo; Al; Ti; C; TiC; Al2O3; TiO2	[340]
Ni	Cr3C2	Pressureless Sintering (PS)	Ni; Cr; C; Mo	[341]
Ni	Cr3C2	Hot Isostatic Pressing (HIP)	Ni; Cr; C	[342]
Ni	Cr3C2	Pressureless Sintering (PS)	Ni; Cr; C	[343]
Ni	Cr3C2	Pressureless Sintering (PS); Hot Isostatic Pressing (HIP)	Ni; Cr; C	[344]
Ni	Cr3C2	Pressureless Sintering (PS)	Ni; Cr; C	[345]
Ni	Cr3C2	Pressureless Sintering (PS)	Ni; Cr; C	[346]
Ni	Graphene	Pressureless Sintering (PS)	Sucrose; Ni	[25]
Ni	Graphene	Pressureless Sintering (PS)	Sucrose; Ni	[347]
Ni	Graphene	Hot Pressing (HP)	Ni; PMMA	[348]
Ni	Graphene	Hot Pressing (HP)	Ni; PMMA	[349]
Ni	Mo2NiB2	Pressureless Sintering (PS)	Mo; Ni; N-B	[350]
Ni	NiAl2O4; Al2O3	Hot Pressing (HP)	Ni(NO3)2.6H2O; Al(NO3)3.9H2O; NaOH; Na2CO3	[91]
Ni(Mo)	Ti(C,N)	Gas-Pressure Sintering (GPS)	Ti; TiO2; Ni; Mo; Graphite; N2	[351]
Ni(Mo)	Ti(C,N)	Pressureless Sintering (PS)	Ti; TiO2; Ni; Mo; Graphite; N2	[352]
Ni(Mo)	Ti(C,N)	Pressureless Sintering (PS)	Ti; TiO2; Ni; Mo; Graphite; N2	[353]
Ni	Ti(C,N)	Pressureless Sintering (PS)	Ni; TiO2; TiN; Mo; WC; C	[354]
Ni	Ti(C,N)	Pressureless Sintering (PS)	Ni; TiO2; TiN; Mo; WC; C	[355]
Ni	Ti(C,N)	Pressureless Sintering (PS)	Ni; TiO2; TiN; Mo; WC; C	[356]
Ti-Ni	TiB; La2O3	Hot Pressing (HP)	Ti-Ni; LaB6	[357]
Ni(Si,Ti)	TiC	Pressureless Sintering (PS)	Ti3SiC2; Ni	[80]
Ni	TiC	Pressureless Sintering (PS)	Ti-Ni; Graphite	[38]
Ni(Si,Ti)	TiC	Pressureless Sintering (PS)	Ti3SiC2; Ni	[358]
Ni	TiC	Spark Plasma Sintering (SPS)	Ni; Ti; C	[359]

Table A4. *Cont.*

Matrix	Reinforcement	Processing Method	Raw Materials	References
Ni	TiC	Pressureless Sintering (PS)	Ni; Ti; Graphite	[360]
Ni(Al)	TiC	Hot Pressing (HP)	Ni; Ti2AlC	[361]
Ni	TiC	Pressureless Sintering (PS)	Ni; Ti; Graphite	[362]
Ni	TiC	Spark Plasma Sintering (SPS)	Ni; Ti; C	[363]
Ni	TiC; (NiCu)3Al; CuNi2Ti	Pressureless Sintering (PS)	Ni; Cu; Ti3AlC2	[364]
Ni	TiC; Graphite	Spark Plasma Sintering (SPS)	Ni; Ti; Graphite	[365]
Ni	TiC; γ'-Ni3(Al,Ti)	Hot Pressing (HP)	Ti2AlC; Ni	[366]
Ni	TiC; γ'-Ni3(Al,Ti)	Hot Pressing (HP)	Ti2AlC; Ni	[50]
Ni	TiC; γ'-Ni3(Al,Ti)	Hot Pressing (HP)	Ti3AlC2; Ni(Cr, Si, Fe, B)	[367]
Ni	TiC; γ'-Ni3(Al,Ti)	Hot Pressing (HP)	Ti2AlC; Ni	[368]
Ni(Ti, Al)	TiC; γ'-Ni3(Al,Ti)	Pressureless Sintering (PS)	Ni; Ti2AlC	[369]
Ni(Mo); Ni(Cr)	TiCxNy; TiB2	Hot Pressing (HP)	Ti; BN; B4C; Cr; Mo	[370]
Ni	TiN; TiCN; Ti2Ni	Spark Plasma Sintering (SPS)	Ti; Ni; TiCN	[371]
Ni	TiN; TiO2	Pressureless Sintering (PS)	Ni; Ti; CONDAT	[372]
Ni(W)	WC	Spark Plasma Sintering (SPS)	Ni; W	[373]
Ni	WC	Hot Pressing (HP)	W; Ni; Graphite	[374]

Table A5. Copper Matrix Composites.

Matrix	Reinforcement	Processing Method	Raw Materials	References
Cu	Al2O3	Spark Plasma Sintering (SPS)	Cu(Al); Oxidants	[375]
Cu	Al2O3	Pressureless Sintering (PS); Hot Extrusion (HE)	Cu-Al; O2	[376]
Cu	Al2O3	Spark Plasma Sintering (SPS)	Cu-Al; CuO; Cu	[377]
Cu(Sn)	Al2O3	Pressureless Sintering (PS)	Sn; Cu2O; Cu-Al	[81]
Cu	Al2O3; CeO2; Cu2O	Spark Plasma Sintering (SPS)	CuAl2O3; Ce; La	[378]
Cu	Al2O3; TiC	Spark Plasma Sintering (SPS)	Cu; Ti2AlC; Cu2O	[379]
Cu	Cr2O3	Hot Pressing (HP)	Cu; Cr; Cu2O	[380]
Cu	Cr3C2; Graphene; CeO2	Spark Plasma Sintering (SPS)	Cu; Graphene Oxide; Cr; Ce	[381]
Cu	Cu5Zr; ZrB2	Rapid Solidification Process (RSP); Nd:YAG Pulsed Laser	Cu; Zr; B	[24]
Cu	Gd2O3	Hot Pressing (HP)	Cu(Gd); CuO2; O2	[48]
Cu	Graphene	Hot Pressing (HP)	Cu; Paraffin	[382]
Cu	Graphene	Spark Plasma Sintering (SPS)	Cu; Wheat flour	[383]
Cu	Graphene; Al2O3	Hot Pressing (HP)	Cu; C9H21AlO3	[384]
Cu(Ti)	Graphene; TiC	Pressureless Sintering (PS)	Cu; Graphene; Ti	[385]
Cu	Mo2C	Hot Pressing (HP)	Cu; Mo; C	[386]
Cu	Mo2C	Pressureless Sintering (PS); Spark Plasma Sintering (SPS)	Cu; Mo; C	[387]

Table A5. *Cont.*

Matrix	Reinforcement	Processing Method	Raw Materials	References
Cu	NbC	Pressureless Sintering (PS); Hot Extrusion (HE)	Cu-Nb; Nb; Stearic Acid	[388]
Cu	NbC	Pressureless Sintering (PS)	Cu; Nb; Graphite	[389]
Cu	NbC	Pressureless Sintering (PS)	Cu; Nb; Graphite	[390]
Cu	NbC	Spark Plasma Sintering (SPS)	Cu; Nb; Graphite	[49]
Cu	NbC	Pressureless Sintering (PS)	Cu; Nb; Graphite	[391]
Cu	NbC	Spark Plasma Sintering (SPS)	Cu; Nb; Graphite	[392]
Cu	NbC	Pressureless Sintering (PS)	Cu; Nb; Graphite	[393]
Cu	NbC	Pressureless Sintering (PS)	Cu; Nb; Graphite	[394]
Cu	NbC	Hot Pressing (HP)	Cu; Nb; Graphite	[395]
Cu	TiB2	Hot Pressing (HP)	Cu; Ti; B	[396]
Cu	TiB2	Hot Pressing (HP); Hot Extrusion (HE)	Cu; Ti; B	[397]
Cu	TiB2; TiB	Hot Pressing (HP)	Cu; Ti; TiH2; B	[398]
Cu	TiB2; TiB	Pressureless Sintering (PS)	Cu; Ti; B	[399]
Cu	TiB2; TiC	Laser Sintering (LS)	Cu; B4C; Ni; Ti	[400]
Cu	TiC	Spark Plasma Sintering (SPS)	Ti25Cu75; C	[401]
Cu	TiC	Spark Plasma Sintering (SPS)	Ti25Cu75; Carbon black; Nanodiamonds	[402]
Cu	TiC	Hot Pressing (HP)	Cu; Ti; Graphite	[403]
Cu	TiC	Spark Plasma Sintering (SPS)	Cu; Ti; Graphite	[404]
Cu	TiC	Spark Plasma Sintering (SPS)	Cu; Ti; TiH2; Graphite	[405]
Cu	TiC	Pressureless Sintering (PS)	Cu; Ti; Graphite	[406]
Cu	TiC	Spark Plasma Sintering (SPS)	Cu; Ti; Graphite	[407]
Cu(Ti)	TiC	Spark Plasma Sintering (SPS); Hot Rolling (HR)	Cu; Ti; Graphite	[39]
Cu	TiC	Spark Plasma Sintering (SPS); Hot Pressing (HP)	Cu; Ti; Carbon Black	[408]
Cu	TiC	Spark Plasma Sintering (SPS)	Cu; TiH2; C; TiC	[409]
Cu	TiC	Spark Plasma Sintering (SPS)	Cu; Ti; C; Graphite; Nanodiamonds	[410]
Cu	TiC; C	Pressureless Sintering (PS)	Cu; Ti; Graphite; Carbon nanotube (CNT); Graphene	[411]
Cu	TiC; CuTi4	Hot Extrusion (HE)	CuTi; Graphite	[412]
Cu	TiC; Graphene	Pressureless Sintering (PS)	Cu; Ti; Graphite	[413]
Cu(Sn)	V2C	Hot Pressing (HP)	Cu; V2SnC	[414]
Cu	WC	Hot Pressing (HP)	Cu, W; Graphite	[68]
Cu(W)	WC	Hot Pressing (HP)	Cu; W; GCI	[415]
Cu	WC; W2C	Pressureless Sintering (PS)	Cu; W; Graphite	[70]
Cu	Y2Ti2O7	Spark Plasma Sintering (SPS)	Cu(Y); TiO2	[416]

Table A6. Iron and Steel Matrix Composites.

Matrix	Reinforcement	Processing Method	Raw Materials	References
Fe	(Ti,V)C	Pressureless Sintering (PS)	Ti; Fe; FeV; C	[417]
Fe	(Ti,V)C	Pressureless Sintering (PS)	Fe; FeV; FeCr; FeMo; Ti; C	[418]
Fe	(Ti,V)C	Pressureless Sintering (PS)	Fe; FeV; FeCr; FeMo; Ti; C	[419]
Fe	(Ti,V)C	Pressureless Sintering (PS)	Ti; Fe; Fe–V; Fe–Cr; Fe–Mo; C	[420]
Fe(Al)	Al2O3; Fe3Al	Hot Pressing (HP)	Fe-Al	[421]
Fe	Al2O3; FeAl2O4	Pressureless Sintering (PS)	Fe-Al2O3	[422]
316L Steel	Cr7C3; Cr3C2; Fe2Si	Spark Plasma Sintering (SPS)	316L; PCS	[423]
316L Steel	Cr7C3; FeSi	Spark Plasma Sintering (SPS)	316L; PCS	[33]
HCWI	Cr7C3; TiC	Pressureless Sintering (PS); Hot Pressing (HP)	HCWI; TiC; Ti3AlC2	[424]
Fe	Fe3O4	Pressureless Sintering (PS)	Fe; O2	[425]
Fe	Fe3O4	Pressureless Sintering (PS)	Fe; H2O	[426]
Fe	Fe3O4	Pressureless Sintering (PS)	Fe; Fe2O3	[427]
Fe	FeAl2O4	Hot Pressing (HP)	Fe; Fe2O3; Al2O3	[428]
Fe	FeAl2O4	Pressureless Sintering (PS)	Fe; Al2O3	[429]
Fe	FeAl2O4; Al2O3	Pressureless Sintering (PS)	Fe; Al2O3	[430]
Fe	FeB; Fe2B	Hot Pressing (HP); Pressureless Sintering (PS)	Fe; B4C	[82]
Fe(Mo)	FeS; TiC; VC	Pressureless Sintering (PS)	Fe2O3; FeO; TiO2; V2O5; Al2O3; SiO2; MgO; Fe; Graphite; MoS2	[431]
Fe(Cr,C)	M7C3; TiC	Pressureless Sintering (PS); Hot Pressing (HP)	HCWI; Ti3AlC2	[432]
Fe-Si	MnO-SiO2	Spark Plasma Sintering (SPS)	Fe-Si; MnO2	[433]
Fe	Mo(Ti)2FeB	Pressureless Sintering (PS)	Mo; FeB; Fe; Ti	[434]
Fe-Ni	Nanodiamonds	Spark Plasma Sintering (SPS)	Fe30Ni; MWCNTs	[435]
Fe	NbC	Pressureless Sintering (PS)	Fe; Nb; Graphite	[436]
Fe	TiB2	Spark Plasma Sintering (SPS)	FeTi; FeB	[437]
Fe-Cr-Mn-Al	TiB2	Spark Plasma Sintering (SPS)	Cr; Fe; Mn; Al; Ti; B	[438]
Fe	TiB2	Spark Plasma Sintering (SPS); Pressureless Sintering (PS)	FeB; TiH2	[75]
Steel	TiB2; TiC	Spark Plasma Sintering (SPS)	Fe2Ti; B4C	[55]
Steel	TiB2; TiC	Spark Plasma Sintering (SPS)	FeTi; B4C	[17]
Steel	TiB2; TiC	Pressureless Sintering (PS)	465 stainless steel; FeB; Ti; C	[20]
Fe/Steel	TiB2; TiC	Pressureless Sintering (PS)	465 stainless steel; FeB; Ti; C	[439]
Fe	TiB2; TiC	Pressureless Sintering (PS)	Ti; C; FeB	[440]
Steel	TiC	Pressureless Sintering (PS); Hot Isostatic Press (HIP)	Fe; TiH2; C	[19]

Table A6. *Cont.*

Matrix	Reinforcement	Processing Method	Raw Materials	References
Fe	TiC	Pressureless Sintering (PS)	Fe2O3; TiO2; Graphite	[52]
Fe	TiC	Pressureless Sintering (PS)	Fe; Ti; C	[441]
Fe	TiC	Pressureless Sintering (PS)	Fe3O4; FeTiO3; Al2O3; SiO2; MgO; CaO; Fe; La2O3; CeO2; Graphite	[442]
Fe(Ni, Mo, Cu)	TiC	Pressureless Sintering (PS)	Fe; Ti; Mo; Ni; Cu; Graphite	[443]
Fe	TiC	Pressureless Sintering (PS)	FeTi70; Sucrose	[74]
Fe	TiC	Hot Isostatic Pressing (HIP); Hot Pressing (HP)	Graphite; Steel; FeTi; WCI	[444]
Fe	TiC	Pressureless Sintering (PS)	FeTiO3; Graphite	[445]
Steel	TiC; TiB2	Pressureless Sintering (PS)	465 stainless steel; FeB; Ti; C	[446]
Fe	TiN	Spark Plasma Sintering (SPS); Pressureless Sintering (PS)	Fe(Cr,Ni,Ti); N2	[447]
Steel	TiN; TiB2	Spark Plasma Sintering (SPS)	FeTi; BN	[448]
Steel	TiN; VN	Hot Isostatic Pressing (HIP)	X4CrMoV15–1; FeTi; X4CrMo15–1; FeV; Graphite; N2	[449]
Fe(Cr, V)	V3B4; V8C7	Pressureless Sintering (PS)	FeV; C; Fe45	[450]
Fe(Cr,Mo)	VC	Pressureless Sintering (PS)	Fe; FeV; FeCr; FeMo; C	[32]
Fe	VC	Spark Plasma Sintering (SPS)	FeV; C	[45]
Fe	WC; Fe3W3C; W2C	Spark Plasma Sintering (SPS)	Fe; Cu; W; C	[451]
Fe	WC; W2C; Fe3W3C	Spark Plasma Sintering (SPS)	Fe; C; W; Cu; WC	[452]
Fe	ZrO2; Zr6Fe3O	Pressureless Sintering (PS)	Fe; ZrO2	[453]

References

1. Chao, Z.; Zhang, L.; Jiang, L.; Qiao, J.; Xu, Z.; Chi, H.; Wu, G. Design, microstructure and high temperature properties of in-situ Al_3Ti and nano-Al_2O_3 reinforced 2024Al matrix composites from Al-TiO_2 system. *J. Alloy. Compd.* **2019**, *775*, 290–297. [CrossRef]
2. Tanprayoon, D.; Srisawadi, S.; Sato, Y.; Tsukamoto, M.; Suga, T. Microstructure and hardness response of novel 316L stainless steel composite with TiN addition fabricated by SLM. *Opt. Laser Technol.* **2020**, *129*, 106238. [CrossRef]
3. Behera, M.P.; Dougherty, T.; Singamneni, S. Conventional and Additive Manufacturing with Metal Matrix Composites: A Perspective. *Procedia Manuf.* **2019**, *30*, 159–166. [CrossRef]
4. Lloyd, D.; Lagace, H.; McLeod, A.; Morris, P. Microstructural aspects of aluminium-silicon carbide particulate composites produced by a casting method. *Mater. Sci. Eng. A* **1989**, *107*, 73–80. [CrossRef]
5. Pandey, U.; Purohit, R.; Agarwal, P.; Dhakad, S.; Rana, R. Effect of TiC particles on the mechanical properties of aluminium alloy metal matrix composites (MMCs). *Mater. Today Proc.* **2017**, *4*, 5452–5460. [CrossRef]
6. Maurya, M.; Kumar, S.; Bajpai, V.; Maurya, N.K. Process parameters, development and applications of stir cast composite: A review. *Mater. Test.* **2020**, *62*, 196–208. [CrossRef]
7. Lawley, A.; Apelian, D. Spray Forming of Metal Matrix Composites. *Powder Met.* **1994**, *37*, 123–128. [CrossRef]
8. Bains, P.S.; Sidhu, S.; Payal, H.S. Fabrication and Machining of Metal Matrix Composites: A Review. *Mater. Manuf. Process.* **2015**, *31*, 553–573. [CrossRef]
9. Rahimipour, M.R.; Sobhani, M. Evaluation of Centrifugal Casting Process Parameters for In Situ Fabricated Functionally Gradient Fe-TiC Composite. *Met. Mater. Trans. Mater. Process. Sci.* **2013**, *44*, 1120–1123. [CrossRef]
10. Shin, D.-S.; Lee, J.-C.; Yoon, E.-P.; Lee, H.-I. Effect of the processing methods on the formation of Al_4C_3 in SiCp/2024 Al composites. *Mater. Res. Bull.* **1997**, *32*, 1155–1163. [CrossRef]

11. Veeravalli, R.R.; Nallu, R.; Sarcar, M.M.M. Mechanical and tribological properties of AA7075–TiC metal matrix composites under heat treated (T6) and cast conditions. *J. Mater. Res. Technol.* **2016**, *5*, 377–383. [CrossRef]
12. Jõeleht, M. The Influence of Sintering Temperature of Reactive Sintered (Ti, Mo)C-Ni Cermets. *Mater. Sci.* **2015**, *21*, 435–438. [CrossRef]
13. Wang, F.; Li, J.; Shi, C.; Zhao, N.; Liu, E.; He, C.; He, F. Preparation and mechanical properties of in-situ synthesized nano-$MgAl_2O_4$ particles and $Mg_xAl_{(1-x)}B_2$ whiskers co-reinforced Al matrix composites. *Mater. Sci. Eng. A* **2018**, *735*, 236–242. [CrossRef]
14. Duygulu, O. High-resolution transmission electron microscopy investigation of in situ TiC/Al composites. *Met. Mater.* **2018**, *56*, 265–275. [CrossRef] [PubMed]
15. Qu, X.; Wang, F.; Shi, C.; Zhao, N.; Liu, E.; He, C.; He, F. In situ synthesis of a gamma-Al_2O_3 whisker reinforced aluminium matrix composite by cold pressing and sintering. *Mater. Sci. Eng. A* **2018**, *709*, 223–231. [CrossRef]
16. Mokhnache, E.O.; Wang, G.-S.; Geng, L.; Balasubramaniam, K.; Henniche, A.; Ramdani, N. In situ (α-Al_2O_3 + ZrB_2)/Al composites with network distribution fabricated by reaction hot pressing. *Int. J. Miner. Met. Mater.* **2016**, *22*, 1092–1100. [CrossRef]
17. Li, B.; Liu, Y.; Li, J.; Cao, H.; He, L. Effect of sintering process on the microstructures and properties of in situ TiB_2–TiC reinforced steel matrix composites produced by spark plasma sintering. *J. Mater. Process. Technol.* **2010**, *210*, 91–95. [CrossRef]
18. Verezub, O.; Kálazi, Z.; Buza, G.; Verezub, N.V.; Kaptay, G. Classification of laser beam induced surface engineering technologies andin situsynthesis of steel matrix surface nanocomposites. *Surf. Eng.* **2011**, *27*, 428–435. [CrossRef]
19. Lee, J.; Lee, D.; Song, M.H.; Rhee, W.; Ryu, H.J.; Hong, S.H. In-situ synthesis of TiC/Fe alloy composites with high strength and hardness by reactive sintering. *J. Mater. Sci. Technol.* **2018**, *34*, 1397–1404. [CrossRef]
20. Akhtar, F. Microstructure evolution and wear properties of in situ synthesized TiB_2 and TiC reinforced steel matrix composites. *J. Alloy. Compd.* **2008**, *459*, 491–497. [CrossRef]
21. da Costa, C.; Zapata, W.; Velasco, F.; Ruiz-Prieto, J.; Torralba, J. Wear behaviour of aluminum reinforced with nickel aluminide MMCs. *J. Mater. Process. Technol.* **1999**, *92–93*, 66–70. [CrossRef]
22. Rezaei, A.; Hosseini, H.R.M. Investigating the effect of heat treatment on the fracture toughness of a hot extruded Al–Ti composite produced by powder metallurgy route. *Mater. Sci. Eng. A* **2020**, *771*, 138573. [CrossRef]
23. Fogagnolo, J.; Pallone, E.; Martin, D.; Kiminami, C.; Bolfarini, C.; Botta, W. Processing of Al matrix composites reinforced with Al–Ni compounds and Al_2O_3 by reactive milling and reactive sintering. *J. Alloy. Compd.* **2009**, *471*, 448–452. [CrossRef]
24. Stašić, J.; Rajković, V.; Ružić, J.; Božić, D. An investigation on synthesis development of high hardened, high conductivity Cu-Zr and Cu-Zr-ZrB_2 alloys through green compact laser sintering. *Int. J. Adv. Manuf. Technol.* **2015**, *80*, 1049–1057. [CrossRef]
25. Jiang, J.; He, X.; Du, J.; Pang, X.; Yang, H.; Wei, Z. In-situ fabrication of graphene-nickel matrix composites. *Mater. Lett.* **2018**, *220*, 178–181. [CrossRef]
26. Tjong, S.C. Microstructural and mechanical characteristics of in situ metal matrix composites. *Mater. Sci. Eng. R Rep.* **2000**, *29*, 49–113. [CrossRef]
27. Amosov, A.P. Nanomaterials of SHS technology for tribological applications: A review. *Russ. J. Non-Ferrous Met.* **2017**, *58*, 530–539. [CrossRef]
28. Subrahmanyam, J.; Vijayakumar, M. Self-propagating high-temperature synthesis. *J. Mater. Sci.* **1992**, *27*, 6249–6273. [CrossRef]
29. Karanjai, M.; Sundaresan, R.; Rao, G.V.N.; Mohan, T.R.R.; Kashyap, B.P. Development of titanium based biocomposite by powder metallurgy processing with in situ forming of Ca–P phases. *Mater. Sci. Eng. A* **2007**, *447*, 19–26. [CrossRef]
30. Karanjai, M.; Kumar, B.M.; Sundaresan, R.; Basu, B.; Mohan, T.R.; Kashyap, B. Fretting wear study on Ti–Ca–P biocomposite in dry and simulated body fluid. *Mater. Sci. Eng. A* **2008**, *475*, 299–307. [CrossRef]
31. Patel, V.; El-Desouky, A.; Garay, J.; Morsi, K. Pressure-less and current-activated pressure-assisted sintering of titanium dual matrix composites: Effect of reinforcement particle size. *Mater. Sci. Eng. A* **2009**, *507*, 161–166. [CrossRef]
32. Wang, J.; Fu, S. Production of in situ Vanadium Carbide Particulate Reinforced Iron Matrix Composite. *Mater. Sci.* **2014**, *20*, 409–413. [CrossRef]
33. Guan, D.; He, X.; Zhang, R.; Li, R.; Qu, X. Tribological and corrosion properties of PM 316L matrix composites reinforced by in situ polymer-derived ceramics. *Vacuum* **2018**, *148*, 319–326. [CrossRef]
34. Pan, D.; Li, S.; Gao, L.; Liu, L.; Zhang, X.; Ji, X.; Umeda, J.; Kondoh, K. TiB Whisker and Nitrogen Solid-Solution Synergistic-Strengthened Titanium Matrix Composites by Ti–BN via Spark Plasma Sintering and Hot Extrusion. *Adv. Eng. Mater.* **2021**, *23*, 2100344. [CrossRef]
35. Otte, J.A.; Zou, J.; Patel, R.; Lu, M.; Dargusch, M.S. TiB Nanowhisker Reinforced Titanium Matrix Composite with Improved Hardness for Biomedical Applications. *Nanomaterials* **2020**, *10*, 2480. [CrossRef] [PubMed]
36. Otte, J.A.; Zou, J.; Huang, Y.; Dargusch, M.S. Ultrahigh Aspect Ratio TiB Nanowhisker-Reinforced Titanium Matrix Composites as Lightweight and Low-Cost Replacements for Superalloys. *ACS Appl. Nano Mater.* **2020**, *3*, 8208–8215. [CrossRef]
37. Toptan, F. Corrosion and wear behaviour of highly porous Ti-TiB-TiNxin situ composites in simulated physiological solution. *Turk. J. Chem.* **2020**, *44*, 805–816. [CrossRef] [PubMed]
38. Kwon, H.; Jung, S.-A.; Suh, C.-Y.; Roh, K.-M.; Kim, W.; Kim, J. Highly toughened dense TiC–Ni composite by in situ decomposition of (Ti,Ni)C solid solution. *Ceram. Int.* **2015**, *41*, 4656–4661. [CrossRef]
39. Wang, F.; Li, Y.; Yamanaka, K.; Wakon, K.; Harata, K.; Chiba, A. Influence of two-step ball-milling condition on electrical and mechanical properties of TiC-dispersion-strengthened Cu alloys. *Mater. Des.* **2014**, *64*, 441–449. [CrossRef]

40. Rezaei, A.; Hosseini, H.R.M. Evolution of microstructure and mechanical properties of Al-5 wt.% Ti composite fabricated by P/M and hot extrusion: Effect of heat treatment. *Mater. Sci. Eng. A* **2017**, *689*, 166–175. [CrossRef]
41. Zhang, X.; Song, F.; Wei, Z.; Yang, W.; Dai, Z. Microstructural and mechanical characterization of in-situ TiC/Ti titanium matrix composites fabricated by graphene/Ti sintering reaction. *Mater. Sci. Eng. A* **2017**, *705*, 153–159. [CrossRef]
42. Krizik, P.; Balog, M.; Nagy, S. Small punch testing of heat resistant ultrafine-grained Al composites stabilized by nano-metric Al2O3 (HITEMAL©) in a broad temperature range. *J. Alloy. Compd.* **2021**, *887*, 161332. [CrossRef]
43. Xu, S.; Zhou, C.; Liu, Y.; Liu, B.; Li, K. Microstructure and mechanical properties of Ti-15Mo-xTiC composites fabricated by in-situ reactive sintering and hot swaging. *J. Alloy. Compd.* **2018**, *738*, 188–196. [CrossRef]
44. Grützner, S.; Krüger, L.; Radajewski, M.; Schneider, I. Characterization of In-Situ TiB/TiC Particle-Reinforced Ti-5Al-5Mo-5V-3Cr Matrix Composites Synthesized by Solid-State Reaction with B4C and Graphite through SPS. *Metals* **2018**, *8*, 377. [CrossRef]
45. Huang, L.; Qian, M.; Liu, Z.; Nguyen, V.T.; Yang, L.; Wang, L.; Zou, J. In situ preparation of TiB nanowires for high-performance Ti metal matrix nanocomposites. *J. Alloy. Compd.* **2018**, *735*, 2640–2645. [CrossRef]
46. Sadeghian, Z.; Lotfi, B.; Enayati, M.; Beiss, P. Microstructural and mechanical evaluation of Al–TiB2 nanostructured composite fabricated by mechanical alloying. *J. Alloy. Compd.* **2011**, *509*, 7758–7763. [CrossRef]
47. He, L.; Liu, Y.; Li, B.; Cao, H.; Li, J. Reaction synthesis of in situ vanadium carbide particulates-reinforced iron matrix composites by spark plasma sintering. *J. Mater. Sci.* **2010**, *45*, 2538–2542. [CrossRef]
48. Cao, H.; Zhan, Z.; Lv, X. Microstructure Evolution and Properties of an In-Situ Nano-Gd_2O_3/Cu Composite by Powder Metallurgy. *Materials* **2021**, *14*, 5021. [CrossRef]
49. Long, B.; Othman, R.; Umemoto, M.; Zuhailawati, H. Spark plasma sintering of mechanically alloyed in situ copper–niobium carbide composite. *J. Alloy. Compd.* **2010**, *505*, 510–515. [CrossRef]
50. Hu, W.; Huang, Z.; Cai, L.; Lei, C.; Zhai, H.; Zhou, Y. Exploring the interfacial state and tensile behaviors in nickel matrix composite with in-situ TiC and γ'-Ni3(Al,Ti) reinforcements. *J. Alloy. Compd.* **2018**, *765*, 987–993. [CrossRef]
51. Chen, Z.-C.; Takeda, T.; Ikeda, K. Microstructural evolution of reactive-sintered aluminum matrix composites. *Compos. Sci. Technol.* **2008**, *68*, 2245–2253. [CrossRef]
52. Ghiasabadi, S.M.; Raygan, S. In Situ Production of Fe-TiC Nanocomposite by Mechanical Activation and Heat Treatment of the $Fe_2O_3/TiO_2/C$ Powder. *J. Mater. Eng. Perform.* **2012**, *21*, 2295–2302. [CrossRef]
53. Brinkman, H.; Duszczyk, J.; Katgerman, L. In-situ formation of TiB 2 in a P/M aluminum matrix. *Scr. Mater.* **1997**, *37*, 293–297. [CrossRef]
54. Andrieux, J.; Dezellus, O.; Bosselet, F.; Viala, J.C. Low-Temperature Interface Reaction Between Titanium and the Eutectic Silver-Copper Brazing Alloy. *J. Phase Equilibria Diffus.* **2009**, *30*, 40–45. [CrossRef]
55. Li, B.H.; Liu, Y.; Li, J.; Cao, H.; He, L. Fabrication of *in situ* TiB_2–TiC reinforced steel matrix composites by spark plasma sintering. *Powder Met.* **2011**, *54*, 222–224. [CrossRef]
56. Shahid, R.N.; Scudino, S. Microstructure and Mechanical Behavior of Al-Mg Composites Synthesized by Reactive Sintering. *Metals* **2018**, *8*, 762. [CrossRef]
57. Ediger, M. Dynamics of Polymer Glasses and Melts: Probe Diffusion. In *Encyclopedia of Materials: Science and Technology*; Elsevier: Amsterdam, The Netherlands, 2004. [CrossRef]
58. Shi, H.; Zhao, Y.; Gao, H.-B.; Zhang, M.-S.; Jiang, Y.-H.; Cao, F.; Zou, J.-T.; Liang, S.-H. In-situ spherical TiB_2/Cu composite powder: A new method of liquid phase reaction coupled with gas atomization. *Mater. Charact.* **2022**, *191*, 112096. [CrossRef]
59. German, R.M. *Powder Metallurgy & Particulate Materials Processing*; Metal Powder Industry: Princeton, NJ, USA, 2005.
60. Woo, K.D.; Lee, H.B. Fabrication of Al alloy matrix composite reinforced with subsive-sized Al_2O_3 particles by the in situ displacement reaction using high-energy ball-milled powder. *Mater. Sci. Eng. A* **2007**, *449–451*, 829–832. [CrossRef]
61. Aguilar, C.; Martin, P.; Pio, E.; Salvo, C.; Neves, G. Materials analysis applying thermodynamic (MAAT) software: A friendly and free tool to analyze the formation of solid solutions, amorphous phases and intermetallic compounds. *Comput. Phys. Commun.* **2021**, *259*, 107573. [CrossRef]
62. Gu, J.; Gu, S.; Xue, L.; Wu, S.; Yan, Y. Microstructure and mechanical properties of in-situ Al13Fe4/Al composites prepared by mechanical alloying and spark plasma sintering. *Mater. Sci. Eng. A* **2012**, *558*, 684–691. [CrossRef]
63. Xue, Y.; Shen, R.; Ni, S.; Xiao, D.; Song, M. Effects of Sintering Atmosphere on the Mechanical Properties of Al-Fe Particle-Reinforced Al-Based Composites. *J. Mater. Eng. Perform.* **2015**, *24*, 1890–1896. [CrossRef]
64. Xue, Y.; Shen, R.; Ni, S.; Song, M.; Xiao, D. Fabrication, microstructure and mechanical properties of Al–Fe intermetallic particle reinforced Al-based composites. *J. Alloy. Compd.* **2015**, *618*, 537–544. [CrossRef]
65. Miedema, A.; de Châtel, P.; de Boer, F. Cohesion in alloys—Fundamentals of a semi-empirical model. *Phys. B+C* **1980**, *100*, 1–28. [CrossRef]
66. Zhang, R.; Zhang, S.; He, Z.; Jing, J.; Sheng, S. Miedema Calculator: A thermodynamic platform for predicting formation enthalpies of alloys within framework of Miedema's Theory. *Comput. Phys. Commun.* **2016**, *209*, 58–69. [CrossRef]
67. Aguilar, C.; Martinez, C.; Tello, K.; Palma, S.; Delonca, A.; Martín, F.S.; Alfonso, I. Thermodynamic Analysis of the Formation of FCC and BCC Solid Solutions of Ti-Based Ternary Alloys by Mechanical Alloying. *Metals* **2020**, *10*, 510. [CrossRef]
68. Li, J.; Ni, J.; Huang, B.; Chen, J.; Xu, Z.; Liao, S.; Wang, C.; Luo, W. Long-term ball milling and hot pressing of in-situ nanoscale tungsten carbides reinforced copper composite and its characterization. *Mater. Charact.* **2019**, *152*, 134–140. [CrossRef]
69. Chookajorn, T.; Murdoch, H.A.; Schuh, C.A. Design of Stable Nanocrystalline Alloys. *Science* **2012**, *337*, 951–954. [CrossRef]

70. Yusoff, M.; Zuhailawati, H. In Situ Tungsten Carbide Formation in Nanostructured Copper Matrix Composite Using Mechanical Alloying and Sintering. *Materials* **2022**, *15*, 2340. [CrossRef]
71. Grützner, S.; Krüger, L.; Schimpf, C.; Radajewski, M.; Schneider, I. Microstructure and Mechanical Properties of In Situ TiB/TiC Particle-Reinforced Ti-5Al-5Mo-5V-3Cr Composites Synthesized by Spark Plasma Sintering. *Met. Mater. Trans. A* **2018**, *49*, 5671–5682. [CrossRef]
72. Hu, J.; Zhang, J.; Luo, G.; Sun, Y.; Shen, Q.; Zhang, L. Design and Synthesis of C-O Grain Boundary Strengthening of Al Composites. *Nanomaterials* **2020**, *10*, 438. [CrossRef]
73. Karak, S.; Chudoba, T.; Witczak, Z.; Lojkowski, W.; Manna, I. Development of ultra high strength nano-Y_2O_3 dispersed ferritic steel by mechanical alloying and hot isostatic pressing. *Mater. Sci. Eng. A* **2011**, *528*, 7475–7483. [CrossRef]
74. Wang, J.-J.; Hao, J.-J.; Guo, Z.-M.; Wang, S. Plasma preparation and low-temperature sintering of spherical TiC–Fe composite powder. *Int. J. Miner. Met. Mater.* **2015**, *22*, 1328–1333. [CrossRef]
75. Cho, H.-R.; Kim, J.-S.; Chung, K.-H. Microstructure, mechanical, and tribological properties of pressureless sintered and spark plasma sintered Fe TiB2 nanocomposites. *Tribol. Int.* **2019**, *131*, 83–93. [CrossRef]
76. Viljus, M.; Pirso, J.; Juhani, K.; Letunovitš, S. Structure Formation in Ti-C-Ni-Mo Composites during Reactive Sintering. *Mater. Sci.* **2012**, *18*, 62–65. [CrossRef]
77. Porter, D.A. *Phase Transformations in Metals and Alloys*; Springer: Berlin/Heidelberg, Germany, 1992.
78. Lifshitz, I.; Slyozov, V. The kinetics of precipitation from supersaturated solid solutions. *J. Phys. Chem. Solids* **1961**, *19*, 35–50. [CrossRef]
79. Wagner, C. Theorie der Alterung von Niederschliigen durch Umlosen (Ostwald-Reifung). *Z. Elektrochem. Ber. Bunsenges. Phys. Chem.* **1961**, *65*, 581–591.
80. Chiker, N.; Benamor, A.; Hadji, Y.; Haddad, A.; Hakem, M.; Azzaz, M.; Sahraoui, T.; Hadji, M. Microstructure and Tribological Behavior of In Situ TiC-Ni(Si,Ti) Composites Elaborated from Ni and Ti_3SiC_2 Powders. *J. Mater. Eng. Perform.* **2020**, *29*, 1995–2005. [CrossRef]
81. Chen, F.; Yan, Z.; Wu, X.; Liu, B.; Liu, Y. Microstructures and properties of Cu-10Sn oil bearings reinforced by Al_2O_3 nanoparticles. *Adv. Powder Technol.* **2021**, *32*, 710–717. [CrossRef]
82. Nair, F.; Hamamcı, M. Effect of In-Situ Synthesized Boride Phases on the Impact Behavior of Iron-Based Composites Reinforced by B4C Particles. *Metals* **2020**, *10*, 554. [CrossRef]
83. Tokita, M. The Potential of Spark Plasma Sintering (SPS) Method for the Fabrication on an Industrial Scale of Functionally Graded Materials. *Adv. Sci. Technol.* **2010**, *63*, 322–331. [CrossRef]
84. Cavaliere, P. Spark plasma sintering of materials: Advances in processing and applications. In *Spark Plasma Sintering of Materials*; Advances in Processing and Applications; Springer: Berlin/Heidelberg, Germany, 2019. [CrossRef]
85. Degnah, A.; Du, J.; Chandran, K.R. CALPHAD Approach and processing of a multicomponent titanium matrix composite for high strength and fracture toughness. *Mater. Sci. Eng. A* **2020**, *781*, 139210. [CrossRef]
86. Saito, T.; Takamiya, H.; Furuta, T. Thermomechanical properties of P/M β titanium metal matrix composite. *Mater. Sci. Eng. A* **1998**, *243*, 273–278. [CrossRef]
87. Panda, K.B.; Chandran, K.S.R. Synthesis of ductile titanium-titanium boride (Ti-TiB) composites with a beta-titanium matrix: The nature of TiB formation and composite properties. *Met. Mater. Trans. A* **2003**, *34*, 1371–1385. [CrossRef]
88. Klein, A.N.; Furlan, K.P.; Schroeder, R.M.; Hammes, G.; Binder, C.; Neto, J.B.R.; Probst, S.H.; de Mello, J.D.B. Thermodynamic aspects during the processing of sintered materials. *Powder Technol.* **2015**, *271*, 193–203. [CrossRef]
89. Balog, M.; Krizik, P.; Svec, P.; Orovcik, L. Industrially fabricated in-situ Al-AlN metal matrix composites (part A): Processing, thermal stability, and microstructure. *J. Alloy. Compd.* **2021**, *883*, 160858. [CrossRef]
90. Lu, J.; Qin, J.; Lu, W.; Liu, Y.; Gu, J.; Zhang, D. In situ preparation of $(TiB+TiC+Nd_2O_3)/Ti$ composites by powder metallurgy. *J. Alloy. Compd.* **2009**, *469*, 116–122. [CrossRef]
91. Rodeghiero, E.D.; Chisaki, J.; Giannelis, E.P. In Situ Microstructural Control of Ni/Al_2O_3 and $Ni/NiAl_2O_4$ Composites from Layered Double Hydroxides. *Chem. Mater.* **1997**, *9*, 478–484. [CrossRef]
92. Zhao, L.; Jiao, Y.; Zhao, M.; Zhang, J. Investigation on in situ Al0.5FeSi0.5/Al composites prepared by transient liquid phase sintering. *Mater. Des.* **2014**, *59*, 70–75. [CrossRef]
93. Feng, Y.; Geng, L.; Li, A.; Zheng, Z. Fabrication and characteristics of in situ Al12W particles reinforced aluminum matrix composites by reaction sintering. *Mater. Des.* **2010**, *31*, 965–967. [CrossRef]
94. Yang, Q.; Zhang, Y.; Zhang, H.; Zheng, R.; Xiao, W.; Ma, C. Fabrication of Al-based composites reinforced with in situ devitrified Al84Ni8.4Y4.8La1.8Co1 particles by hot pressing consolidation. *J. Alloy. Compd.* **2015**, *648*, 382–388. [CrossRef]
95. Nalivaiko, A.Y.; Arnautov, A.N.; Zmanovsky, S.V.; Ozherelkov, D.; Shurkin, P.K.; Gromov, A.A. Al–Al_2O_3 powder composites obtained by hydrothermal oxidation method: Powders and sintered samples characterization. *J. Alloy. Compd.* **2020**, *825*, 154024. [CrossRef]
96. Haghi, S.M.A.; Sajjadi, S.A.; Babakhani, A. In-situ fabrication of Al(Zn)$-Al_2O_3$ graded composite using the aluminothermic reaction during hot pressing. *Int. J. Miner. Met. Mater.* **2018**, *25*, 832–839. [CrossRef]
97. Moreno, M.F.; Balog, M.; Krizik, P. Mechanical characterization of PM aluminum composites by small punch test. *Matéria* **2018**, *23*. [CrossRef]

98. Nicoara, M.; Locovei, C.; Opris, C.; Ursu, D.; Vasiu, R.; Stoica, M. Optimizing the parameters for in situ fabrication of hybrid Al-Al_2O_3 composites. *J. Therm. Anal.* **2017**, *127*, 115–122. [CrossRef]
99. Kováč, P.; Balog, M.; Hušek, I.; Kopera, L.; Križik, P.; Rosová, A.; Kováč, J.; Kulich, M.; Čaplovičová, M. Properties of near- and sub-micrometre Al matrix composites strengthened with nano-scale in-situ Al_2O_3 aimed for low temperature applications. *Cryogenics* **2017**, *87*, 58–65. [CrossRef]
100. Balog, M.; Simancik, F.; Walcher, M.; Rajner, W.; Poletti, M.C. Extruded Al–Al_2O_3 composites formed in situ during consolidation of ultrafine Al powders: Effect of the powder surface area. *Mater. Sci. Eng. A* **2011**, *529*, 131–137. [CrossRef]
101. Dirras, G.; Gubicza, J.; Tingaud, D.; Billard, S. Microstructure of Al–Al_2O_3 nanocomposite formed by in situ phase transformation during Al nanopowder consolidation. *Mater. Chem. Phys.* **2011**, *129*, 846–852. [CrossRef]
102. Durai, T.; Das, K.; Das, S. Synthesis and characterization of Al matrix composites reinforced by in situ alumina particulates. *Mater. Sci. Eng. A* **2007**, *445-446*, 100–105. [CrossRef]
103. Yu, P.; Deng, C.-J.; Ma, N.-G.; Ng, D.H. A new method of producing uniformly distributed alumina particles in Al-based metal matrix composite. *Mater. Lett.* **2004**, *58*, 679–682. [CrossRef]
104. Lakra, S.; Bandyopadhyay, T.K.; Das, S.; Das, K. Thermal conductivity of in-situ dual matrix aluminum composites with segregated morphology. *Mater. Res. Bull.* **2021**, *144*, 111515. [CrossRef]
105. Chen, C.-F.; Huang, C.-N.; Kao, P.-W. Nanometer-sized δ^*-Al_2O_3-reinforced aluminum composites using the friction stir process: A TEM study. *Mater. Charact.* **2020**, *170*, 110704. [CrossRef]
106. Yu, P.; Kwok, C.; To, C.; Li, T.; Ng, D.H. Enhanced precipitation hardening in an alumina reinforced Al–Cu alloy matrix composite. *Compos. Part B Eng.* **2008**, *39*, 327–331. [CrossRef]
107. Kleiner, S.; Bertocco, F.; Khalid, F.A.; Beffort, O. Reactively Synthesized Nanostructured PM Aluminium Composite—Microstructure Stability and Elevated Temperature Hardness Response. *Adv. Eng. Mater.* **2005**, *7*, 380–383. [CrossRef]
108. Roy, D.; Basu, B.; Mallick, A.B. Tribological properties of Ti-aluminide reinforced Al-based in situ metal matrix composite. *Intermetallics* **2005**, *13*, 733–740. [CrossRef]
109. Lakra, S.; Bandyopadhyay, T.K.; Das, S.; Das, K. Synthesis and characterization of in-situ (Al–Al_3Ti–Al_2O_3)/Al dual matrix composite. *J. Alloy. Compd.* **2020**, *842*, 155745. [CrossRef]
110. Woo, K.D.; Kim, J.H.; Kwon, E.P.; Moon, M.S.; Lee, H.B.; Sato, T.; Liu, Z. Fabrication of Al matrix composite reinforced with submicrometer-sized Al_2O_3 particles formed by combustion reaction between HEMM Al and V_2O_5 composite particles during sintering. *Met. Mater. Int.* **2010**, *16*, 213–218. [CrossRef]
111. Mandal, A.; DAS, K.; DAS, S. Characterization of microstructure and properties of Al–Al_3Zr–Al_2O_3 composite. *Bull. Mater. Sci.* **2016**, *39*, 913–924. [CrossRef]
112. Chen, B.; Zhou, X.; Zhang, B.; Kondoh, K.; Li, J.; Qian, M. Microstructure, tensile properties and deformation behaviors of aluminium metal matrix composites co-reinforced by ex-situ carbon nanotubes and in-situ alumina nanoparticles. *Mater. Sci. Eng. A* **2020**, *795*, 139930. [CrossRef]
113. Dikici, B.; Gavgali, M. The effect of sintering time on synthesis of in situ submicron α-Al_2O_3 particles by the exothermic reactions of CuO particles in molten pure Al. *J. Alloy. Compd.* **2013**, *551*, 101–107. [CrossRef]
114. Zahid, G.; Azhar, T.; Musaddiq, M.; Rizvi, S.; Ashraf, M.; Hussain, N.; Iqbal, M. In situ processing and aging behaviour of an aluminium/Al_2O_3 composite. *Mater. Des.* **2011**, *32*, 1630–1635. [CrossRef]
115. Rong, X.; Zhang, X.; Zhao, D.; He, C.; Shi, C.; Liu, E.; Zhao, N. In-situ Al2O3-Al interface contribution towards the strength-ductility synergy of Al-CuO composite fabricated by solid-state reactive sintering. *Scr. Mater.* **2021**, *198*, 113825. [CrossRef]
116. Mallik, B.; Sikdar, K.; Roy, D. Tribological Performance of In Situ Reinforced Al-Based Metal Matrix Composite Processed by Spark Plasma Sintering. *Mater. Perform. Charact.* **2019**, *8*, 62–71. [CrossRef]
117. Huo, H.; Woo, K.D. In situ synthesis of Al_2O_3 particulate-reinforced Al matrix composite by low temperature sintering. *J. Mater. Sci.* **2006**, *41*, 3249–3253. [CrossRef]
118. Mintzer, S.; Ipohorski, M. Microstructure of aluminium-alumina-silica participate composites obtained by reactive sintering. *J. Mater. Sci.* **1995**, *30*, 4703–4709. [CrossRef]
119. Chen, J.; Jiang, X.; Lyu, L.; Li, Y.; Christian, P.; Sun, H.; Shu, R. Microstructure and properties of nano-C and in-situ Al_2O_3 reinforced aluminum matrix composites processed by high-pressure torsion. *Compos. Interfaces* **2022**, *29*, 579–595. [CrossRef]
120. Sharma, A.; Lee, H.; Ahn, B. Microstructure and properties of in-situ Al–Si/Al_2O_3 composites prepared by displacement reaction. *Powder Met.* **2021**, *64*, 192–197. [CrossRef]
121. Mokhnache, E.O.; Wang, G.; Geng, L.; Kaveendran, B.; Henniche, A.; Ramdani, N. In Situ Al Based Composites Fabricated in Al-SiO2-C System by Reaction Sintering. *JOM* **2015**, *67*, 1505–1514. [CrossRef]
122. Lakra, S.; Bandyopadhyay, T.K.; Das, S.; Das, K. In situ dual matrix composite with segregated microstructure fabricated from Al–TiO2–B2O3 system by mechanical thermal process. *J. Alloy. Compd.* **2021**, *860*, 158527. [CrossRef]
123. Ma, Z.Y.; Li, J.H.; Li, S.X.; Ning, X.G.; Lu, Y.X.; Bi, J. Property-microstructure correlation in in situ formed Al2O3, TiB2 and Al3Ti mixture-reinforced aluminium composites. *J. Mater. Sci.* **1996**, *31*, 741–747. [CrossRef]
124. Odhiambo, J.O.; Yoshida, M.; Otsu, A.; Yi, L.-F.; Onda, T.; Chen, Z.-C. Microstructure and tensile properties of in-situ synthesized and hot-extruded aluminum-matrix composites reinforced with hybrid submicron-sized ceramic particles. *J. Compos. Mater.* **2022**, *56*, 1987–2001. [CrossRef]

125. Yu, P.; Mei, Z.; Tjong, S. Structure, thermal and mechanical properties of in situ Al-based metal matrix composite reinforced with Al_2O_3 and TiC submicron particles. *Mater. Chem. Phys.* **2005**, *93*, 109–116. [CrossRef]
126. Liu, H.; Ruiying, Z.; Sen, Y.; Jinxuan, L.; Han, Y. Effect of TiO_2 particle size on reinforcements, reaction mode and kinetics in Al-TiO_2-C system. *Mater. Res. Express* **2019**, *6*, 116505. [CrossRef]
127. Fan, G.; Wang, Q.; Geng, L.; Wang, G.; Feng, Y. Preparation and characterization of aluminum matrix composites based on Al–WO3 system. *J. Alloy. Compd.* **2012**, *545*, 130–134. [CrossRef]
128. Feng, C.; Froyen, L. In-situ P/M Al/(ZrB_2 + Al_2O_3) MMCs: Processing, microstructure and mechanical characterization. *Acta Mater.* **1999**, *47*, 4571–4583. [CrossRef]
129. Wu, X.; Li, Y.; Jiang, P.; Sun, J. In situ formation mechanism of spinel-like Al5O6N and plate-like $Al_7O_3N_5$ in the two-step sintered Al–Al_2O_3 composites. *Mater. Chem. Phys.* **2021**, *271*, 124951. [CrossRef]
130. Xu, D.; Long, W.; Zhou, X. Microstructure and corrosion resistance of Al_3(Zr, Ti)/Al composite prepared by powder metallurgy. *Adv. Compos. Lett.* **2020**, *29*, 2633366X20906160. [CrossRef]
131. Cintas, J.; Cuevas, F.; Montes, J.M.; Caballero, E.; Herrera, E. Strengthening of ultrafine PM aluminium using nano-sized oxycarbonitride dispersoids. *Mater. Sci. Eng. A* **2011**, *528*, 8286–8291. [CrossRef]
132. Akçamlı, N.; Şenyurt, B. Fabrication and characterization of in-situ Al3Ni intermetallic and CeO2 particulate-reinforced aluminum matrix composites. *Ceram. Int.* **2021**, *47*, 21197–21206. [CrossRef]
133. Wan, Q.; Li, F.; Wang, W.; Hou, J.; Cui, W.; Li, Y. Study on In-Situ Synthesis Process of Ti–Al Intermetallic Compound-Reinforced Al Matrix Composites. *Materials* **2019**, *12*, 1967. [CrossRef]
134. Goyal, V.; Ravi, R.; Bakshi, S.R.; Soni, P.R. Development and Mechanical Properties of In Situ Al_3Ti-Reinforced Nanostructured AA6061 via Mechanical Alloying. *J. Mater. Eng. Perform.* **2019**, *28*, 117–122. [CrossRef]
135. Dursun, Ö.; Tansel, T.; Hatice, E. Ibrahim, Synthesis, Characterization and Dry Sliding Wear Behavior of In-situ Formed $TiAl_3$ Precipitate Reinforced A356 Alloy Produced by Mechanical Alloying Method. *Mater. Res.* **2015**, *18*, 813–820. [CrossRef]
136. Chianeh, V.A.; Hosseini, H.M.; Nofar, M. Micro structural features and mechanical properties of Al–Al3Ti composite fabricated by in-situ powder metallurgy route. *J. Alloy. Compd.* **2009**, *473*, 127–132. [CrossRef]
137. Sun, Z.; Hashimoto, H.; Wang, Q.; Park, Y.; Abe, T. Synthesis of Al–Al3Ti Composites using Pulse Discharge Sintering Process. *Mater. Trans. JIM* **2000**, *41*, 597–600. [CrossRef]
138. Guo, B.; Song, M.; Zhang, X.; Cen, X.; Li, W.; Chen, B.; Wang, Q. Achieving high combination of strength and ductility of Al matrix composite via in-situ formed Ti-Al_3Ti core-shell particle. *Mater. Charact.* **2020**, *170*, 110666. [CrossRef]
139. Vorotilo, S.; Nepapushev, A.; Moskovskikh, D.; Buinevich, V.; Trusov, G.; Kovalev, D.Y.; Semenyuk, A.; Stepanov, N.; Nalivaiko, A.; Gromov, A. Engineering of strong and hard in-situ Al-Al3Ti nanocomposite via high-energy ball milling and spark plasma sintering. *J. Alloy. Compd.* **2022**, *895*, 162676. [CrossRef]
140. Krizik, P.; Balog, M.; Nosko, M.; Riglos, M.V.C.; Dvorak, J.; Bajana, O. Ultrafine-grained Al composites reinforced with in-situ Al3Ti filaments. *Mater. Sci. Eng. A* **2016**, *657*, 6–14. [CrossRef]
141. Zhang, Q.; Xiao, B.; Wang, D.; Ma, Z. Formation mechanism of in situ Al3Ti in Al matrix during hot pressing and subsequent friction stir processing. *Mater. Chem. Phys.* **2011**, *130*, 1109–1117. [CrossRef]
142. Azarniya, A.; Hosseini, H.R.M.; Jafari, M.; Bagheri, N. Thermal decomposition of nanostructured Aluminum Titanate in an active Al matrix: A novel approach to fabrication of in situ Al/Al2O3–Al3Ti composites. *Mater. Des.* **2015**, *88*, 932–941. [CrossRef]
143. Azarniya, A.; Hosseini, H.R.M. A new method for fabrication of in situ Al/Al3Ti–Al2O3 nanocomposites based on thermal decomposition of nanostructured tialite. *J. Alloy. Compd.* **2015**, *643*, 64–73. [CrossRef]
144. Yıldırım, M.; Özyūrek, D. An Investigation of Wear Behaviors of AA7075 Al Hybrid Composites. *High Temp. Mater. Process.* **2018**, *37*, 619–624. [CrossRef]
145. Umeda, J.; Nishimura, N.; Fujii, H.; Jia, L.; Kondoh, K. In-Situ Formed Al_3Zr Compounds Reinforced Al Composites and Tribological Application. *Crystals* **2021**, *11*, 227. [CrossRef]
146. Geng, L.; Imai, T.; Mao, J.; Takagi, M.; Yao, C. Microstructure and high strain rate superplasticity ofin situcomposite synthesised from aluminium and nano ZrO_2 particles by powder metallurgy. *Mater. Sci. Technol.* **2001**, *17*, 187–194. [CrossRef]
147. Geng, L.; Zheng, Z.Z.; Yao, C.K.; Mao, J.F.; Imai, T. A new in situ composite fabricated by powder metallurgy with aluminum and nanocrystalline ZrO_2 particles. *J. Mater. Sci. Lett.* **2000**, *19*, 985–987. [CrossRef]
148. Velgosová, O.; Besterci, M.; Balloková, B. Influence of Al_4C_3 nanophase on structural stability and mechanical properties of Al-Al_4C_3 composites after thermal exposure. *Met. Res. Technol.* **2018**, *115*, 606. [CrossRef]
149. Ozdemir, A.T.; Bostan, B. Microstructure and electrical resistivity features in Al-Al_4C_3 in-situ composite after attrition milling and double sequence of compaction and high temperature treatment. *Met. Mater.* **2012**, *50*, 89–95. [CrossRef]
150. Arik, H.; Aydin, M.; Kurt, A.; Turker, M. Weldability of Al4C3–Al composites via diffusion welding technique. *Mater. Des.* **2005**, *26*, 555–560. [CrossRef]
151. Arik, H. Production and characterization of in situ Al4C3 reinforced aluminum-based composite produced by mechanical alloying technique. *Mater. Des.* **2004**, *25*, 31–40. [CrossRef]
152. Hu, J.; Zhang, J.; Luo, G.; Sun, Y.; Shen, Q.; Zhang, L. Effectively enhanced strength by interfacial reactions in in-situ carbon reinforced Al matrix composites. *Vacuum* **2021**, *188*, 110148. [CrossRef]

153. Wan, J.; Chen, B.; Feng, D.; Cao, L.; Shen, J.; Guo, B.; Li, J. Strengthening efficiency competition between carbon nanotubes (CNTs) and in-situ Al_4C_3 nanorods in CNTs/Al composites influenced by alumina characteristics. *Compos. Part A Appl. Sci. Manuf.* **2022**, *152*, 106704. [CrossRef]
154. Chen, B.; Jia, L.; Li, S.; Imai, H.; Takahashi, M.; Kondoh, K. In Situ Synthesized Al_4C_3Nanorods with Excellent Strengthening Effect in Aluminum Matrix Composites. *Adv. Eng. Mater.* **2014**, *16*, 972–975. [CrossRef]
155. Lekatou, A.; Sfikas, A.; Karantzalis, A. The influence of the fabrication route on the microstructure and surface degradation properties of Al reinforced by Al_9CO_2. *Mater. Chem. Phys.* **2017**, *200*, 33–49. [CrossRef]
156. Yuan, L.; Han, J.; Liu, J.; Jiang, Z. Mechanical properties and tribological behavior of aluminum matrix composites reinforced with in-situ AlB2 particles. *Tribol. Int.* **2016**, *98*, 41–47. [CrossRef]
157. Balog, M.; Yu, P.; Qian, M.; Behulova, M.; Švec, P.; Cicka, R. Nanoscaled Al–AlN composites consolidated by equal channel angular pressing (ECAP) of partially in situ nitrided Al powder. *Mater. Sci. Eng. A* **2013**, *562*, 190–195. [CrossRef]
158. Yu, P.; Balog, M.; Yan, M.; Schaffer, G.; Qian, M. In situ fabrication and mechanical properties of Al–AlN composite by hot extrusion of partially nitrided AA6061 powder. *J. Mater. Res.* **2011**, *26*, 1719–1725. [CrossRef]
159. Kondoh, K.; Umeda, J.; Watanabe, R. Cavitation erosion of aluminum matrix sintered composite with AlN dispersoids. *Wear* **2009**, *267*, 1511–1515. [CrossRef]
160. Kondoh, K.; Kimura, A.; Watanabe, R. Cavitation toughness ofin situnitrided Al–AlN composite sintered material. *Powder Met.* **2001**, *44*, 157–160. [CrossRef]
161. Balog, M.; Krizik, P.; Dvorak, J.; Bajana, O.; Krajcovic, J.; Drienovsky, M. Industrially fabricated in-situ Al-AlN metal matrix composites (part B): The mechanical, creep, and thermal properties. *J. Alloy. Compd.* **2022**, *909*, 164720. [CrossRef]
162. Caballero, E.S.; Cuevas, F.G.; Ternero, F.; Astacio, R.; Montes, J.M.; Cintas, J. In Situ Synthesis of Al-Based MMCs Reinforced with AlN by Mechanical Alloying under NH3 Gas. *Materials* **2018**, *11*, 823. [CrossRef]
163. Yang, W.-W.; Guo, Z.-M.; Guo, L.-C.; Cao, H.-Q.; Luo, J.; Ye, A.-P. In situ fabrication and properties of AlN dispersion strengthened 2024 aluminum alloy. *Int. J. Miner. Met. Mater.* **2014**, *21*, 1228–1232. [CrossRef]
164. Balog, M.; Krizik, P.; Yan, M.; Simancik, F.; Schaffer, G.; Qian, M. SAP-like ultrafine-grained Al composites dispersion strengthened with nanometric AlN. *Mater. Sci. Eng. A* **2013**, *588*, 181–187. [CrossRef]
165. Gostariani, R.; Asadabad, M.A.; Paydar, M.H.; Ebrahimi, R. Morphological and phase evaluation of Al/15 wt.% BN nanocomposite synthesized by planetary ball mill and sintering. *Adv. Powder Technol.* **2017**, *28*, 2232–2238. [CrossRef]
166. Kondoh, K.; Takeda, Y. Tribological property of in situ directly nitrided and sintered Al/AlN composite. *Powder Met.* **2000**, *43*, 69–75. [CrossRef]
167. Chen, C.-L.; Lin, C.-H. In-situ dispersed La oxides of Al6061 composites by mechanical alloying. *J. Alloy. Compd.* **2019**, *775*, 1156–1163. [CrossRef]
168. Zhou, Y.; Zan, Y.; Zheng, S.; Shao, X.; Jin, Q.; Zhang, B.; Wang, Q.; Xiao, B.; Ma, X.; Ma, Z. Thermally stable microstructures and mechanical properties of B4C-Al composite with in-situ formed Mg(Al)B. *J. Mater. Sci. Technol.* **2019**, *35*, 1825–1830. [CrossRef]
169. Hao, G.; Shi, C.-S.; Zhao, N.-Q.; Liu, E.-Z.; He, C.-N.; He, F.; Ma, L.-Y. Microstructural evolution and mechanical behavior of in situ synthesized MgAl2O4 whiskers reinforced 6061 Al alloy composite after hot extrusion and annealing. *Rare Met.* **2018**, 1–11. [CrossRef]
170. Xing, L.; Zhang, Y.; Shi, C.; Zhou, Y.; Zhao, N.; Liu, E.; He, C. In-situ synthesis of $MgAl_2O_4$ nanowhiskers reinforced 6061 aluminum alloy composites by reaction hot pressing. *Mater. Sci. Eng. A* **2014**, *617*, 235–242. [CrossRef]
171. Zhou, Y.; Zhao, N.; Shi, C.; Liu, E.; Du, X.; He, C. In-situ processing and aging behaviors of $MgAl_2O_4$ spinel whisker reinforced 6061Al composite. *Mater. Sci. Eng. A* **2014**, *598*, 114–121. [CrossRef]
172. Zhou, Y.; Yu, Z.; Zhao, N.; Shi, C.; Liu, E.; Du, X.; He, C. Microstructure and properties of in situ generated $MgAl_2O_4$ spinel whisker reinforced aluminum matrix composites. *Mater. Des.* **2013**, *46*, 724–730. [CrossRef]
173. Yu, Z.; Zhao, N.; Liu, E.; Shi, C.; Du, X.; Wang, J. Fabrication of aluminum matrix composites with enhanced mechanical properties reinforced by in situ generated $MgAl_2O_4$ whiskers. *Compos. Part A Appl. Sci. Manuf.* **2012**, *43*, 631–634. [CrossRef]
174. Jia, L.; Rong, X.; Zhao, D.; Zhang, X.; He, C.; Zhao, N. Microstructural characteristic and mechanical properties of the in-situ $MgAl_2O_4$ reinforced Al matrix composite based on Al-Mg-ZnO system. *J. Alloy. Compd.* **2022**, *891*, 161991. [CrossRef]
175. Li, J.; Wang, F.; Shi, C.; Liu, E.; He, C.; Zhao, N. High strength-ductility synergy of MgAlB4 whisker reinforced aluminum matrix composites achieved by in situ synthesis. *Mater. Sci. Eng. A* **2020**, *799*, 140127. [CrossRef]
176. Maiti, R.; Chakraborty, M. Synthesis and characterization of molybdenum aluminide nanoparticles reinforced aluminium matrix composites. *J. Alloy. Compd.* **2008**, *458*, 450–456. [CrossRef]
177. Chen, J.; Jiang, X.; Lyu, L.; Li, Y.; Christian, P.; Sun, H.; Shu, R. Microstructures and mechanical properties of nano-C and in situ Al2O3 reinforced aluminium matrix composites processed by equal-channel angular pressing. *J. Alloy. Compd.* **2021**, *876*, 160159. [CrossRef]
178. Wu, W.; Guo, B.; Xue, Y.; Shen, R.; Ni, S.; Song, M. Ni-AlxNiy core–shell structured particle reinforced Al-based composites fabricated by in-situ powder metallurgy technique. *Mater. Chem. Phys.* **2015**, *160*, 352–358. [CrossRef]
179. Ma, J.; Fan, C.; Chen, W.; Tan, H.; Zhu, S.; Li, Q.; Yang, J. Core-shell structure in situ reinforced aluminum matrix composites: Microstructure, mechanical and tribological properties. *J. Alloy. Compd.* **2022**, *901*, 163613. [CrossRef]

180. Li, J.; Jiang, X.; Shao, Z.; Zhu, D.; Johnson, S.S.; Luo, Z.; Zhu, M. Microstructure and Mechanical Properties of Multiphase Strengthened Al/Si/Al2O3/SiO2/MWCNTs Nanocomposites Sintered byIn SituVacuum Hot Pressing. *J. Nanomater.* **2015**, *2015*, 433. [CrossRef]
181. Daoush, W.; Francis, A.; Lin, Y.; German, R. An exploratory investigation on the in-situ synthesis of SiC/AlN/Al composites by spark plasma sintering. *J. Alloy. Compd.* **2015**, *622*, 458–462. [CrossRef]
182. Hu, Z.-Y.; Zhang, Z.-H.; Wang, H.; Li, S.-L.; Yin, S.-P.; Song, Q.; Cheng, X.-W. A rapid route for synthesizing Ti-(AlxTiy/UFG Al) core-multishell structured particles reinforced Al matrix composite with promising mechanical properties. *Mater. Sci. Eng. A* **2018**, *721*, 61–64. [CrossRef]
183. Guo, B.; Yi, J.; Ni, S.; Shen, R.; Song, M. Factors affecting the microstructure and mechanical properties of Ti-Al_3Ti core-shell-structured particle-reinforced Al matrix composites. *Philos. Mag.* **2016**, *96*, 1197–1211. [CrossRef]
184. Zhu, H.; Liu, J.; Wu, Y.; Zhang, Q.; Shi, Q.; Chen, Z.; Wang, L.; Zhang, F.; Wang, H. Hot Deformation Behavior and Workability of in Situ TiB2/7050Al Composites Fabricated by Powder Metallurgy. *Materials* **2020**, *13*, 5319. [CrossRef]
185. Lü, L.; Lai, M.; Su, Y.; Teo, H.; Feng, C. In situ TiB2 reinforced Al alloy composites. *Scr. Mater.* **2001**, *45*, 1017–1023. [CrossRef]
186. Zhang, J.; Zhang, D.; Zhu, H.; Xie, Z. In-situ TiB2 reinforced Al–4Cu matrix composites synthesized through microwave and conventional heating methods: Thermodynamics, dynamics and mechanical properties. *Mater. Chem. Phys.* **2021**, *270*, 124843. [CrossRef]
187. Birol, Y. Response to thermal exposure of Al/K2TiF6/C powder blends. *J. Alloy. Compd.* **2008**, *455*, 164–167. [CrossRef]
188. Qin, Q.D.; Huang, B.W.; Li, W.; Zeng, Z.Y. Preparation and Wear Resistance of Aluminum Composites Reinforced with In Situ Formed TiO/Al_2O. *J. Mater. Eng. Perform.* **2016**, *25*, 2029–2036. [CrossRef]
189. Wang, N.; Wu, B.; Wu, W.; Li, J.; Ge, C.; Dong, Y.; Zhang, L.; Wang, Y. Microstructure and properties of aluminium-high entropy alloy composites fabricated by mechanical alloying and spark plasma sintering. *Mater. Today Commun.* **2020**, *25*, 101366. [CrossRef]
190. Cai, S.; Ma, X.; Tang, H. In situ WAl12 particle-reinforced Al matrix composites synthesized by combining mechanical alloying and vacuum hot pressing technology. *J. Alloy. Compd.* **2012**, *520*, 170–173. [CrossRef]
191. Cai, S.G.; Ma, X.F.; Tang, H.G.; Zhao, W.; Zhu, C.J.; Yan, J.M.; Qiao, Z.H.; Zhao, B. Processing, Microstructure and Mechanical Properties of in Situ Al-based Metal Matrix Composite Reinforced with 22 wt.% WAl12 Particles. *Adv. Eng. Mater.* **2006**, *8*, 740–743. [CrossRef]
192. Li, T.; Ng, D.H. Fabrication of Al–$LiAlO_2$ metal matrix composites and crystalline γ-LiAlO. *Mater. Sci. Eng. A* **2007**, *445–446*, 652–656. [CrossRef]
193. Kaneko, J.; Sugamata, M.; Okubo, M. In Situ Dispersion of Yttrium and Calcium Oxides in Mechanically Alloyed Al-Y and Al-Ca Alloys. *Mater. Sci. Forum* **2000**, *331–337*, 1209–1214. [CrossRef]
194. Yu, P.; Deng, C.-J.; Ma, N.-G.; Yau, M.-Y.; Ng, D.H. Formation of nanostructured eutectic network in α-Al2O3 reinforced Al–Cu alloy matrix composite. *Acta Mater.* **2003**, *51*, 3445–3454. [CrossRef]
195. Deqing, W.; Ziyuan, S. Aluminothermic Reduction of Silica for the Synthesis of Alumina-Aluminum-Silicon Composite. *J. Mater. Synth. Process.* **2001**, *9*, 241–246. [CrossRef]
196. Zhang, W.; Chai, D.; Ran, G.; Zhou, J. Study on microstructure and tensile properties of in situ fiber reinforced aluminum matrix composites. *Mater. Sci. Eng. A* **2008**, *476*, 157–161. [CrossRef]
197. Liu, L.; Li, Y.; Zhang, H.; Cheng, X.; Mu, X.; Fan, Q.; Ge, Y.; Guo, S. Simultaneously enhancing strength and ductility in graphene nanoplatelets reinforced titanium (GNPs/Ti) composites through a novel three-dimensional interface design. *Compos. Part B Eng.* **2021**, *216*, 108851. [CrossRef]
198. Vasanthakumar, K.; Ghosh, S.; Koundinya, N.; Ramaprabhu, S.; Bakshi, S.R. Synthesis and mechanical properties of TiCx and Ti(C,N) reinforced Titanium matrix in situ composites by reactive spark plasma sintering. *Mater. Sci. Eng. A* **2019**, *759*, 30–39. [CrossRef]
199. Yu, J.; Zhao, Y.; Zhao, Q.; Zhang, W.; Huo, W.; Zhang, Y. Microstructure and Properties of Titanium Matrix Composites Synergistically Reinforced by Graphene Oxide and Alloying Elements. *Adv. Eng. Mater.* 2022, *in press*. [CrossRef]
200. Xiong, Y.; Du, M.; Zhang, F.; Saba, F.; Shang, C. Preparation and mechanical properties of titanium alloy matrix composites reinforced by Ti_3AlC and TiC ceramic particulates. *J. Alloy. Compd.* **2021**, *886*, 161216. [CrossRef]
201. Zhang, X.; He, M.; Yang, W.; Wu, K.; Zhan, Y.; Song, F. Structure and mechanical properties of in-situ titanium matrix composites with homogeneous Ti_5Si_3 equiaxial particle-reinforcements. *Mater. Sci. Eng. A* **2017**, *698*, 73–79. [CrossRef]
202. Sumida, M.; Kondoh, K. In-Situ Synthesis of Ti Matrix Composite Reinforced with Dispersed Ti_5Si_3 Particles via Spark Plasma Sintering. *Mater. Trans.* **2005**, *46*, 2135–2141. [CrossRef]
203. Lu, Q.; Lv, Y.; Zhang, C.; Zhang, H.; Chen, W.; Xu, Z.; Feng, P.; Fan, J. Highly oxidation-resistant Ti-Mo alloy with two-scale network Ti_5Si_3 reinforcement. *J. Mater. Sci. Technol.* **2022**, *110*, 24–34. [CrossRef]
204. Huang, L.; Wang, S.; Geng, L.; Kaveendran, B.; Peng, H.-X. Low volume fraction in situ (Ti_5Si_3 + Ti_2C)/Ti hybrid composites with network microstructure fabricated by reaction hot pressing of Ti–SiC system. *Compos. Sci. Technol.* **2013**, *82*, 23–28. [CrossRef]
205. Huang, K.; Chen, W.; Wu, M.; Wang, J.; Jiang, K.; Liu, J. Microstructure and densification of the Ti6Al4V–70%TiB2 metal-ceramic by coupled multi-physical fields-activated sintering. *J. Alloy. Compd.* **2020**, *820*, 153091. [CrossRef]

206. Mohammadzadeh, A.; Azadbeh, M.; Danninger, H.; Namini, A.S. Ti–TiB2 composites consolidated by spark plasma sintering: Reaction mechanism, characteristics of in-situ formed phases and densification behavior. *Mater. Chem. Phys.* **2020**, *242*, 122556. [CrossRef]
207. Cao, Y.; Liu, Y.; Li, Y.; Liu, B.; Xu, R. Hot deformation behavior of nano-sized TiB reinforced Ti-6Al-4V metal matrix composites. *Mech. Mater.* **2020**, *141*, 103260. [CrossRef]
208. Namini, A.S.; Dilawary, S.A.A.; Motallebzadeh, A.; Asl, M.S. Effect of TiB2 addition on the elevated temperature tribological behavior of spark plasma sintered Ti matrix composite. *Compos. Part B Eng.* **2019**, *172*, 271–280. [CrossRef]
209. Singh, H.; Hayat, M.; He, Z.; Peterson, V.K.; Das, R.; Cao, P. In situ neutron diffraction observations of Ti-TiB composites. *Compos. Part A Appl. Sci. Manuf.* **2019**, *124*, 105501. [CrossRef]
210. Singh, H.; Hayat, M.; Zhang, H.; Das, R.; Cao, P. Effect of TiB2 content on microstructure and properties of in situ Ti-TiB composites. *Int. J. Miner. Met. Mater.* **2019**, *26*, 915–924. [CrossRef]
211. Cai, C.; He, S.; Li, L.; Teng, Q.; Song, B.; Yan, C.; Wei, Q.; Shi, Y. In-situ TiB/Ti-6Al-4V composites with a tailored architecture produced by hot isostatic pressing: Microstructure evolution, enhanced tensile properties and strengthening mechanisms. *Compos. Part B Eng.* **2019**, *164*, 546–558. [CrossRef]
212. Miklaszewski, A.; Jurczyk, M. Mechanical Alloying and Electrical Current-Assisted Sintering Adopted for In Situ Ti-TiB Metal Matrix Composite Processing. *Materials* **2019**, *12*, 653. [CrossRef]
213. Namini, A.S.; Motallebzadeh, A.; Nayebi, B.; Asl, M.S.; Azadbeh, M. Microstructure–mechanical properties correlation in spark plasma sintered Ti–4.8 wt.% TiB2 composites. *Mater. Chem. Phys.* **2019**, *223*, 789–796. [CrossRef]
214. Wang, H.; Hu, Z.-Y.; Cheng, X.-W.; Zhang, Z.-H.; Song, Q.; Li, X.-Y. A rapid route to fabricate in situ TiB-whisker-reinforced Ti-6Al-4V alloy composites by spark plasma sintering and heat treatment. *Mater. Res. Express* **2019**, *6*, 1265d3. [CrossRef]
215. Mohammadzadeh, A.; Namini, A.S.; Azadbeh, M.; Motallebzadeh, A. On the physical and mechanical properties of spark plasma sintered pure Ti and Ti-TiB composite. *Mater. Res. Express* **2018**, *5*, 126512. [CrossRef]
216. Chaudhari, R.; Bauri, R. A novel spark plasma sintering route to process high-strength Ti–4Al–2Fe/TiB nano-composite. *Mater. Sci. Technol.* **2018**, *34*, 2008–2017. [CrossRef]
217. Xu, R.; Liu, B.; Liu, Y.; Cao, Y.; Guo, W.; Nie, Y.; Liu, S. High Temperature Deformation Behavior of In-Situ Synthesized Titanium-Based Composite Reinforced with Ultra-Fine TiB Whiskers. *Materials* **2018**, *11*, 1863. [CrossRef] [PubMed]
218. Feng, Y.; Cui, G.; Zhang, W.; Chen, W.; Yu, Y. High temperature tensile fracture characteristics of the oriented TiB whisker reinforced TA15 matrix composites fabricated by pre-sintering and canned extrusion. *J. Alloy. Compd.* **2018**, *738*, 164–172. [CrossRef]
219. Chen, W.; Yang, J.; Zhang, W.; Wang, M.; Du, D.; Cui, G. Influence of TiBw volume fraction on microstructure and high-temperature properties of in situ TiBw/Ti_6Al_4V composites with TiBw columnar reinforced structure fabricated by pre-sintering and canned extrusion. *Adv. Powder Technol.* **2017**, *28*, 2346–2356. [CrossRef]
220. Namini, A.S.; Azadbeh, M.; Asl, M.S. Effect of TiB2 content on the characteristics of spark plasma sintered Ti–TiBw composites. *Adv. Powder Technol.* **2017**, *28*, 1564–1572. [CrossRef]
221. Miklaszewski, A. Ultrafast densification and microstructure evolution of in situ Ti/TiB metal matrix composite obtained by PPS approach. *Int. J. Refract. Met. Hard Mater.* **2017**, *65*, 34–38. [CrossRef]
222. Namini, A.S.; Azadbeh, M. Microstructural characterisation and mechanical properties of spark plasma-sintered TiB_2-reinforced titanium matrix composite. *Powder Met.* **2017**, *60*, 22–32. [CrossRef]
223. Zhang, W.; Feng, Y.; Chen, W.; Yang, J. Effects of heat treatment on the microstructure and mechanical properties of in situ inhomogeneous TiBw/Ti_6Al_4V composite fabricated by pre–sintering and canned powder extrusion. *J. Alloy. Compd.* **2017**, *693*, 1116–1123. [CrossRef]
224. Cai, C.; Song, B.; Qiu, C.; Li, L.; Xue, P.; Wei, Q.; Zhou, J.; Nan, H.; Chen, H.; Shi, Y. Hot isostatic pressing of in-situ TiB/Ti-6Al-4V composites with novel reinforcement architecture, enhanced hardness and elevated tribological properties. *J. Alloy. Compd.* **2017**, *710*, 364–374. [CrossRef]
225. Ozerov, M.; Klimova, M.; Vyazmin, A.; Stepanov, N.; Zherebtsov, S. Orientation relationship in a Ti/TiB metal-matrix composite. *Mater. Lett.* **2017**, *186*, 168–170. [CrossRef]
226. Miklaszewski, A. Effect of starting material character and its sintering temperature on microstructure and mechanical properties of super hard Ti/TiB metal matrix composites. *Int. J. Refract. Met. Hard Mater.* **2015**, *53*, 56–60. [CrossRef]
227. Yu, Y.; Zhang, W.; Dong, W.; Yang, J.; Feng, Y. Effects of pre-sintering on microstructure and properties of TiBw/Ti6Al4V composites fabricated by hot extrusion with steel cup. *Mater. Sci. Eng. A* **2015**, *638*, 38–45. [CrossRef]
228. Ropars, L.; Dehmas, M.; Gourdet, S.; Delfosse, J.; Tricker, D.; Aeby-Gautier, E. Structure evolutions in a Ti–6Al–4V matrix composite reinforced with TiB, characterised using high energy X-ray diffraction. *J. Alloy. Compd.* **2015**, *624*, 179–188. [CrossRef]
229. Cao, Y.; Zeng, F.; Lu, J.; Liu, B.; Liu, Y.; Li, Y. In Situ Synthesis of TiB/Ti6Al4V Composites Reinforced with Nano TiB through SPS. *Mater. Trans.* **2015**, *56*, 259–263. [CrossRef]
230. Yan, Z.; Chen, F.; Cai, Y.; Zheng, Y. Microstructure and mechanical properties of in-situ synthesized TiB whiskers reinforced titanium matrix composites by high-velocity compaction. *Powder Technol.* **2014**, *267*, 309–314. [CrossRef]
231. Attar, H.; Bönisch, M.; Calin, M.; Zhang, L.; Zhuravleva, K.; Funk, A.; Scudino, S.; Yang, C.; Eckert, J. Comparative study of microstructures and mechanical properties of in situ Ti–TiB composites produced by selective laser melting, powder metallurgy, and casting technologies. *J. Mater. Res.* **2014**, *29*, 1941–1950. [CrossRef]

232. Chaudhari, R.; Bauri, R. Reaction mechanism, microstructure and properties of Ti–TiB insitu composite processed by spark plasma sintering. *Mater. Sci. Eng. A* **2013**, *587*, 161–167. [CrossRef]
233. Huang, L.; Zhang, Y.; Liu, B.; Song, X.; Geng, L.; Wu, L. Superplastic tensile characteristics of in situ TiBw/Ti6Al4V composites with novel network microstructure. *Mater. Sci. Eng. A* **2013**, *581*, 128–132. [CrossRef]
234. Huang, L.; Zhang, Y.; Geng, L.; Wang, B.; Ren, W. Hot compression characteristics of TiBw/Ti6Al4V composites with novel network microstructure using processing maps. *Mater. Sci. Eng. A* **2013**, *580*, 242–249. [CrossRef]
235. Wei, S.; Zhang, Z.-H.; Wang, F.-C.; Shen, X.-B.; Cai, H.-N.; Lee, S.-K.; Wang, L. Effect of Ti content and sintering temperature on the microstructures and mechanical properties of TiB reinforced titanium composites synthesized by SPS process. *Mater. Sci. Eng. A* **2013**, *560*, 249–255. [CrossRef]
236. Zhang, Z.-H.; Shen, X.-B.; Wang, F.-C.; Wei, S.; Li, S.-K.; Cai, H.-N. Microstructure characteristics and mechanical properties of TiB/Ti-1.5Fe-2.25Mo composites synthesized in situ using SPS process. *Trans. Nonferrous Met. Soc. China* **2013**, *23*, 2598–2604. [CrossRef]
237. Huang, L.; Yang, F.; Hu, H.; Rong, X.; Geng, L.; Wu, L. TiB whiskers reinforced high temperature titanium Ti60 alloy composites with novel network microstructure. *Mater. Des.* **2013**, *51*, 421–426. [CrossRef]
238. Huang, L.; Geng, L.; Wang, B.; Wu, L. Effects of volume fraction on the microstructure and tensile properties of in situ TiBw/Ti6Al4V composites with novel network microstructure. *Mater. Des.* **2013**, *45*, 532–538. [CrossRef]
239. Huang, L.; Wang, S.; Dong, Y.; Zhang, Y.; Pan, F.; Geng, L.; Peng, H. Tailoring a novel network reinforcement architecture exploiting superior tensile properties of in situ TiBw/Ti composites. *Mater. Sci. Eng. A* **2012**, *545*, 187–193. [CrossRef]
240. Koo, M.Y.; Park, J.S.; Park, M.K.; Kim, K.T.; Hong, S.H. Effect of aspect ratios of in situ formed TiB whiskers on the mechanical properties of TiBw/Ti–6Al–4V composites. *Scr. Mater.* **2012**, *66*, 487–490. [CrossRef]
241. Huang, L.; Geng, L.; Peng, H.-X.; Kaveendran, B. High temperature tensile properties of in situ TiBw/Ti6Al4V composites with a novel network reinforcement architecture. *Mater. Sci. Eng. A* **2012**, *534*, 688–692. [CrossRef]
242. Shen, X.; Zhang, Z.; Wei, S.; Wang, F.; Lee, S. Microstructures and mechanical properties of the in situ TiB–Ti metal–matrix composites synthesized by spark plasma sintering process. *J. Alloy. Compd.* **2011**, *509*, 7692–7696. [CrossRef]
243. Zhang, Z.-H.; Shen, X.-B.; Wen, S.; Luo, J.; Lee, S.-K.; Wang, F.-C. In situ reaction synthesis of Ti–TiB composites containing high volume fraction of TiB by spark plasma sintering process. *J. Alloy. Compd.* **2010**, *503*, 145–150. [CrossRef]
244. Morsi, K.; Patel, V.; Naraghi, S.; Garay, J. Processing of titanium–titanium boride dual matrix composites. *J. Mater. Process. Technol.* **2008**, *196*, 236–242. [CrossRef]
245. Feng, H.; Jia, D.; Zhou, Y. Influence factors of ball milling process on BE powder for reaction sintering of TiB/Ti–4.0Fe–7.3Mo composite. *J. Mater. Process. Technol.* **2006**, *182*, 79–83. [CrossRef]
246. Feng, H.; Zhou, Y.; Jia, D.; Meng, Q.; Rao, J. Growth Mechanism of In Situ TiB Whiskers in Spark Plasma Sintered TiB/Ti Metal Matrix Composites. *Cryst. Growth Des.* **2006**, *6*, 1626–1630. [CrossRef]
247. Feng, H.B.; Jia, D.C.; Zhou, Y. Spark plasma sintering reaction synthesized TiB reinforced titanium matrix composites. *Compos. Part A Appl. Sci. Manuf.* **2005**, *36*, 558–563. [CrossRef]
248. Feng, H.; Zhou, Y.; Jia, D.; Meng, Q. Microstructure and mechanical properties of in situ TiB reinforced titanium matrix composites based on Ti–FeMo–B prepared by spark plasma sintering. *Compos. Sci. Technol.* **2004**, *64*, 2495–2500. [CrossRef]
249. Gorsse, S.; Petitcorps, Y.; Matar, S.; Rebillat, F. Investigation of the Young's modulus of TiB needles in situ produced in titanium matrix composite. *Mater. Sci. Eng. A* **2003**, *340*, 80–87. [CrossRef]
250. Panda, K.B.; Chandran, K.S.R. Titanium-titanium boride (Ti-TiB) functionally graded materials through reaction sintering: Synthesis, microstructure, and properties. *Met. Mater. Trans. Phys. Metall. Mater. Sci.* **2003**, *34*, 1993–2003. [CrossRef]
251. Godfrey, T.; Wisbey, A.; Goodwin, P.; Bagnall, K.; Ward-Close, C. Microstructure and tensile properties of mechanically alloyed Ti–6A1–4V with boron additions. *Mater. Sci. Eng. A* **2000**, *282*, 240–250. [CrossRef]
252. Gorsse, S.; Chaminade, J.; Le Petitcorps, Y. In situ preparation of titanium base composites reinforced by TiB single crystals using a powder metallurgy technique. *Compos. Part A Appl. Sci. Manuf.* **1998**, *29*, 1229–1234. [CrossRef]
253. Hagiwara, M.; Kim, S.-J. Low cost synthesis and property evaluation of P/M Ti alloys and ti-based particulate composites. *Met. Mater.* **1998**, *4*, 141–149. [CrossRef]
254. Kumar, R.; Antonov, M.; Liu, L.; Hussainova, I. Sliding wear performance of in-situ spark plasma sintered Ti-TiBw composite at temperatures up to 900 °C. *Wear* **2021**, *476*, 203663. [CrossRef]
255. Luo, G.; Chen, J.; Qin, J.; Sun, Y.; Zhang, J.; Li, Y.; Shen, Q. Microstructure and strengthening mechanism of boride in-situ reinforced titanium matrix composites prepared by plasma activated sintering. *Ceram. Int.* **2021**, *47*, 15910–15922. [CrossRef]
256. Song, B.-N.; Cao, J. Sintering properties of in situ Ti-TiB microlattices created by 3D extrusion printing of TiH_2 + TiB_2 inks. *J. Cent. South Univ.* **2021**, *28*, 1078–1088. [CrossRef]
257. Chang, S.-H.; Liang, C.-H.; Huang, K.-T.; Liang, C. Evaluation of the microstructures, strengthening mechanisms and corrosion behaviors of TiB2 powder added to Ti–8Ta–6Ni alloys through the vacuum sintering process. *J. Alloy. Compd.* **2021**, *857*, 157629. [CrossRef]
258. Song, Y.; Dong, S.; Stasiuk, O.; Savvakin, D.; Ivasishin, O. Synthesis of Ti/TiB Composites via Hydrogen-Assisted Blended Elemental Powder Metallurgy. *Front. Mater.* **2020**, *7*, 572005. [CrossRef]
259. Feng, Y.; Hou, J.; Gao, L.; Cui, G.; Zhang, W. Research on the inhomogeneity and joint interface of in situ oriented TiBw/TA15 composites fabricated by vacuum hot-pressing sintering and canned extrusion. *J. Manuf. Process.* **2020**, *59*, 791–800. [CrossRef]

260. Tabrizi, S.G.; Babakhani, A.; Sajjadi, S.A.; Lü, W.-J. Microstructural aspects of in-situ TiB reinforced Ti–6Al–4V composite processed by spark plasma sintering. *Trans. Nonferrous Met. Soc. China* **2015**, *25*, 1460–1467. [CrossRef]
261. Zhou, Y.; Yang, F.; Chen, C.; Shao, Y.; Lu, B.; Sui, Y.; Guo, Z. Mechanical property and microstructure of in-situ TiB/Ti composites via vacuum sintering and hot rolling. *J. Alloy. Compd.* **2022**, *911*, 165042. [CrossRef]
262. Chen, R.; An, Q.; Wang, S.; Huang, L.; Zhang, R.; Wang, C.; Zhou, S.; Geng, L. Overcoming the strength-ductility trade-off dilemma in TiBw/TC18 composites via network architecture with trace reinforcement. *Mater. Sci. Eng. A* **2022**, *842*, 143092. [CrossRef]
263. Song, Y.; Ma, G.; Qiu, F.; Stasiuk, O.; Savvakin, D.; Ivasishin, O.; Xu, X.; Cheng, T. Nearly dense Ti–6Al–4V/TiB composites manufactured via hydrogen assisted BEPM. *Ceram. Int.* **2022**, *48*, 10902–10910. [CrossRef]
264. Song, Y.; Qiu, F.; Savvakin, D.; Xu, X.; Stasiuk, O.; Ivasishin, O.; Cheng, T. In Situ Ti6Al4V/TiB Composites Prepared by Hydrogen-Assisted Sintering of Blends Containing TiH_2 and Ball-Milled Ti + TiB_2 Powders. *Materials* **2022**, *15*, 1049. [CrossRef] [PubMed]
265. Wang, Q.; Zhang, Z.-H.; Su, T.-J.; Cheng, X.-W.; Li, X.-Y.; Zhang, S.-Z.; He, J.-Y. A TiB whisker-reinforced titanium matrix composite with controllable orientation: A novel method and superior strengthening effect. *Mater. Sci. Eng. A* **2022**, *830*, 142309. [CrossRef]
266. Yang, C.; Wang, J.; Kang, L.; Chen, T.; Zhang, W.; Liu, L.; Li, Y. Improvement in tensile plasticity of pressureless-sintered TiBw/Ti composites by evading Kirkendall's pore. *Powder Technol.* **2022**, *396*, 444–448. [CrossRef]
267. Lark, A.; Du, J.; Chandran, K.R. Material design and processing of a new class of titanium boride cermets with tough metallic phases and mechanical properties. *J. Mater. Res.* **2018**, *33*, 4296–4306. [CrossRef]
268. Ranjan, A.; Tyagi, R.; Jindal, V.; Chandran, K.S.R. Investigation on Wear Characteristics of TiBFe Composites Containing 10 at.% Boron and 10–30 at.% Iron. *J. Mater. Eng. Perform.* **2020**, *29*, 6333–6342. [CrossRef]
269. Hayat, M.D.; Singh, H.; Miodowski, A.; Bokhari, S.W.; He, Z.; Cao, P. Fabrication, microstructure and mechanical properties of in situ formed particle reinforced titanium matrix composite. *Int. J. Refract. Met. Hard Mater.* **2020**, *92*, 105257. [CrossRef]
270. Jiao, Y.; Huang, L.; Wei, S.; Peng, H.; An, Q.; Jiang, S.; Geng, L. Constructing two-scale network microstructure with nano-Ti5Si3 for superhigh creep resistance. *J. Mater. Sci. Technol.* **2019**, *35*, 1532–1542. [CrossRef]
271. Jiao, Y.; Huang, L.; An, Q.; Jiang, S.; Gao, Y.; Cui, X.; Geng, L. Effects of Ti5Si3 characteristics adjustment on microstructure and tensile properties of in-situ (Ti_5Si_3 + TiBw)/Ti6Al4V composites with two-scale network architecture. *Mater. Sci. Eng. A* **2016**, *673*, 595–605. [CrossRef]
272. Sun, Y.; Zhang, J.; Luo, G.; Shen, Q.; Zhang, L. Microstructure and Mechanical Behaviors of Titanium Matrix Composites Containing in situ Whiskers Synthesized via Plasma Activated Sintering. *Materials* **2018**, *11*, 544. [CrossRef]
273. Namini, A.S.; Asl, M.S.; Delbari, S.A. Influence of Sintering Temperature on Microstructure and Mechanical Properties of Ti–Mo–B4C Composites. *Met. Mater. Int.* **2021**, *27*, 1092–1102. [CrossRef]
274. Chaudhari, R.; Bauri, R. A novel functionally gradient Ti/TiB/TiC hybrid composite with wear resistant surface layer. *J. Alloy. Compd.* **2018**, *744*, 438–444. [CrossRef]
275. Namini, A.S.; Azadbeh, M.; Asl, M.S. Effects of in-situ formed TiB whiskers on microstructure and mechanical properties of spark plasma sintered Ti–B4C and Ti–TiB2 composites. *Sci. Iran.* **2017**, *25*, 762–771. [CrossRef]
276. Huang, L.; Wang, L.; Qian, M.; Zou, J. High tensile-strength and ductile titanium matrix composites strengthened by TiB nanowires. *Scr. Mater.* **2017**, *141*, 133–137. [CrossRef]
277. Li, S.; Kondoh, K.; Imai, H.; Chen, B.; Jia, L.; Umeda, J.; Fu, Y. Strengthening behavior of in situ -synthesized (TiC–TiB)/Ti composites by powder metallurgy and hot extrusion. *Mater. Des.* **2016**, *95*, 127–132. [CrossRef]
278. Balaji, V.S.; Kumaran, S. Dry Sliding Wear Behavior of Titanium–(TiB + TiC) in situ Composite Developed by Spark Plasma Sintering. *Tribol. Trans.* **2015**, *58*, 698–703. [CrossRef]
279. Tabrizi, S.G.; Sajjadi, S.A.; Babakhani, A.; Lu, W. Influence of spark plasma sintering and subsequent hot rolling on microstructure and flexural behavior of in-situ TiB and TiC reinforced Ti6Al4V composite. *Mater. Sci. Eng. A* **2015**, *624*, 271–278. [CrossRef]
280. Jia, L.; Chen, B.; Li, S.-F.; Imai, H.; Kondoh, K. Pinning Effect of In-Situ TiCp and TiBw on the Grain Size and Room Temperature Strength of (TiC + TiB)/Ti Composites. *KONA Powder Part. J.* **2015**, *32*, 264–269. [CrossRef]
281. Jia, L.; Chen, B.; Li, S.; Imai, H.; Takahashi, M.; Kondoh, K. Stability of strengthening effect of in situ formed TiCp and TiBw on the elevated temperature strength of (TiCp + TiBw)/Ti composites. *J. Alloy. Compd.* **2014**, *614*, 29–34. [CrossRef]
282. Jia, L.; Li, S.-F.; Imai, H.; Chen, B.; Kondoh, K. Size effect of B4C powders on metallurgical reaction and resulting tensile properties of Ti matrix composites by in-situ reaction from Ti–B4C system under a relatively low temperature. *Mater. Sci. Eng. A* **2014**, *614*, 129–135. [CrossRef]
283. Balaji, V.S.; Kumaran, S. Synthesis and Characterization of Ti/(TiB + TiC) Hybrid in-situ Composites by Spark Plasma Sintering. *Trans. Indian Inst. Met.* **2013**, *66*, 339–341. [CrossRef]
284. Zhou, P.; Qin, J.N.; Lu, W.J.; Zhang, D. Microstructure and mechanical properties of *in situ* synthesised (TiC+TiB)/Ti–6Al–4V composites prepared by powder metallurgy. *Mater. Sci. Technol.* **2011**, *27*, 1788–1792. [CrossRef]
285. Vadayar, K.S.; Poshal, G.; Prasad, V.V.B. Reaction Synthesis of Titanium Matrix Composites Through Powder Metallurgy Processing Technique. *Trans. Indian Inst. Met.* **2011**, *64*, 439–445. [CrossRef]
286. Bhat, B.R.; Subramanyam, J.; Prasad, V.B. Preparation of Ti-TiB-TiC & Ti-TiB composites by in-situ reaction hot pressing. *Mater. Sci. Eng. A* **2002**, *325*, 126–130. [CrossRef]

287. Jeong, H.W.; Kim, S.J.; Hyun, Y.T.; Lee, Y.T. Densification and compressive strength ofin-situ processed Ti/TiB composites by powder metallurgy. *Met. Mater. Int.* **2002**, *8*, 25–35. [CrossRef]
288. Hagiwara, M.; Arimoto, N.; Emura, S.; Kawabe, Y.; Suzuki, H.G. Mechanical Properties of Particulate Reinforced Titanium-based Metal Matrix Composites Produced by the Blended Elemental P/M Route. *ISIJ Int.* **1992**, *32*, 909–916. [CrossRef]
289. Singh, N.; Ummethala, R.; Karamched, P.S.; Sokkalingam, R.; Gopal, V.; Manivasagam, G.; Prashanth, K.G. Spark plasma sintering of Ti6Al4V metal matrix composites: Microstructure, mechanical and corrosion properties. *J. Alloy. Compd.* **2021**, *865*, 158875. [CrossRef]
290. Song, B.; Kenel, C.; Dunand, D.C. 3D ink-extrusion printing and sintering of Ti, Ti-TiB and Ti-TiC microlattices. *Addit. Manuf.* **2020**, *35*, 101412. [CrossRef]
291. Nguyen, T.P.; Delbari, S.A.; Azizian-Kalandaragh, Y.; Babapoor, A.; Van Le, Q.; Namini, A.S.; Shokouhimehr, M.; Asl, M.S. Characteristics of quadruplet Ti–Mo–TiB_2–TiC composites prepared by spark plasma sintering. *Ceram. Int.* **2020**, *46*, 20885–20895. [CrossRef]
292. Hu, Z.-Y.; Peng, H.-C.; Zhang, Z.-H.; Song, P.; Chen, M.; Ding, Y.-S.; Liang, Y.-Y.; Li, S.-M. Influence of the sintering temperature on the microstructure, mechanical properties and densification characteristics of (TiB + TiC)/TC4 composite. *Mater. Res. Express* **2021**, *8*, 126517. [CrossRef]
293. Montealegre-Melendez, I.; Arévalo, C.; Ariza, E.; Pérez-Soriano, E.M.; Rubio-Escudero, C.; Kitzmantel, M.; Neubauer, E. Analysis of the Microstructure and Mechanical Properties of Titanium-Based Composites Reinforced by Secondary Phases and B4C Particles Produced via Direct Hot Pressing. *Materials* **2017**, *10*, 1240. [CrossRef]
294. Arévalo, C.; Montealegre-Meléndez, I.; Ariza, E.; Kitzmantel, M.; Rubio-Escudero, C.; Neubauer, E. Influence of Sintering Temperature on the Microstructure and Mechanical Properties of In Situ Reinforced Titanium Composites by Inductive Hot Pressing. *Materials* **2016**, *9*, 919. [CrossRef]
295. Bram, M.; Aubertin, F.; Venskutonis, A.; Breme, J. Kinetics of the phase transformation and wear resistance of in-situ processed titanium matrix composites based on Ti–Fe–B. *Mater. Sci. Eng. A* **1999**, *264*, 74–80. [CrossRef]
296. Sun, F.; Huang, L.; Zhang, R.; Wang, S.; Jiang, S.; Sun, Y.; An, Q.; Jiao, Y.; Geng, L. In-situ synthesis and superhigh modulus of network structured TiC/Ti composites based on diamond-Ti system. *J. Alloy. Compd.* **2020**, *834*, 155248. [CrossRef]
297. Bai, M.; Namus, R.; Xu, Y.; Guan, D.; Rainforth, M.W.; Inkson, B.J. In-situ Ti-6Al-4V/TiC composites synthesized by reactive spark plasma sintering: Processing, microstructure, and dry sliding wear behaviour. *Wear* **2019**, *432–433*, 202944. [CrossRef]
298. Liu, Z.; Zhang, D.C.; Gong, L.J.; Lin, J.G.; Wen, C. Microstructures and mechanical properties of in situ TiC-β-Ti-Nb composites with ultrafine grains fabricated by high-pressure sintering. *Sci. Rep.* **2018**, *8*, 9496. [CrossRef] [PubMed]
299. Zhang, C.; Guo, Z.; Yang, F.; Wang, H.; Shao, Y.; Lu, B. In situ formation of low interstitials Ti-TiC composites by gas-solid reaction. *J. Alloy. Compd.* **2018**, *769*, 37–44. [CrossRef]
300. Wei, W.-H.; Shao, Z.-N.; Shen, J.; Duan, X.-M. Microstructure and mechanical properties of in situ formed TiC-reinforced Ti–6Al–4V matrix composites. *Mater. Sci. Technol.* **2018**, *34*, 191–198. [CrossRef]
301. Sun, X.; Han, Y.; Cao, S.; Qiu, P.; Lu, W. Rapid in-situ reaction synthesis of novel TiC and carbon nanotubes reinforced titanium matrix composites. *J. Mater. Sci. Technol.* **2017**, *33*, 1165–1171. [CrossRef]
302. Zheng, Y.; Yao, X.; Su, Y.; Zhang, D. Fabrication of an in-situ Ti-2.6vol%TiC metal matrix composite by thermomechanical consolidation of a TiH2-1vol%CNTs powder blend. *Mater. Sci. Eng. A* **2016**, *667*, 300–310. [CrossRef]
303. Yang, C.; Ding, Z.; Lin, J.; Qu, S.; Li, X.; Zhang, W.; Li, Y. Serrated Flow Behavior of Titanium-Based Composites with Different In Situ TiC Contents. *Adv. Eng. Mater.* **2015**, *17*, 1383–1390. [CrossRef]
304. Zadra, M.; Girardini, L. High-performance, low-cost titanium metal matrix composites. *Mater. Sci. Eng. A* **2014**, *608*, 155–163. [CrossRef]
305. Yanbin, L.; Yong, L.; Zhongwei, Z.; Yanhui, C.; Huiping, T. Effect of addition of metal carbide on the oxidation behaviors of titanium matrix composites. *J. Alloy. Compd.* **2014**, *599*, 188–194. [CrossRef]
306. Li, S.; Sun, B.; Imai, H.; Kondoh, K. Powder metallurgy Ti–TiC metal matrix composites prepared by in situ reactive processing of Ti-VGCFs system. *Carbon* **2013**, *61*, 216–228. [CrossRef]
307. Chen, B.-Y.; Hwang, K.-S. Sintered Ti–Fe alloys with in situ synthesized TiC dispersoids. *Mater. Sci. Eng. A* **2012**, *541*, 88–97. [CrossRef]
308. Yanbin, L.; Yong, L.; Huiping, T.; Bin, W.; Bin, L. Fabrication and mechanical properties of in situ TiC/Ti metal matrix composites. *J. Alloy. Compd.* **2011**, *509*, 3592–3601. [CrossRef]
309. Bin Liu, Y.; Liu, Y.; Tang, H.P.; Wang, B.; Liu, B. Reactive sintering mechanism of Ti + Mo2C and Ti + VC powder compacts. *J. Mater. Sci.* **2011**, *46*, 902–909. [CrossRef]
310. Threrujirapapong, T.; Kondoh, K.; Imai, H.; Umeda, J.; Fugetsu, B. Mechanical Properties of a Titanium Matrix Composite Reinforced with Low Cost Carbon Black via Powder Metallurgy Processing. *Mater. Trans.* **2009**, *50*, 2757–2762. [CrossRef]
311. Kim, Y.; Kim, Y.; Ahn, J.; Chung, H. Reaction Synthesis of Ti/TiC Particulate Reinforced Composite. *Mater. Technol.* **2003**, *18*, 32–35. [CrossRef]
312. Kim, Y.-J.; Chung, H.; Kang, S.-J. In situ formation of titanium carbide in titanium powder compacts by gas–solid reaction. *Compos. Part A Appl. Sci. Manuf.* **2001**, *32*, 731–738. [CrossRef]
313. Xu, S.; Lu, T.; Qiu, J.; Fu, A.; Liu, Y. Microstructure and mechanical properties of Ti-Ta based composites enhanced by in-situ formation of TiC particles. *Mater. Charact.* **2021**, *178*, 111241. [CrossRef]

314. Myalska-Głowacka, H.; Chmiela, B.; Godzierz, M.; Sozańska, M. Residual Stress Induced by Addition of Nanosized TiC in Titanium Matrix Composite. *Materials* **2022**, *15*, 2517. [CrossRef]
315. Du, K.; Liu, Z.; Zhang, J.; Wen, L.; Xiao, Z. Microstructure and properties of high-throughput in situ network structure TiC reinforced TC4 composite materials. *Fenmo Yejin Cailiao Kexue Yu Gongcheng Mater. Sci. Eng. Powder Metall.* **2022**, *27*, 56–65. [CrossRef]
316. Lu, X.; Pan, Y.; Li, W.; Hayat, M.D.; Yang, F.; Singh, H.; Song, W.; Qu, X.; Xu, Y.; Cao, P. High-performance Ti composites reinforced with in-situ TiC derived from pyrolysis of polycarbosilane. *Mater. Sci. Eng. A* **2020**, *795*, 139924. [CrossRef]
317. Xu, X.; Liu, Y.; Tabie, V.; Cai, C.; Xiao, Y.; Zhang, X.; Li, C.; Jiang, Z.; Liu, Q.; Chen, H. High-temperature oxidation resistance of a Ti–Al–Sn–Zr titanium matrix composites reinforced with in situ TiC and Ti5Si3 fabricated by powder metallurgy. *Appl. Phys. A* **2020**, *126*, 254. [CrossRef]
318. Lu, Q.; Hao, Y.; Wang, Y.; Feng, P.; Fan, J. Microstructural evolution and high-temperature oxidation mechanisms of a Ti-Mo-Si composite. *Corros. Sci.* **2019**, *161*, 108180. [CrossRef]
319. Wang, H.; Xu, X.; Liu, Y.; Cai, C.; Sun, Z.; Han, M.; Sha, S.; Tabie, V.M. Effect of SiC Content on Hot Corrosion Resistance of TiC and Ti5Si3 Reinforced Ti-Al-Sn-Zr Titanium Matrix Composites. *J. Mater. Eng. Perform.* **2021**, *30*, 2439–2448. [CrossRef]
320. Namini, A.S.; Delbari, S.A.; Nayebi, B.; Asl, M.S.; Parvizi, S. Effect of B4C content on sintering behavior, microstructure and mechanical properties of Ti-based composites fabricated via spark plasma sintering. *Mater. Chem. Phys.* **2020**, *251*, 123087. [CrossRef]
321. Fattahi, M.; Delbari, S.A.; Namini, A.S.; Ahmadi, Z.; Azadbeh, M.; Asl, M.S. Characterization of triplet Ti–TiB–TiC composites: Comparison of in-situ formation and ex-situ addition of TiC. *Ceram. Int.* **2020**, *46*, 11726–11734. [CrossRef]
322. Balaji, V.S.; Surendarnath, S. High-Temperature Wear Behavior of Spark-Plasma-Sintered Titanium/(TiB + TiC) In Situ Composites. *Trans. Indian Inst. Met.* **2019**, *72*, 1669–1673. [CrossRef]
323. Yi, M.; Zhang, X.; Ge, C.; Liu, G.; Xu, S.; Zhong, D.; Qiao, G. Oxidation behavior of in situ synthesized (TiB + TiC)/Ti–6Al–4V composites from Ti–B4C–C and Ti–TiB2–TiC systems. *J. Mater. Res.* **2019**, *34*, 1762–1772. [CrossRef]
324. Wei, S.; Huang, L.; Li, X.; An, Q.; Geng, L. Interactive effects of cyclic oxidation and structural evolution for Ti-6Al-4V/(TiC+TiB) alloy composites at elevated temperatures. *J. Alloy. Compd.* **2018**, *752*, 164–178. [CrossRef]
325. Jia, L.; Wang, X.; Chen, B.; Imai, H.; Li, S.; Lu, Z.; Kondoh, K. Microstructural evolution and competitive reaction behavior of Ti-B4C system under solid-state sintering. *J. Alloy. Compd.* **2016**, *687*, 1004–1011. [CrossRef]
326. Li, S.; Kondoh, K.; Imai, H.; Chen, B.; Jia, L.; Umeda, J. Microstructure and mechanical properties of P/M titanium matrix composites reinforced by in-situ synthesized TiC–TiB. *Mater. Sci. Eng. A* **2015**, *628*, 75–83. [CrossRef]
327. Montealegre-Meléndez, I.; Arévalo, C.; Pérez-Soriano, E.M.; Kitzmantel, M.; Neubauer, E. Microstructural and XRD Analysis and Study of the Properties of the System Ti-TiAl-B4C Processed under Different Operational Conditions. *Metals* **2018**, *8*, 367. [CrossRef]
328. Ali, K.S.; Karunanithi, R.; Prashanth, M.; Sivasankaran, S.; Subramanian, B.; Jailani, H.S. Structure and mechanical properties of in-situ synthesized α-Ti/TiO2/TiC hybrid composites through mechanical milling and spark plasma sintering. *Ceram. Int.* **2022**, *48*, 11215–11227. [CrossRef]
329. Borkar, T.; Nag, S.; Ren, Y.; Tiley, J.; Banerjee, R. Reactive spark plasma sintering (SPS) of nitride reinforced titanium alloy composites. *J. Alloy. Compd.* **2014**, *617*, 933–945. [CrossRef]
330. Wexler, D.; Calka, A.; Mosbah, A.Y. Ti–TiN hardmetals prepared by in situ formation of TiN during reactive ball milling of Ti in ammonia. *J. Alloy. Compd.* **2000**, *309*, 201–207. [CrossRef]
331. Wexler, D.; Calka, A.; Mosbah, A.Y. Microstructure and Properties of Ti-TiN In-Situ Composites Prepared by Reactive Ball Milling of Ti in Ammonia Followed by Hot Pressing. *Mater. Sci. Forum* **2000**, *343–346*, 399–404. [CrossRef]
332. Rominiyi, A.L.; Shongwe, M.B.; Jeje, S.O.; Olubambi, P.A. Microstructure, tribological and oxidation behaviour of spark plasma sintered Ti-Ni-xTiCN composites. *J. Alloy. Compd.* **2022**, *890*, 161857. [CrossRef]
333. Sun, L.; Hui, W.; Xu, L.; Zhai, W.; Dong, H.; Wang, Y.; He, L.; Peng, J. Interface characterization and mechanical properties of Mo-added chromium carbide-nickel composite. *Ceram. Int.* **2020**, *46*, 27071–27079. [CrossRef]
334. Jõeleht, M.; Pirso, J.; Juhani, K.; Viljus, M.; Traksmaa, R. The influence of high energy milling and sintering parameters on reactive sintered (Ti, Mo)C–Ni cermets. *J. Alloy. Compd.* **2015**, *636*, 381–386. [CrossRef]
335. Jõeleht, M.; Pirso, J.; Juhani, K.; Viljus, M.; Traksmaa, R. The formation of reactive sintered (Ti, Mo)C–Ni cermet from nanocrystalline powders. *Int. J. Refract. Met. Hard Mater.* **2014**, *43*, 284–290. [CrossRef]
336. Xiong, H.; Wen, Y.; Li, Z.; Zhou, K. Dual-grained (Ti, W)C–Ni cermets by two-step carbonization: Hot isotropic press sintering of NiTiW alloys and colloidal graphite. *J. Am. Ceram. Soc.* **2019**, *102*, 4296–4305. [CrossRef]
337. Xiong, H.; Guo, Y.; Li, Z.; Zhou, K. New production of (Ti, W)C-based cermets toughened by in-situ formed WC and twinned (Ti, W)C platelets: Carbonization of the Nix(Ti0.6, W0.4)4C-type η phases. *J. Alloy. Compd.* **2018**, *731*, 253–263. [CrossRef]
338. Kwon, H.; Suh, C.; Kim, W. Preparation of a highly toughened (Ti,W)C-20Ni cermet through in situ formation of solid solution and WC whiskers. *Ceram. Int.* **2015**, *41*, 4223–4226. [CrossRef]
339. Mameri, A.; Daoud, I.; Rezzoug, A.; Azem, S.; Yamanoglu, R. Tribological properties of in situ oxide reinforced nickel matrix composites produced by pressure-assisted sintering. *Int. J. Adv. Manuf. Technol.* **2022**, *120*, 3731–3740. [CrossRef]
340. Wang, J.; Wang, W.; Jia, J. The oxidation resistance and tribological properties of Ni-based composites with in situ/ex situ Al_2O_3 and TiC ceramic phases at high temperatures. *J. Mater. Res.* **2016**, *31*, 3262–3271. [CrossRef]

341. Zhai, W.; Gao, Y.; Sun, L.; He, L.; Wang, Y. Improvement of high temperature oxidation behavior of Cr3C2-20 wt % Ni cermets by adding 1 wt.% Mo. *J. Alloy. Compd.* **2018**, *731*, 271–278. [CrossRef]
342. Zhai, W.; Gao, Y.; Sun, L.; Wang, Y.; Niwa, K.; Hasegawa, M. High pressure in-situ synthesis and physical properties of Cr_3C_2-Ni cermets. *Ceram. Int.* **2017**, *43*, 17202–17205. [CrossRef]
343. Zhai, W.Y.; Gao, Y.M.; Huang, Z.F.; He, L. Cr_3C_2–20%Ni cermets prepared by high energy milling and reactive sintering, and their mechanical properties. *Adv. Appl. Ceram.* **2016**, *115*, 327–332. [CrossRef]
344. Juhani, K.; Pirso, J.; Letunovits, S.; Viljus, M. Phase evolution, microstructure characteristics and properties of Cr_3C_2-Ni cermets prepared by reactive sintering. *Int. J. Mater. Prod. Technol.* **2011**, *40*, 75. [CrossRef]
345. Hussainova, I.; Pirso, J.; Antonov, M.; Juhani, K.; Letunovitš, S. Erosion and abrasion of chromium carbide based cermets produced by different methods. *Wear* **2007**, *263*, 905–911. [CrossRef]
346. Pirso, J.; Viljus, M.; Letunovits, S.; Juhani, K. Reactive carburizing sintering—A novel production method for high quality chromium carbide–nickel cermets. *Int. J. Refract. Met. Hard Mater.* **2006**, *24*, 263–270. [CrossRef]
347. Lei, Y.; Jiang, J.; Bi, T.; Du, J.; Pang, X. Tribological behavior of in situ fabricated graphene–nickel matrix composites. *RSC Adv.* **2018**, *8*, 22113–22121. [CrossRef]
348. Zhang, X.; Liu, Y.; Liu, X.; Zhang, J.; Chen, X.; Wu, Y.; Jing, L.; Wu, X.; Zhao, M.; Han, P. In-situ grown few-layer graphene reinforced Ni matrix composites with simultaneously enhanced strength and ductility. *Mater. Sci. Eng. A* **2021**, *828*, 142118. [CrossRef]
349. Liu, Y.; Liu, X.; Zhang, X.; Chen, X.; Zhang, J.; Jing, L.; Wu, Y.; Yu, S. Tribological properties and self-lubrication mechanism of in-situ grown graphene reinforced nickel matrix composites in ambient air. *Wear* **2022**, *496–497*, 204308. [CrossRef]
350. Zheng, X.-Q.; Liu, Y. Slurry erosion–corrosion wear behavior in SiC-containing NaOH solutions of Mo_2NiB_2 cermets prepared by reactive sintering. *Int. J. Refract. Met. Hard Mater.* **2019**, *78*, 193–200. [CrossRef]
351. Xu, X.; Zheng, Y.; Ke, Z.; Wu, H.; Yang, M.; Liang, H.; Zhao, Y. Graded Ti(C,N)-based cermets fabricated by mechanical activation and in situ carbothermal reduction: Investigation of nitrogen sintering pressure on microstructure and mechanical performance. *Ceram. Int.* **2022**, *48*, 913–919. [CrossRef]
352. Xu, X.; Zheng, Y.; Zhang, J.; Ke, Z.; Wu, H.; Yang, Z. Evolution of microstructure and interfacial characteristics of complete solid-solution Ti(C,N)-based cermets fabricated by mechanical activation and subsequent in situ carbothermal reduction. *Ceram. Int.* **2021**, *47*, 16786–16793. [CrossRef]
353. Xu, X.; Zheng, Y.; Zhang, G.; Yang, Z.; Ke, Z.; Wu, H.; Lu, X. Preparation of highly toughened Ti(C,N)-based cermets via mechanical activation and subsequent in situ carbothermal reduction. *Int. J. Refract. Met. Hard Mater.* **2020**, *92*, 105310. [CrossRef]
354. Zhang, G.; Zheng, Y.; Zhang, J.; Ke, Z.; Zhou, W.; Xiong, W. Growth of ceramic grains during liquid-phase sintering in Ti(C,N)-based cermets prepared by in situ carbothermal reduction of TiO_2. *Int. J. Refract. Met. Hard Mater.* **2019**, *85*, 105060. [CrossRef]
355. Zhang, G.; Zheng, Y.; Ke, Z.; Zhang, J.; Zhao, Y.; Lu, X. Effect of WC content on the microstructure and mechanical properties of Ti(C,N)-based cermets fabricated by in situ carbothermal reduction of TiO_2. *Mater. Sci. Eng. A* **2019**, *761*, 138024. [CrossRef]
356. Zhang, G.; Zheng, Y.; Zhou, W.; Zhao, Y.; Zhang, J.; Ke, Z.; Yu, L. Microstructure and mechanical properties of Ti(C,N)-based cermets fabricated by in situ carbothermal reduction of TiO2 and subsequent liquid phase sintering. *Ceram. Int.* **2018**, *44*, 3092–3098. [CrossRef]
357. Yi, X.; Wang, H.; Sun, K.; Shen, G.; Meng, X.; Gao, Z.; Cai, W. Tailoring martensitic transformation and mechanical properties of Ti–Ni composite reinforced by network structure of in-situ TiB and La_2O_3 phase. *Vacuum* **2021**, *184*, 109894. [CrossRef]
358. Wang, W.; Zhai, H.; Chen, L.; Huang, Z.; Bei, G.; Baumgärtner, C.; Greil, P. Preparation and mechanical properties of in situ TiCx–Ni (Si, Ti) alloy composites. *Mater. Sci. Eng. A* **2014**, *616*, 214–218. [CrossRef]
359. Zohari, S.; Sadeghian, Z.; Lotfi, B.; Broeckmann, C. Application of spark plasma sintering (SPS) for the fabrication of in situ Ni–TiC nanocomposite clad layer. *J. Alloy. Compd.* **2015**, *633*, 479–483. [CrossRef]
360. Zhao, Z.; Qi, Q.; Ma, M.; Han, R.; Shang, Q.; Yao, S. The formation mechanism of TiC/Ni composites fabricated by pressureless reactive sintering. *Int. J. Refract. Met. Hard Mater.* **2021**, *97*, 105524. [CrossRef]
361. Gao, Q.; Wang, W.; Yi, G.; Wang, B.; Feng, X.; Shi, P.; Hua, M. High temperature and room temperature tribological behaviors of in-situ carbides reinforced Ni-based composites by reactive sintering Ni and Ti2AlC precursor. *Wear* **2022**, *488–489*, 204165. [CrossRef]
362. Zhao, Z.; Yu, X.; Wang, C.; Yao, S.; Qi, Q.; Wang, L. Oxidation mechanism of in-situ TiC/Ni composites at 1073 K. *Corros. Sci.* **2022**, *194*, 109958. [CrossRef]
363. Ding, L.; Xiang, D.; Pan, Y.; Zhang, T.; Wu, Z. In situ synthesis of TiC cermet by spark plasma reaction sintering. *J. Alloy. Compd.* **2016**, *661*, 136–140. [CrossRef]
364. Wang, W.; Zhai, H.; Chen, L.; Huang, Z.; Bei, G.; Greil, P. Preparation and mechanical properties of TiC x–$(NiCu)_3Al$–$CuNi_2$ Ti–Ni hybrid composites by reactive pressureless sintering pre-alloyed Cu/Ti_3AlC_2 and Ni as precursor. *Mater. Sci. Eng. A* **2016**, *670*, 351–356. [CrossRef]
365. Patil, A.; Walunj, G.; Torgerson, T.B.; Koricherla, M.V.; Khan, M.U.F.; Scharf, T.W.; Gupta, R.; Borkar, T. Tribological Behavior of In Situ Processed Ni-Ti-C Nanocomposites. *Tribol. Trans.* **2021**, *64*, 53–64. [CrossRef]
366. Hu, W.; Huang, Z.; Yu, Q.; Wang, Y.; Jiao, Y.; Zhou, Y.; Zhai, H. Investigation on High Temperature Mechanical Behaviors of TiC-γ' Reinforced Ni Composite. *Met. Mater. Int.* **2021**, *27*, 3003–3012. [CrossRef]

367. Hu, W.; Huang, Z.; Cai, L.; Lei, C.; Zhai, H.; Hao, S.; Yu, W.; Zhou, Y. Preparation and mechanical properties of TiCx-Ni3(Al,Ti)/Ni composites synthesized from Ni alloy and Ti$_3$AlC$_2$ powders. *Mater. Sci. Eng. A* **2017**, *697*, 48–54. [CrossRef]
368. Hu, W.; Huang, Z.; Cai, L.; Lei, C.; Zhai, H.; Wo, S.; Li, X. In-situ TiC and γ'-Ni3(Al,Ti) triggered microstructural modification and strengthening of Ni matrix composite by reactive hot-press sintering pure Ni and Ti$_2$AlC precursor. *J. Alloy. Compd.* **2018**, *747*, 1043–1052. [CrossRef]
369. Chiker, N.; Benamor, A.; Haddad, A.; Hadji, Y.; Hakem, M.; Badji, R.; Labaiz, M.; Azzaz, M.; Hadji, M. Pressureless sintering and tribological properties of in-situ TiC-Ni3(Al,Ti)/Ni(Al,Ti) composites. *Int. J. Refract. Met. Hard Mater.* **2021**, *98*, 105559. [CrossRef]
370. Chang, F.; Qiu, F.; Li, C.; Wang, Y.; Jiang, Q. Effects of Cr and Mo elements on the microstructures and compressive properties of the in situ (TiCxNy–TiB2)/Ni cermets. *Prog. Nat. Sci.* **2019**, *29*, 20–27. [CrossRef]
371. Rominiyi, A.L.; Shongwe, M.B.; Tshabalala, L.C.; Ogunmuyiwa, E.N.; Jeje, S.O.; Babalola, B.J.; Olubambi, P.A. Spark plasma sintering of Ti–Ni–TiCN composites: Microstructural characterization, densification and mechanical properties. *J. Alloy. Compd.* **2020**, *848*, 156559. [CrossRef]
372. Chen, Y.-C.; Fan, F.-Y.; Tsai, M.-H.; Wu, C.-H.; Chen, S.-T.; Ou, S.-F. Microstructure and mechanical properties of Ti nitride/Ni metal-based composites fabricated by reactive sintering. *Ceram. Int.* **2019**, *45*, 10834–10839. [CrossRef]
373. Genç, A.; Ayas, E.; Öveçoğlu, M.L.; Turan, S. Fabrication of in situ Ni(W)–WC nano composites via mechanical alloying and spark plasma sintering. *J. Alloy. Compd.* **2012**, *542*, 97–104. [CrossRef]
374. Azem, S.; Grosbras, M.; Yefsah, S. Effect of carbon content on the reactive sintering of mixed W-Co-C powders. *Rev. Métallurgie* **2004**, *101*, 419–425. [CrossRef]
375. Zhang, X.-H.; Lin, C.-G.; Cui, S.; Li, Z.-D. Microstructure and properties of Al$_2$O$_3$ dispersion-strengthened copper fabricated by reactive synthesis process. *Rare Met.* **2014**, *33*, 191–195. [CrossRef]
376. Yan, P.; Lin, C.; Cui, S.; Lu, Y.; Zhou, Z.; Li, Z. Microstructural features and properties of high-hardness and heat-resistant dispersion strengthened copper by reaction milling. *J. Wuhan Univ. Technol. Sci. Ed.* **2011**, *26*, 902–907. [CrossRef]
377. Fallah, M.K.; Tabrizi, S.G.; Seyedi, S. Investigation of in-situ synthesis of alumina reinforcement and comparative flexural behavior with respect to ex-situ Al$_2$O$_3$ reinforced copper composite. *J. Ultrafine Grained Nanostruct. Mater.* **2021**, *54*, 101–111. [CrossRef]
378. Fu, Y.; Pan, Q.; Cao, Z.; Li, S.; Huo, Y. Strength and electrical conductivity behavior of nanoparticles reaction on new alumina dispersion-strengthened copper alloy. *J. Alloy. Compd.* **2019**, *798*, 616–621. [CrossRef]
379. Yan, Y.; Zou, J.; Zhang, X.; Xiao, Q.; Chen, B.; Huang, F.; Li, X.; Yang, B.; Liang, T. Investigation on microstructure and properties of TiC0.5-Al$_2$O$_3$/Cu composites fabricated by a novel in-situ reactive synthesis. *Ceram. Int.* **2021**, *47*, 18858–18865. [CrossRef]
380. Shojaeepour, F.; Abachi, P.; Purazrang, K.; Moghanian, A.H. Production and properties of Cu/Cr$_2$O$_3$ nano-composites. *Powder Technol.* **2012**, *222*, 80–84. [CrossRef]
381. Liu, S.; Li, L.; Zhou, M.; Liang, S.; Zhang, Y.; Huang, J.; Tian, B.; Geng, Y.; Liu, Y.; Jia, Y.; et al. Preparation and properties of graphene reinforced Cu/$_{0.5}$CeO$_{230}$Cr electrical contact materials. *Vacuum* **2022**, *195*, 110687. [CrossRef]
382. Gao, Z.; Zuo, T.; Wang, M.; Zhang, L.; Da, B.; Ru, Y.; Xue, J.; Wu, Y.; Han, L.; Xiao, L. In-situ graphene enhanced copper wire: A novel electrical material with simultaneously high electrical conductivity and high strength. *Carbon* **2022**, *186*, 303–312. [CrossRef]
383. Yang, T.; Chen, W.; Zhang, H.; Ma, L.; Fu, Y.-Q. In-situ generated graphene from wheat flour for enhancing mechanical and electrical properties of copper matrix composites. *Mater. Sci. Eng. A* **2022**, *835*, 142662. [CrossRef]
384. Wang, M.; Zuo, T.; Xue, J.; Ru, Y.; Wu, Y.; Xu, Z.; Gao, Z.; Han, L.; Xiao, L. A novel approach for in-situ preparation of copper/graphene composite with high hardness and high electrical conductivity. *Mater. Lett.* **2022**, *319*, 132219. [CrossRef]
385. Akbarpour, M.; Sadeghi, N.; Aghajani, H. Nano TiC-Graphene-Cu composites fabrication by a modified ball-milling method followed by reactive sintering: Effects of reinforcements content on microstructure, consolidation, and mechanical properties. *Ceram. Int.* **2022**, *48*, 130–136. [CrossRef]
386. Bian, Y.; Ni, J. Microstructure Evolution and Properties of In Situ Micro/Nanoscale Mo2C Reinforced Copper Composite Synthesized by Hot-Pressing Consolidation of Mechanical Alloying Powders. *J. Mater. Eng. Perform.* **2022**, *31*, 4604–4610. [CrossRef]
387. Ke-Sheng, Z.; Sheng-Qi, X.; Jing-En, Z. Effect of sintering methods on properties of Cu-Based composite reinforced by mechanically alloyed Cu–Mo–C powder. *Results Mater.* **2021**, *9*, 100153. [CrossRef]
388. Zeng, W.; Xie, J.; Zhou, D.; Fu, Z.; Zhang, D.; Lavernia, E.J. Bulk Cu-NbC nanocomposites with high strength and high electrical conductivity. *J. Alloy. Compd.* **2018**, *745*, 55–62. [CrossRef]
389. Shiri, S.G.; Abachi, P.; Pourazarang, K.; Rahvard, M.M. Preparation of in-situ Cu/NbC nanocomposite and its functionally graded behavior for electrical contact applications. *Trans. Nonferrous Met. Soc. China* **2015**, *25*, 863–872. [CrossRef]
390. Long, B.; Umemoto, M.; Todaka, Y.; Othman, R.; Zuhailawati, H. Fabrication of high strength Cu–NbC composite conductor by high pressure torsion. *Mater. Sci. Eng. A* **2011**, *528*, 1750–1756. [CrossRef]
391. Zuhailawati, H.; Salihin, H.M.; Mahani, Y. Microstructure and properties of copper composite containing in situ NbC reinforcement: Effects of milling speed. *J. Alloy. Compd.* **2010**, *489*, 369–374. [CrossRef]
392. Long, B.; Zuhailawati, H.; Umemoto, M.; Todaka, Y.; Othman, R. Effect of ethanol on the formation and properties of a Cu–NbC composite. *J. Alloy. Compd.* **2010**, *503*, 228–232. [CrossRef]
393. Zuhailawati, H.; Mahani, Y. Effects of milling time on hardness and electrical conductivity of in situ Cu–NbC composite produced by mechanical alloying. *J. Alloy. Compd.* **2009**, *476*, 142–146. [CrossRef]

394. Zuhailawati, H.; Yong, T. Consolidation of dispersion strengthened copper–niobium carbide composite prepared by in situ and ex situ methods. *Mater. Sci. Eng. A* **2009**, *505*, 27–30. [CrossRef]
395. Bian, Y.; Ni, J.; Wang, C.; Zhen, J.; Hao, H.; Kong, X.; Chen, H.; Li, J.; Li, X.; Jia, Z.; et al. Microstructure and wear characteristics of in-situ micro/nanoscale niobium carbide reinforced copper composites fabricated through powder metallurgy. *Mater. Charact.* **2021**, *172*, 110847. [CrossRef]
396. Dong, S.J.; Zhou, Y.; Chang, B.H.; Shi, Y.W. Formation of a TiB2-reinforced copper-based composite by mechanical alloying and hot pressing. *Met. Mater. Trans. A* **2002**, *33*, 1275–1280. [CrossRef]
397. Ma, Z.; Tjong, S. High temperature creep behavior of in-situ TiB2 particulate reinforced copper-based composite. *Mater. Sci. Eng. A* **2000**, *284*, 70–76. [CrossRef]
398. Jiang, Y.; Wang, C.; Liang, S.; Ren, J.; Du, X.; Liu, F. TiB2(-TiB)/Cu in-situ composites prepared by hot-press with the sintering temperature just beneath the melting point of copper. *Mater. Charact.* **2016**, *121*, 76–81. [CrossRef]
399. Lan, T.; Jiang, Y.-H.; Zhang, X.-J.; Cao, F.; Liang, S.-H. Competitive precipitation behavior of hybrid reinforcements in copper matrix composites fabricated by powder metallurgy. *Int. J. Miner. Met. Mater.* **2021**, *28*, 1090–1096. [CrossRef]
400. Leong, C.; Lu, L.; Fuh, J.; Wong, Y. In-situ formation of copper matrix composites by laser sintering. *Mater. Sci. Eng. A* **2002**, *338*, 81–88. [CrossRef]
401. Dudina, D.V.; Korchagin, M.A.; Gavrilov, A.I.; Bulina, N.V.; Batraev, I.; Esikov, M.A.; Georgarakis, K.; Kato, H. Formation of TiC-Cu nanocomposites by a reaction between Ti25Cu75 melt-spun alloy and carbon. *Mater. Lett.* **2019**, *235*, 104–106. [CrossRef]
402. Dudina, D.V.; Vidyuk, T.M.; Korchagin, M.A.; Gavrilov, A.I.; Bulina, N.V.; Esikov, M.A.; Datekyu, M.; Kato, H. Interaction of a Ti–Cu Alloy with Carbon: Synthesis of Composites and Model Experiments. *Materials* **2019**, *12*, 1482. [CrossRef]
403. Ni, J.; Li, J.; Luo, W.; Han, Q.; Yin, Y.; Jia, Z.; Huang, B.; Hu, C.; Xu, Z. Microstructure and properties of in-situ TiC reinforced copper nanocomposites fabricated via long-term ball milling and hot pressing. *J. Alloy. Compd.* **2018**, *755*, 24–28. [CrossRef]
404. Wang, F.; Li, Y.; Chiba, A. Effects of carbon content and size on Ti-C reaction behavior and resultant properties of Cu-Ti-C alloy system. *Mater. Charact.* **2018**, *141*, 186–192. [CrossRef]
405. Oanh, N.T.H.; Viet, N.H.; Kim, J.-S.; Junior, A.M.J. Characterization of In-Situ Cu–TiH2–C and Cu–Ti–C Nanocomposites Produced by Mechanical Milling and Spark Plasma Sintering. *Metals* **2017**, *7*, 117. [CrossRef]
406. Bagheri, G. The effect of reinforcement percentages on properties of copper matrix composites reinforced with TiC particles. *J. Alloy. Compd.* **2016**, *676*, 120–126. [CrossRef]
407. Wang, F.; Li, Y.; Wang, X.; Koizumi, Y.; Kenta, Y.; Chiba, A. In-situ fabrication and characterization of ultrafine structured Cu–TiC composites with high strength and high conductivity by mechanical milling. *J. Alloy. Compd.* **2016**, *657*, 122–132. [CrossRef]
408. Dudina, D.V.; Vidyuk, T.M.; Gavrilov, A.I.; Ukhina, A.V.; Bokhonov, B.B.; Legan, M.A.; Matvienko, A.A.; Korchagin, M.A. Separating the reaction and spark plasma sintering effects during the formation of TiC–Cu composites from mechanically milled Ti–C–3Cu mixtures. *Ceram. Int.* **2021**, *47*, 12494–12504. [CrossRef]
409. Viet, N.H.; Oanh, N.T.H. Microstructure and Electrical Property of Ex-Situ and In-Situ Copper Titanium Carbide Nanocomposites. *Metals* **2020**, *10*, 735. [CrossRef]
410. Vidyuk, T.M.; Dudina, D.V.; Korchagin, M.A.; Gavrilov, A.I.; Ukhina, A.V.; Bulanova, U.E.; Legan, M.A.; Novoselov, A.N.; Esikov, M.A.; Anisimov, A.G. Manufacturing of TiC-Cu composites by mechanical milling and spark plasma sintering using different carbon sources. *Surf. Interfaces* **2021**, *27*, 101445. [CrossRef]
411. Sadeghi, N.; Aghajani, H.; Akbarpour, M. Microstructure and tribological properties of in-situ TiC-C/Cu nanocomposites synthesized using different carbon sources (graphite, carbon nanotube and graphene) in the Cu-Ti-C system. *Ceram. Int.* **2018**, *44*, 22059–22067. [CrossRef]
412. Sauer, C.; Weissgaerber, T.; Puesche, W.; Dehm, G.; Mayer, J.; Kieback, B. High temperature creep of micro-crystalline dispersion strengthened copper alloys. *Int. J. Powder Metall.* **1997**, *33*, 45–53. [CrossRef]
413. Sadeghi, N.; Akbarpour, M.; Aghajani, H. A novel two-step mechanical milling approach and in-situ reactive synthesis to fabricate TiC/Graphene layer/Cu nanocomposites and investigation of their mechanical properties. *Mater. Sci. Eng. A* **2018**, *734*, 164–170. [CrossRef]
414. Quan, Y.; Hu, B.; Fu, S.; Wan, D.; Bao, Y.; Feng, Q.; Grasso, S.; Hu, C. Fabrication, Microstructure, and Properties of In Situ V_2C-Reinforced Copper Composites. *Metals* **2021**, *11*, 1829. [CrossRef]
415. Zhang, Q.; Chen, B.; Chen, Z.; Zhu, Z.; Hu, X.; Ding, Y.; Liang, S. Microstructure and properties of W Cu composites reinforced by in-situ generated WC. *Int. J. Refract. Met. Hard Mater.* **2021**, *99*, 105585. [CrossRef]
416. Zhao, M.; Xu, B.; Zhang, P.; Xu, J.; Jiang, Y.; Liu, F.; Yan, Y. Microstructure development of Y–Ti–O dispersion strengthened Cu alloys fabricated by mechanical alloying. *Mater. Charact.* **2022**, *186*, 111808. [CrossRef]
417. Fu, S.; Xu, H. Microstructure and Wear Behavior of (Ti,V)C Reinforced Ferrous Composite. *J. Mater. Eng. Perform.* **2010**, *19*, 825–828. [CrossRef]
418. Jing, W.; Yisan, W.; Yichao, D. Reaction synthesis of Fe–(Ti,V)C composites. *J. Mater. Process. Technol.* **2008**, *197*, 54–58. [CrossRef]
419. Wang, J.; Wang, Y.; Ding, Y.; Gong, W. Microstructure and wear-resistance of Fe–(Ti,V)C composite. *Mater. Des.* **2007**, *28*, 2207–2209. [CrossRef]
420. Jing, W.; Yisan, W.; Yichao, D. Production of (Ti,V)C reinforced Fe matrix composites. *Mater. Sci. Eng. A* **2007**, *454–455*, 75–79. [CrossRef]

421. Chen, X.; Zhai, H.; Wang, W.; Huang, Z. Fabrication of Cr_2AlC-Fe based composites by in-situ reaction technique. *Kuei Suan Jen Hsueh Pao J. Chin. Ceram. Soc.* **2013**, *41*, 309–313. [CrossRef]
422. Gupta, P.; Kumar, D.; Quraishi, M.A.; Parkash, O. Effect of sintering parameters on the corrosion characteristics of Iron-Alumina metal matrix nanocomposites. *J. Mater. Environ. Sci.* **2015**, *6*, 155–167.
423. Guan, D.; He, X.; Zhang, R.; Qu, X. Microstructure and tensile properties of in situ polymer-derived particles reinforced steel matrix composites produced by powder metallurgy method. *Mater. Sci. Eng. A* **2017**, *705*, 231–238. [CrossRef]
424. Jiang, J.; Li, S.; Hu, S.; Zhang, J.; Yu, W.; Zhou, Y. Comparison of high Cr white iron composites reinforced with directly added TiC and in situ formed TiCx. *J. Mater. Res. Technol.* **2020**, *9*, 3140–3148. [CrossRef]
425. Zhang, Q.; Li, S.; Zhang, W.; Peng, K. Influence of processed parameters on the magnetic properties of Fe/Fe3O4 composite cores. *J. Mater. Sci. Mater. Electron.* **2021**, *32*, 1233–1241. [CrossRef]
426. Li, J.; Yu, J.; Li, W.; Che, S.; Zheng, J.; Qiao, L.; Ying, Y. The preparation and magnetic performance of the iron-based soft magnetic composites with the Fe@Fe_3O_4 powder of in situ surface oxidation. *J. Magn. Magn. Mater.* **2018**, *454*, 103–109. [CrossRef]
427. Marinca, T.F.; Neamţu, B.V.; Chicinaş, I.; Isnard, O. Structural and Magnetic Characteristics of Composite Compacts of Fe/Fe3O4 Type Obtained by Sintering. *IEEE Trans. Magn.* **2014**, *50*, 2800604. [CrossRef]
428. Zhang, K.; Li, Y.; Yan, H.; Wang, C.; Li, H.; Liang, J.; Dang, J. Effect of Sintering Temperature on Microstructure and Mechanical Properties of Hot-Pressed Fe/$FeAl_2O_4$ Composite. *Crystals* **2021**, *11*, 422. [CrossRef]
429. Gupta, P.; Kumar, D.; Jha, A.K.; Parkash, O. Effect of height to diameter (h/d) ratio on the deformation behaviour of Fe–Al2O3 metal matrix nanocomposites. *Bull. Mater. Sci.* **2016**, *39*, 1245–1258. [CrossRef]
430. Gupta, P.; Kumar, D.; Parkash, O.; Jha, A.K. Structural and mechanical behaviour of 5% Al2O3-reinforced Fe metal matrix composites (MMCs) produced by powder metallurgy (P/M) route. *Bull. Mater. Sci.* **2013**, *36*, 859–868. [CrossRef]
431. Zhang, Y.; Feng, K.; Shui, Y. Effect of MoS2 on Iron-Based Friction Material Prepared Directly from Vanadium-Bearing Titanomagnetite Concentrates. *Met. Mater. Int.* **2020**, *26*, 1070–1078. [CrossRef]
432. Jiang, J.; Li, S.; Hu, S.; Zhou, Y. Effects of in situ formed TiCx on the microstructure, mechanical properties and abrasive wear behavior of a high chromium white iron. *Mater. Chem. Phys.* **2018**, *214*, 80–88. [CrossRef]
433. Luo, Z.; Fan, X.; Zhang, Y.; Yang, Z.; Wang, J.; Wu, Z.; Liu, X.; Li, G.; Li, Y. Formation mechanism and magnetic performance of Fe-Si soft magnetic composites coated with MnO-SiO_2 composite coatings. *Adv. Powder Technol.* **2021**, *32*, 3364–3371. [CrossRef]
434. Shen, Y.; Huang, Z.; Zhang, L.; Li, K.; Cao, Z.; Xiao, P.; Jian, Y. Sintering Mechanism, Microstructure Evolution, and Mechanical Properties of Ti-Added Mo2FeB2-Based Cermets. *Materials* **2020**, *13*, 1889. [CrossRef]
435. Zhang, F.; Zhao, P.; Liu, T.; Liu, S.; Zhang, P.; Yu, J.; Sun, J. In-situ synthesis of nanodiamonds reinforced iron-nickel matrix nanocomposites and their properties. *Diam. Relat. Mater.* **2018**, *83*, 60–66. [CrossRef]
436. Rasib SZ, M.; Zuhailawati, H. Fabrication of in situ Fe-NbC composite by mechanical alloying. *Sains Malays.* **2013**, *42*, 1751–1754.
437. Li, B.; Liu, Y.; Cao, H.; He, L.; Li, J. Rapid synthesis of TiB2/Fe composite in situ by spark plasma sintering. *J. Mater. Sci.* **2009**, *44*, 3909–3912. [CrossRef]
438. Liu, J.; Wu, M.; Chen, J.; Ye, Z.; Lin, C.; Chen, W.; Du, C. In-Situ Synthesis, Microstructure, and Mechanical Properties of TiB_2-Reinforced Fe-Cr-Mn-Al Steel Matrix Composites Prepared by Spark Plasma Sintering. *Materials* **2021**, *14*, 2346. [CrossRef]
439. Akhtar, F. Processing, microstructure, properties and wear behavior of in situ synthesized TiB2 and TiC thick films on steel substrates. *Surf. Coat. Technol.* **2007**, *201*, 9603–9609. [CrossRef]
440. Akhtar, F.; Hasan, F. Reactive sintering and properties of TiB2 and TiC porous cermets. *Mater. Lett.* **2008**, *62*, 1242–1245. [CrossRef]
441. Jing, W.; Yisan, W. In-situ production of Fe–TiC composite. *Mater. Lett.* **2007**, *61*, 4393–4395. [CrossRef]
442. Zhai, D.; Shui, Y.; Feng, K.; Zhang, Y. Effects of rare-earth oxides on the microstructure and properties of Fe-based friction materials synthesized by in situ carbothermic reaction from vanadium-bearing titanomagnetite concentrates. *RSC Adv.* **2019**, *9*, 20687–20697. [CrossRef]
443. Liu, Z.; Zhang, H.; Liu, X.; Zheng, Y.; Huang, X.; Zou, D. Effects of diffusion alloying on the microstructure and properties of TiC-reinforced Fe-based PM materials. *Int. J. Mater. Res.* **2016**, *107*, 1082–1090. [CrossRef]
444. Berns, H.; Wewers, B. Development of an abrasion resistant steel composite with in situ TiC particles. *Wear* **2001**, *251*, 1386–1395. [CrossRef]
445. Mojisola, T.; Ramakokovhu, M.M.; Raethel, J.; Olubambi, P.; Matizamhuka, W. In-situ synthesis and characterization of Fe–TiC based cermet produced from enhanced carbothermally reduced ilmenite. *Int. J. Refract. Met. Hard Mater.* **2019**, *78*, 92–99. [CrossRef]
446. Farid, A.; Guo, S.; Cui, F.-E.; Feng, P.; Lin, T. TiB2 and TiC stainless steel matrix composites. *Mater. Lett.* **2007**, *61*, 189–191. [CrossRef]
447. Tang, C.F.; Pan, F.; Qu, X.H.; Duan, B.H.; He, X.B.; Wang, T.J. Production of iron matrix composite reinforced by TiN particulate through nitriding by powder metallurgy. *Powder Met.* **2009**, *52*, 24–27. [CrossRef]
448. Zeng, X.G. Reaction synthesis of ultrafine titanium diborides and nitrides reinforced steel matrix composites *in situ* by spark plasma sintering. *Powder Met.* **2015**, *58*, 193–196. [CrossRef]
449. Weber, S.; Berns, H. Development of Wear and Corrosion Resistant Metal Matrix Composites with hard Particles formed in Situ. *Mater. Werkst.* **2007**, *38*, 205–211. [CrossRef]
450. Qin, Y.; Wang, Y.; Wu, S.; Fan, L.; Miao, W.; Chen, H. Formation mechanism of in-situ V8C7 and V3B4 particles in iron matrix composites by vacuum sintering. *Mater. Werkst.* **2021**, *52*, 529–539. [CrossRef]

451. Zhang, Z.; Chen, Y.; Zuo, L.; Zhang, Y.; Qi, Y.; Gao, K. The effect of volume fraction of WC particles on wear behavior of in-situ WC/Fe composites by spark plasma sintering. *Int. J. Refract. Met. Hard Mater.* **2017**, *69*, 196–208. [CrossRef]
452. Zhang, Z.; Chen, Y.; Zhang, Y.; Gao, K.; Zuo, L.; Qi, Y.; Wei, Y. Tribology characteristics of ex-situ and in-situ tungsten carbide particles reinforced iron matrix composites produced by spark plasma sintering. *J. Alloy. Compd.* **2017**, *704*, 260–268. [CrossRef]
453. Jha, P.; Gupta, P.; Kumar, D.; Parkash, O. Synthesis and characterization of Fe–ZrO_2 metal matrix composites. *J. Compos. Mater.* **2014**, *48*, 2107–2115. [CrossRef]